Delft University of Technology

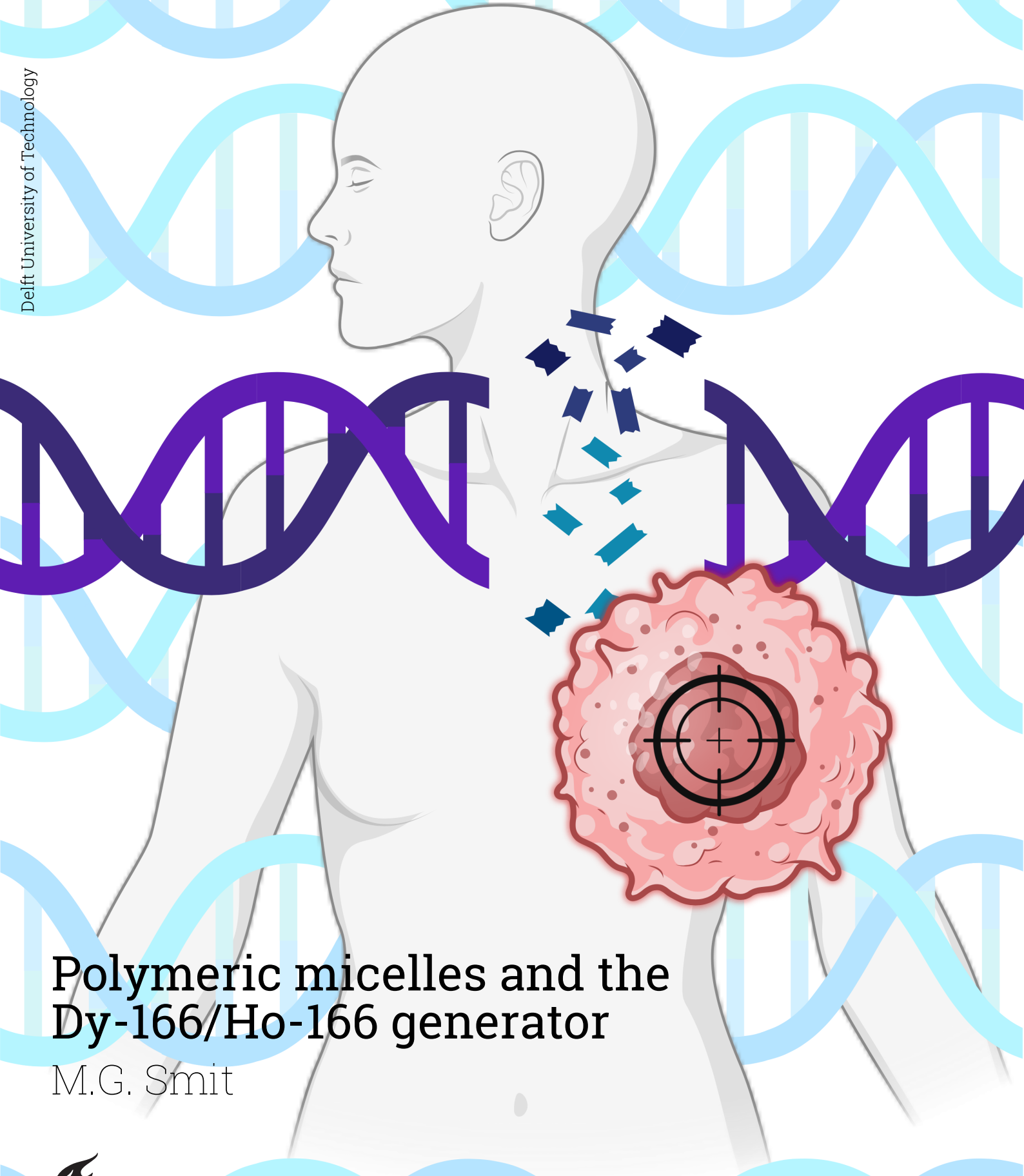

Polymeric micelles and the Dy-166/Ho-166 generator

M.G. Smit

TU Delft

Polymeric micelles and the Dy-166/Ho-166 generator

A study of the loading mechanism of Dy/Dy-166 and Ho-166 into PCL-b-PEO polymeric micelles for imaging and cancer treatment

by

M.G. Smit

to obtain the degree of **Master of Science** in
Applied Physics
at the Delft University of Technology,
to be defended publicly on November 3, 2023 at 10:00.

Project Duration:	January, 2023 - November, 2023	
Faculty:	Delft University of Technology	
	Applied Sciences	
	TU Delft Reactor Institute	
Group:	Applied Radiation & Isotopes	
Thesis committee:	Dr.ir. A.G. Denkova	TU Delft, Supervisor
	Dr.ir. R.M. de Kruijff	TU Delft
	Dr. R. Eelkema	TU Delft
	R. Wang, PhD	TU Delft, Daily Supervisor
Cover:	Created with BioRender.com	
Report style:	TU Delft Report Style	

TU Delft

Acknowledgements

My period at the Applied Radiation & Isotopes (ARI) Group at the TU Delft is one I will look back upon with gratitude. I received a warm welcome into this group of patient and kind people. The project and flexibility I was given have allowed me to get back on track after a tough time last year. For that, I am immensely thankful.

Dr. Antonia Denkova and Runze Wang have been wonderful supervisors. I wish to thank them both for the brainstorming sessions, their valuable input and most importantly, their time. I have admired your willingness to explain difficult topics and be open to new ideas. Thank you to Baukje and Astrid for familiarizing me with working in the lab and for listening to my input. To Folkert, thank you for your friendliness, discussions about chess and teaching me how to use the radiation detection machinery. Thank you Eline for your patience while I figured out how to run experiments with radiation under your watchful eye. Also thank you for the enthusiasm and for the conversations we have had. It was great to have a chat in the lab while we were both collecting hundreds of droplets. If only we could roll a die to make the droplets fall faster. Thank you to the others at the ARI group for the talks, coffees and laughs. It has been great to get to know all of you.

A special thanks to Dosti Dihalu, whom I shared numerous conversations and memories with. It was incredibly special for me to get to meet you here.

To my loving friends and family, thank you for the unconditional support. I am proud to be amongst you.

”Cogito, ergo sum.”
I think, therefore I am.
- R. Decartes

Abstract

Radionuclide therapy is a therapy that uses ionizing radiation to kill cancer cells and destroy or diminish tumours with target-specific radiopharmaceuticals. A radioisotope used in radionuclide therapy is Holmium-166 (Ho-166). Although applied in the clinic for treatment of liver tumours and bone marrow transplantation, the treatment effectiveness of Ho-166 could be improved by the use of a so called *in vivo* Dysprosium-166(Dy-166)/Ho-166 generator. This allows an increase in radiation dose given to the disease tissue when the Dy-166/Ho-166 generator is used instead of solely Ho-166. The application of this generator is hindered by an effect called internal conversion (IC). This affect can arise after the decay of Dy-166 to Ho-166, which can cause separation of Ho-166 from its carrier. Once separated, Ho-166 would be able to move freely through the body, which is highly undesired for radionuclide therapy.
Polymeric micelles are nanocarriers that might form a solution in the application of the Dy-166/Ho-166 generator in radionuclide therapy. A novel method was proposed to effectively load metallic species into polymeric micelles with high loading stability. It was proposed that the loading of metallic species as aqueous hydroxides would result in a high radiolabelling efficiency and high stability. The main goal of this thesis was to investigate and understand the loading mechanism of metallic species and polymeric micelles with a focus on the loading of Dy/Dy-166 and Ho-166.

The studied micelles were based on the amphiphilic block copolmyer poly(ϵ-caprolactone-b-ethylene oxide) (PCL-b-PEO) with molecular weight [2800-2000]. Chemical speciation analysis was done to predict in which form Dy/Dy-166 could be introduced to the micelles. After loading, size exclusion chromatography (SEC) and gamma measurements were done to determine the radiolabelling efficiency. Stability studies were performed by challenging the labelled micelles with diethylenetriaminepentaacetic acid (DTPA). The experiments with Dy/Dy-166 and supporting experiments with Gallium(Ga)/Ga-68 have shown that it was not effective to load metallic species as free ions or as solid precipitates. It was found that aqueous hydroxides play an important role in achieving good loading and high stability, thereby confirming the proposed loading mechanism.

The second goal was to study if polymeric micelles were able to retain Ho-166 inside their core under the effects of internal conversion. No additional losses of Ho-166 were found when Dy/Dy-166 and Ho-166 were loaded into the micelles. It was concluded that the PCL-PEO micelles prevented the loss of Ho-166 under internal conversion effects.

With the low radiolabelling efficiency and poor stability, it was further concluded that the Dy-166/Ho-166 generator in the current form is not a suitable candidate for the micelle application in radionuclide therapy.

This study has helped in getting a better understanding of the loading mechanism of metallic species into polymeric micelles. More characterisation studies can be performed to gain further knowledge of the loading mechanism. Once this mechanism is fully understood, predictions can be made for the effetive radiolabelling of micelles with other metallic species.

Contents

Nomenclature

Below, the acronyms and symbols for chemical species and other quantities and units used in this report can be found.

Acronyms

Acronym	Definition
CHEAQS Next	CHemical Equilibria in AQuatic Systems Next
CMC	Critical Micelle Concentration
CPM	Counts Per Minute
CT	Computed Tomography
DLS	Dynamic Light Scattering
DNA	Deoxyribonucleic acid
DPM	Disintegrations Per Minute
EPR	Enhanced Permeability and Retention
HCC	Hepotocellular carcinoma
IC	Internal Conversion
LEGe	Low-Energy Germanium
LET	Linear Energy Transfer
MRI	Magnetic Resonance Imaging
MW	Molecular Weight
NET	Neuroendocrine Tumours
PET	Positron Emission Tomography
PMT	Photomultiplier Tube
RE	Radiolabelling Efficiency
RNT	Raionuclide Therapy
SD	Standard Deviation
SEC	Size Exclusion Tomography
SLS	Static Light Scattering
SSTR	Somatostatin Receptors

Chemical species and symbols

Chemical formula/Symbol	Name
γ	gamma particle
μm	micrometer
(aq)	aqueous form
(s)	solid form
A	activity in Bq
α	alpha particle
Be	Beryllium
β	beta particle
Bq	Becquerel
DOTA	dodecane tetraacetic acid, $CH_2CH_2NCH_2CO_2H)_4$
DTPA	diethylenetriaminepentaacetic acid
Dy	dysprosium

Chemical formula/Symbol	Name
Dy2O3	dysprosiumoxide
Dy3+	dysprosium
$Dy(NO_3)_3{\cdot}5H_2O$	dysprosium(III)nitrate pentahydride
Dy(OH)3	dysprosium(III)hydroxide
EDTMP	Dimethylthiophosphate
Er	erbium
eV	electronvolt
g/L	gram/liter
g/mol	gram/mol
Ga	gallium
Ga(NO3)3	gallium nitrate
Ga(OH)3	gallium hydroxide
Ga(OH)4-	gallium hydroxide
Ge	germanium
gr	gram
h	hour
H2O	water
HCl	hydrochlorix acid
HEPES	4-(2-hydroxyethyl)-1-piperazineethanesulfonic acid
Ho	holmium
Ho3+	holmium
Ho(OH)2+	holmium hydroxide
Ho(OH)2 +	holmium hydroxide
Ho(OH)3	holmium hydroxide
Ho(OH)4	holmium hydroxide
hr	hour
kBq	kilo Becquerel
keV	kilo electronvolt
Kr	krypton
L	liter
λ	decay constant in s^{-1}
M	mol/liter
m	meter
MBQ	Mega Becquerel
MES	2-(N-morpholino)ethanesulfonic acid
MeV	Mega electronvolt
mg	milligram
μL	micro liter
μs	micro second
mL	milliliter
mM	milli molar
mm	millimiter
Mo	molybdenum
MQ	MilliQ
N	amount of atoms
n	amount of moles
N_A	Avogadro's number
N_{agg}	aggregation number
NaI	sodium iodide
NaOH	sodium hydroxide
nm	nanometer
PCL-PEO	poly-ϵ-caprolactone-poly(ethylene oxide)
Rb	rubidium

Chemical formula/Symbol	Name
s	second
Si	silicon
t	time
T	half-life time
$t_{1/2}$	half-life time
Tc	technetium
Tl	thallium
t_{max}	time of maximum daughter activity
X(OH)3	chemical species X hydroxide
Y	yttrium
Z	atomic number
Zn	zinc

1

Introduction

Radiation therapy uses ionizing radiation to kill cancer cells and destroy or diminish tumours by damaging the cells' DNA. Frequently, external radiation is used to treat a patient. Another available treatment option is targeted radionuclide therapy (RNT), which is a treatment that uses a molecule or other carrier labeled with a radionuclide to deliver a lethal level of radiation to disease sites in the body. The combination of a carrier and a radionuclide forms a so-called radiopharmaceutical. [1] Although encouraging, RNT seldom leads to cure, often due to the survival of cancer cells after treatment. [2, 3, 4] If the treatment effectiveness could be increased, the quality of life of the patient could be improved and perhaps extended.

A radioisotope currently used in RNT is Holmium-166 (Ho-166). Applied directly, Ho-166 emits β^--radiation with a maximum energy of 1.85 MeV. Ho-166 is used in treating liver tumours, liver metastases and for bone marrow preparation for transplantation. The radioisotope has a short half-life (26.8 hours), which limits the dose that can be delivered to the patient. The effectiveness of treatment with Ho-166 could be improved by using a so called *in vivo* Dysprosium-166(Dy-166)/Ho-166 generator. Dy-166 decays to Ho-166 by emitting a β^--particle with maximum energy of 481 keV. The half-life of Dy-166 is 80.6 hours, which allows an increase in the radiation dose given to the disease tissue when the Dy-166/Ho-166 generator is used instead of solely Ho-166.
Although promising, a process known as internal conversion (IC) makes the application of the Dy-166/Ho-166 generator with conventional carriers difficult. IC is a decay process in which an excited nucleus interacts with one of its orbital electrons. This causes an electron to be emitted from one of the inner electron shells. The cascade of electrons that follows to fill the hole that is formed can cause a valence electron to be ejected and leave the isotope with a net positive charge. This could lead to repulsive forces between the radioisotope and the carrier. In the case of the decay of Dy-166 to Ho-166, it can cause 72% of the Ho-166 to be liberated from the carrier molecule. The freed Ho-166-ions can accumulate in the liver, spleen, kidney and bone and may cause severe effects on patients. [5] A solution to retain Ho-166 and the Dy-166/Ho-166 might be to use nanocarriers for RNT applications.

Nanocarriers form the basis of new-found interest in the biomedical application of nanotechnology. Nanosized carrier systems can better penetrate target tissue, allow an efficient drug delivery, facilitate easier drug uptake by cells and ensure treatment of the targeted location. This last factor is the main benefit of nanocarriers: they can be tailored to be target-specific since there exists a great variety in physiochemical properties, morphologies and functions.
Polymeric micelles, which are core-shell nanostructures scaling from 10 to 100 nm, offer a range in composition and have shown to posses good stability, to increase the solubilization of hydrophobic drugs and to protect encapsulated drugs from biological surroundings. Where larger particles would be cleared rapidly by the reticuloendothelial system, polymeric micelles extend the circulation time of the encapsulated drugs significantly by their protective hydrophilic shell. [6]

In a study performed by Liu et al. [7], a novel method was discovered for the fast and simple radiolabelling of polymeric micelles to follow the fate of nanocarriers in chemotherapy. Different radioisotopes (Indium-

111, Lutetium-177 and Zirconium-89) were introduced to the micelles as aqueous hydroxides (for example $In(OH)_3$ (aq)). Both the radiolabelling efficiency and the stability were found to be 80% or higher. The high labelling efficiency and stability were attributed to an hypothesized interaction mechanism between the aqueous hydroxides and the micelles. The idea was that the aqueous hydroxides easily penetrated the hydrophilic micelle shell and formed solid precipitates in the micelle core at sufficient concentrations. These solid precipitates were then retained inside, giving rise to the high stability.
The hypothesized interaction mechanism needs further exploration to confirm its workings for the effective radiolabelling of polymeric micelles with other metallic species. The focus of this thesis is to extend on the work done by Liu et al. [7].

1.1. Research goal

The main goal of this thesis is to investigate and understand the loading mechanism of metallic species and polymeric micelles. The focus in particular is on Dy and the Dy-166/Ho-166 generator. The second goal is to determine whether Ho-166 remains inside the micelles under the effects of internal conversion.
Initially, the optimal loading conditions for the Dy-166/Ho-166 generator into the micelles are studied. This includes finding appropriate pH values, metal ion concentrations, type of buffer and influence of loading time. The stability of the Dy-166-/Ho-166-labelled micelles is tested and determined with high-resolution gamma radiation measurements. As micelles based on the amphiphilic block copolmyer poly(ϵ-caprolactone-b-ethylene oxide) (PCL-b-PEO) with molecular weight [2800-2000] were found to have highest stability [7], they will be the micellles subject to studying.
Radiolabelling experiments with Ga-68 are performed as well to confirm the loading mechanism established by Liu et al. [7] and this thesis. Once the loading mechanism is understood, predictions can be made for the radiolabelling of micelles with other metallic species for efficient encapsulation and good stability.

The report is set up as follows: chapter 2 contains relevant background theory and information on radionuclide therapy, the loading mechanism and experimental characterisation. Chapter 3 describes the used methodology for the experiments, including the production of the radionuclides and the loading procedure. The results for Dy/Dy-166, Ho-166 and Ga-68 are presented in chapter 4, which are further discussed in chapter 5. Additional information can be found in Appendix A and B.

2

Theoretical background

2.1. Radionuclide therapy

The application of radionuclides in nuclear medicine are found in both diagnostics and internal radiotherapy. Each application demands a specific radionuclide, the choice of which depends on its decay properties. Two physical considerations in internal use of radionculides are: imaging suitability and radiation dose delivered to the patient. [8] For radionuclide therapy, therapeutic radiopharmaceuticals are used for treatment of disease tissue. Radiopharmaceuticals are molecules consisting of a target-specific complex (a 'carrier'), such as an antibody(-fragment) or small molecules, bound to a radionuclide to deliver therapeutic doses of ionizing radiation to target cells. [7, 9] During cancer treament with RNT, the radiolabelled carrier is inserted intravenously or via ingestion and circulates the body to locate the cancer cells, where it deliveres a (lethal) dose of radiation to target cells. [7, 9]
An example of a delivery system is an antibody with the ability to bind to an antigen-expressing tumor, thereby increasing the dose delivered to the target cells and decreasing the dose to regular tissue. [10] Figure 2.1 shows a schematic of this example.

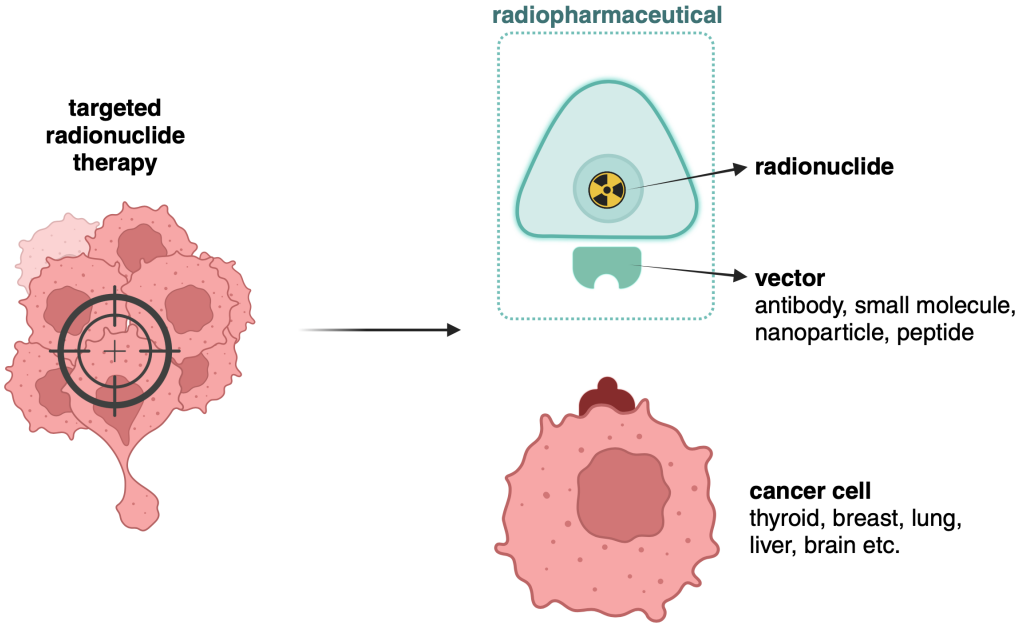

Figure 2.1: A schematic of the basic principle of radionuclide therapy using a anti-body carrier to deliver a radionuclide to an antigen-expressing tumor. The radionuclide emits radiation close to the target tissue (tumor).

The most important target of radiation is the nuclear DNA. The goal is to induce DNA strand breaks by direct ionization or by creating reactive products that produce chemical changes in the DNA. These reactive products are called Reactive Oxygen Species, which are highly reactive chemicals formed by the ionization of oxygen, water or hydrogen peroxide. When a single strand in DNA is damaged or breaks, the cell can often still repair the DNA. Double strand breaks in DNA are difficult to repair for the cell and are primarily responsible for cell death. A localized delivery of controlled doses of ionizing radiation induces DNA breaks that in turn set cell death in (tumour) cells in motion. [9, 11]

During treatment with RNT, the carriers are introduced into the body while the attached radionuclides emit radiation. During this period, both targeted and non-targeted sites will receive a radiation dose. Depending on the radiation energy, the effects on tissue can be critical, especially if the ionizing radiation is highly energetic. [10, 12, 13]
The crucial considerations for radionuclides are emission type, energy/range of emission and half-life. Mainly, the three types of emission considered are β^--particles, α-particles and Auger electrons. Historically, β^--emitters have received the biggest focus. [10] The damage path length in soft tissue ranges from 50 to 12000 μm with a Linear Energy Transfer (LET) of 0.2-2.0 keV/μm. β^--emitters are able to uniformly target the entire tumour site when the emission range exceeds the dimensions of the tumour. It makes β^--emitters a beneficial option in treating solid tumours, which are heterogenous aggregates of many cell types, including cancer (stem) cells, connective-tissue cells and immune cells. [10, 14, 15]

α-emitters produce high energy particles (4-9 MeV) that have a distance range of 40-100 μm. They are characterised by dense damage paths with high LET (50-230 keV/μm). [10, 16, 17] The short range limits therapy with direct α-emission to the targeted cell and immediate neighbouring cells. In contrast to β^--emitters, a low number of nuclear paths (1-3) are generally needed to kill a cell with an α-emitter. α-emitters have therefore been implemented to effectively for treatment of leukaemias, highly vascularized tumours, bone-marrow purging for transplant preparation, neoplasms and micrometastases. [10, 17, 18, 19]

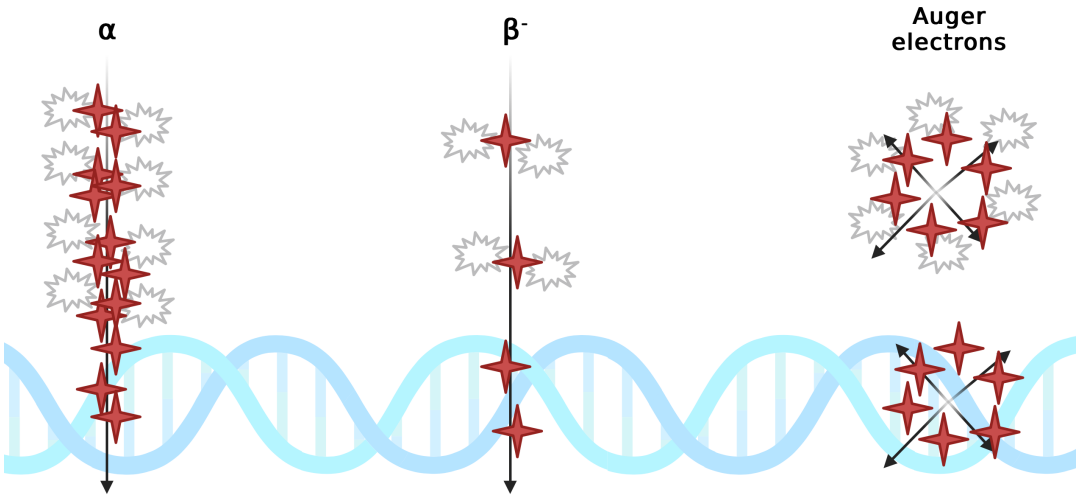

Figure 2.2: A schematic representation of the effect of α-particles, β^--particles and Auger electrons on DNA. α-particles: range 40-100μm, LET 50-230 keV/μm. β^--particles: range 50-12000 μm, LET 0.2-2.0 keV/μm. Auger electrons: range 0.002-0.5 μm, LET 4-26 keV/μm. The red stars represent particle interactions to create direct or indirect ionization. The grey bursts represent the formation of ROS. Image created with Biorender, idea taken from [18].

Radionuclides emitting Auger electrons are generally effective only when the carrier is able to penetrate the cell membrane and reach the nucleus. The Auger electron range is 0.002 to 0.5 μm with an LET of 4-26 keV/μm. A clinical purpose of Auger electrons is for irradiation of microscopic residual disease (nanometer and subnanometer dimensions), but in practise they are not yet used often. [10, 17, 20, 21].

Figure 2.2 schematically shows the impact of β^--particle, -α-particle and Auger electron emitters on DNA and the formation of ROS. ROS are responsible for around 70% of DNA damage during radionuclide therapy. Direct DNA damage accounts only for 30%. It means that there is great dependency on oxygen and oxygen species for RNT to be effective in treating disease sites. [18]

The final consideration, but crucial due to its practicality, is the effective half-life of the radiopharmaceutical. The effective half-life is the time required for the activity of a particular radionuclide deposited into the body to be reduced by 50 percent of its initial value as a consequence of its radioactive decay combined with biological elimination. [22] It is generally calculated with

$$\frac{1}{T_e} = \frac{1}{T_p} + \frac{1}{T_{bio}} \tag{2.1}$$

with T_e the effective half life, T_p the physical half life and T_{bio} the biological half life. It should be optimal regarding the time that is required to prepare the radiopharmaceutical, its delivery to the clinic, administration to the patient and localization in and around the target site. An optimal physical half-life for the (parent) radionuclide for therapy ranges from six hours to seven days. [18, 23] The biological half-life depends on the carrier used for the radiopharmaceutical. If the biological half-life is too short, for example, the radionuclide will be quickly eliminated from the body, resulting in inefficient treatment. Therefore, a balance between the physical and biological half life should be chosen for effective radiation delivery. This choice should be made based on the type of tumour, the method of administration and the uptake mechanism of the radiopharmaceutical by the tumour site. [23]

2.2. Therapeutic and diagnostic in vivo radionuclide generators

Radionuclides that are used in radionuclide therapy are often applied solely. During the localization period of the radiopharmaceutical, the radionuclide already emits therapeutic levels of radiation. This means that a major part of the initially added therapeutic dose is lost to healthy tissue. There is a concept to increase the therapeutic dose given to disease tissue during treatment. This concept involves the production of the therapeutic radionuclide (the daughter) from the *in vivo* decay of its parent nuclide. Ideally, a parent nuclide with a long(er) half-life decays to a daughter nuclide. Depending on the carrier molecule, this can increase the flexibility in localization time and increase the effective dose given to the target site. The system is called an *in vivo* generator. [10, 12, 13, 16]
Table 2.1 gives examples of in vivo generators that have been used or proposed for diagnostic and therapeutic applications.

Table 2.1: Examples of in vivo generators for biological and medical applications. [16, 24]

Parent	$t_{1/2}$	$E_{\beta^-,max}$ MeV	γ keV	Daughter	$t_{1/2}$	$E_{\beta^-,max}$ MeV	γ keV	Use
Rb-81	4.58 h	-	446, β^+	Kr-81m	13.1 s	-	190	Blood flow
Dy-166	81.6 h	0.402	82.5	Ho-166	26.8 h	1.85, 1.78	80.6	RNT
Pb-212	10.6 h	0.568	239	Bi-212	60.6 m	2.25	α 6.09	RNT
Ac-225	10 d	α	5.83	Fr-221	4.8 m	α 6.3	-	
				At-217	0.18 s	α 7.07	-	
				Bi-213	47 m	α 5.869	440	RNT
				Po-213	10^{-6} s	α 8.375	-	

For therapeutic purposes, the parent-daughter form a complex with an appropriate carrier. The parent radionuclide has a suficiently long half-life to allow localization of the carrier molecule to the target tissue. Ideally the parent decays during the localization period, while the daughter delivers destructive radiation to the target as it grows to reach equilibrium. [24]
An in vivo generator and its carrier must match to ensure the daughter radionuclide stays attached to the

carrier. In many cases, the chemical change from one atom to another atom is enough to cause a drastic difference between parent and daughter chemistry as a result of nuclear transformation. An example of such a transition occurs in the Rb-81/Kr-81m generator, data shown in table 2.1 When administered to the body, rubidium accumulates in cells due to its chemical similarity to potassium. Krypton-81m, the decay product of Rb-81, is inert and diffuses freely over cell membranes and is carried away by blood flow. [16, 24] The loss of radionuclides into the circulatory system of the body is usually undesired, as healthy tissue might be affected unintentionally. However, in the case of the Rb-81/Kr-81m generator, the Kr-81m is taken up by the blood flow and allows for measuring perfusion, which is the passage of fluid through the lymphatic system and the circulatory system to an organ or other tissue. It is an example of a chemical transition by nuclear transformation being used appropriately.

2.2.1. Parent/daughter equilibrium

In general, when a radionuclide decays, the activity can be described by the activity equation:

$$A(t) = A_0 e^{-\lambda t} \quad \text{or} \quad N(t) = N_0 e^{-\lambda t} \tag{2.2}$$

in which $A(t)$ is the activity in Bequerel (Bq) at time t (in s), A_0 the initial activity at t = 0, λ the decay constant in s^{-1} and $N(t)$ and N_0 the number of decaying nuclei at time t and t = 0 respectively. The decay constant λ is depended on the half-life of the radionuclide by:

$$\lambda = \frac{\ln(2)}{T_p}. \tag{2.3}$$

When a parent radionuclide decays into a stable daughter nuclide, there is no additional activity as a consequence of a decaying daughter. However, when the daughter nuclide is also radioactive, it again decays into a daughter nuclide. Thus, each radioactive parent nuclide can initiate a series of decays. Each decay product has its own characteristic decay constant. Between a parent and daughter radionuclide, radioactive equilibrium can be reached when the daughter is decaying at the same rate as it is being produced. The period is takes for equilibrium to settle depends on the decay constants of the parent and daughter nuclide and is typically expressed in terms of daughter half-lives. The activities of the parent and daughter radionuclides can be described by a set of first-order differential equations, called the Bateman equations. [25, 26] To start, the activity equation 2.2 can be expressed in N:

$$A_1 = -\frac{dN_1}{dt} = \lambda_1 N_1 \tag{2.4}$$

The subscript 1 denotes the parent, 2 and higher will stand for the daughter products. The number of nuclei or activity at t = 0 is denoted by for example N_1^0 and A_1^0. The number of daughter nuclei is determined by two processes: (1) its radioactive decay and (2) its production by the parent nucleus (or 'growth'), described by:

$$\frac{dN_2}{dt} = -\lambda_2 N_2 + \lambda_1 N_1 \tag{2.5}$$

The solution of this differential equation is:

$$N_2 = \frac{\lambda_1}{\lambda_2 - \lambda_1} N_1^0 (e^{-\lambda_1 t} - e^{-\lambda_2 t}) + N_2^0 e^{-\lambda_2 t} \tag{2.6}$$

and since $A_1 = \lambda_1 N_1$ and $A_2 = \lambda_2 N_2$, the activity of the daughter equals:

$$A_2 = \frac{\lambda_2}{\lambda_2 - \lambda_1} A_1^0 (e^{-\lambda_1 t} - e^{-\lambda_2 t}) + A_2^0 e^{-\lambda_2 t} \tag{2.7}$$

The second term in equation 2.7 is the residual daughter activity that was present at t = 0. More general, for a decay chain consisting of more than two nuclei, the concentration of the nth nuclide after time t is given by Bateman as [25, 26]:

$$N_n(t) = \frac{N_1^0}{\lambda_n} \sum_{i=1}^{n} \lambda_i \alpha_i e^{\lambda_i t} \quad \text{with} \quad \alpha_i = \prod_{j=1, j\neq i}^{n} \frac{\lambda_j}{\lambda_j - \lambda_i} \tag{2.8}$$

An equilibrium between the parent and daughter is not established immediately, but it has a transition period. The period it takes for equilibrium to settle depends on the decay constants of the parent and daughter nucleus. Two types of equilibrium can be distinguished:

Transient equilibrium occurs when the parent half-life is longer than the daughter half-life, or $\lambda_1 < \lambda_2$. In this case, the parent nuclide and the daughter nuclide decay at the same rate. [27] This type of equilibrium exists when the daughter half-life is not negligible compared to the half-life of the parent. An example of a parent/daughter nuclide pair that can be in transient equilibrium is the Molybdenum(Mo)-99/Technetium(Tc)-99m generator, which have half-lives of 66 hours and 6.1 hours respectively. [28] Figure 2.3 shows the relative activity of this generator system. As can be seen, the rate of daughter production is initially greater than its decay until it reaches a point where the production rate equals the decay rate.

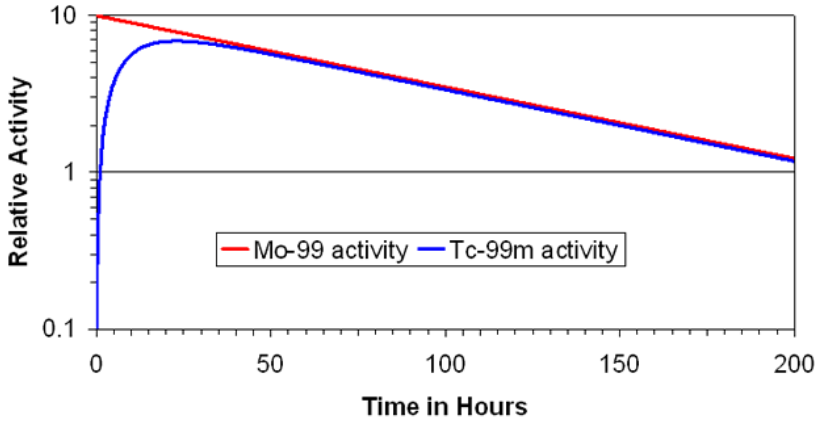

Figure 2.3: An example of transient equilibrium showing the relative activity of the Mo-99/Tc-99m generator. The rate of decay of the daughter equals that of the parent once equilibrium is reached. [27]

The term $\frac{\lambda_2}{\lambda_2 - \lambda_1}$ in equation 2.7 reveals the following. When the half-life of the parent is substantially greater than that of the daughter (and hence $\lambda_1 << \lambda_2$), the term comes close to 1. When the parent and daughter half-life are closer ($\lambda_1 < \lambda_2$), the term becomes greater than 1. That means that under transient equilibrium conditions, the daughter activity exceeds the parent activity. As the daughter's concentration increases, the daughter's decay rate will approach and eventually match the parent's decay rate. [25, 26, 27]
The time of maximum activity can be found using $\lambda = \frac{ln(2)}{t_{1/2}}$ and by differentiating equation 2.7 and equal it to zero. Then the time of maximum activity of the daughter is found with:

$$t_{max} = \frac{1.44 \times T_1 T_2}{T_1 - T_2} \times \ln(T_1/T_2) \tag{2.9}$$

with t_{max} the time of maximum daughter activity and T_1 and T_2 the half-lives of the parent and daughter. Once equilibrium is reached, the activity of the daughter nuclide can be described by assuming that A_2^0 = 0 and that the term $e^{-\lambda_2 t}$ is insignificant under ($\lambda_1 < \lambda_2$), giving the following expression:

$$A_2 \approx \frac{\lambda_2}{\lambda_2 - \lambda_1} A_1^0 e^{\lambda_1 t} = \frac{\lambda_2}{\lambda_2 - \lambda_1} A_1 \tag{2.10}$$

Secular equilibrium occurs when a long-lived radionuclide decays into a radionuclide with a comparably short half-life. The half-life of the parent nuclide is much greater than that of its daughter, meaning $\lambda_1 << \lambda_2$. [25, 27] With the assumption that A_2^0 = 0, the Bateman equation for the daughter activity (equation 2.7) reduces to:

$$A_2 \approx A_1^0 (1 - e^{-\lambda_2 t}) \tag{2.11}$$

The parent will not decay noticeable during many daughter half-lives. An example of a secular equilibrium generator is the parent/daughter system Rb-81/Kr-81m (see table 2.1) where the parent Rb-81

has a half-life of 4.58 hours and the daughter Kr-81m has a half-life of 13 seconds. Figure 2.4 shows the relative activities of a Rb-81/Kr-81m generator. Like for transient equilibrium, the daughter production rate increases until it reaches equilibrium. There, the activity of the daughter matches the activity of the parent.

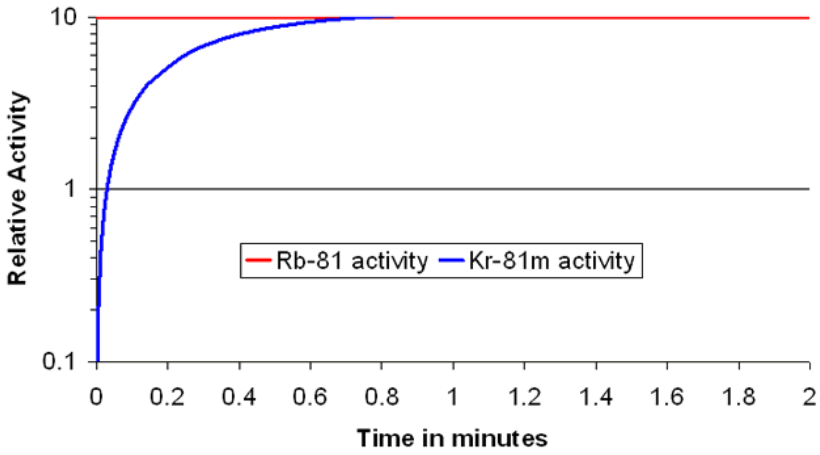

Figure 2.4: Secular equilibrium example showing the activity in the Rb-81/Kr-81m generator. [27]

No equilibrium is established when the half-life of the parent nuclide is shorter than the half-life of the daughter nuclide. The production rate and the decay rate of a daughter in the decay chain cannot match.

2.2.2. Dysprosium-166/Holmium-166 generator

A radionuclide currently used in radionuclide therapy is Holmium-166. It emits β^--particles with energies 1774.32 keV (48.8% yield) and 1854.9 keV (49.9% yield) and decays to the stable Erbium-166. It also emits gammas, with the 80.57 keV gamma having the highest yield (6.7%). The high energy β^--particles can be used for therapeutic effect and the 80.57 keV gamma for nuclear imaging purposes. Furthermore, Ho-166 can be visualized by CT (Computer Tomography) due to its high density. [12, 14, 15, 29] The half-life of Ho-166 is 26.8 h and the maximum tissue range of the β^--particles is 2.2 mm. It is reported by Klaassen et al. [14] that 90% of the total radiation dose is delivered in the first 2.1 mm. Ho-166 can be produced in two ways and it is mainly produced by neutron activation by (n, γ) activation of Ho-165. Ho-165 has a natural abundance of 100% and a cross section of 64 barns for the production of Ho-166. [12, 14, 15, 30]

Diagnostic and therapeutic applications

In clinical research, positive effects have been observed in patients with hepatocellular carcinoma (HCC) that were treated with Ho-166. Hepotocellular carcinoma is the most common type of primary liver cancer for adults and most common cause of death in people of end-stage liver disease.
In a study performed by Kim et al. [4], 42 of 52 patients with HCC showed complete tumour destruction after treatment with Ho-166 attached to a chitosan carrier. With the same carrier and Ho-166, another study confirmed that 70% of the patients with cystic brain tumours responded positively to the treatment. [14]
Other carrier/Ho-166 combinations have been studied to investigate their effectiveness. Examples are chelator molecules such as diethylenetriaminepentaacetic acid (DTPA) and different types of antibodies. In a study performed by Thompson et al. [31] the often used radioisotopes Yttrium-90 and Rhenium-188 for treatment of melanoma (form of skin cancer) was compared to treatment with Ho-166 in combination with an anti-milanin antibody. After injection of the antibodies labelled with the radioisotopes, Ho-166 showed comparable therapeutic effects to treatment with Rhenium-188. Additionally, no toxic effect was observed as a result of injection of the Ho-166 complex, whereas Y-90 was toxic and was insufficient in treating the tumour. [14, 31]
Furthermore, clinical studies and treatment with Ho-166 are currently done for liver cancer, non-resectable

tumours, head-and-neck neoplasms, neuroendocrine tumours in the liver, colorectal tumours, liver metastases, multiple myeloma (blood cancer that develops in plasma cells in the bone marrow), bone marrow preparation for transplantation, microbrachy therapy, kidney tumours, pancreas tumours and inflammation of joints. [14, 24, 32]

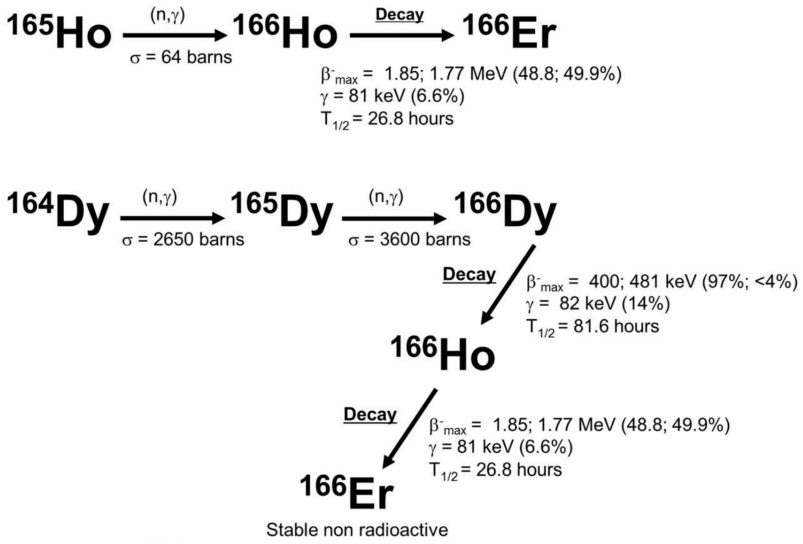

Figure 2.5: A diagram displaying the production methods for Ho-166 and Dy-166 [14]. The first diagram shows how Ho-166 is produced from ^{165}Ho by single neutron capture. A second method to produce Ho-166 is by double neutron activation of ^{164}Dy. Dy-166 will decay into Ho-166, giving rise to the Dy-166/Ho-166 generator. The energies, different decay types and half-lives are shown as well. [14]

In radiation therapy, the cumulative dose is the total radiation dose given in a series of radiation treatments. Compared to other often used radioisotopes for cancer treatment (such as phospohor-32, yttrium-90, iodine-131, lutenium-177 and rhenium-186) with half-lives between 2.7 and 14.3 days, Ho-166 has a relatively high dose-rate if the same initial activity is given due to its shorter half-life. [14]

Increase of Ho-166 treatment effectiveness

Although Ho-166 is already implemented in clinical studies and therapies for various diseases, its effectiveness could be further improved. In a study done by Stella, et al. [3] the effectiveness of HCC treatment with Ho-166 microspheres was studied. This study reported that 72% of the patients showed complete response, partial response or stabilization of the disease. Although treatment of diseases like HCC with Ho-166 is effective already (as reported by the same studies [3]), there is a way that treatment could be further improved. This could be done by using a nuclide that decays into Ho-166 to form an *in vivo* generator. A nuclide that decays into Ho-166 is Dysprosium-166.

Both holmium and dysprosium are part of a group of 15 rare earth elements called lanthanides. It is a group of elements that has become an established source of radionuclides for nuclear diagnostic and therapeutic applications. [14, 32]
Instead of forming Ho-166 by the single neutron capture of Ho-165, it can also be produced from neutron activation of Dy-164 following a (2n, γ) reaction to form Dy-166. The cross section of Dy-164 is 2650 barns. The Dy-166 nuclide will decay with a half-life of 81.5 h into Ho-166 under the emission of a β^--particle with a maximum energy of 481 keV. Like Ho-166, Dy-166 can be imaged due to the emission of a γ with 82.5 keV (14% yield). [12, 14, 15, 30] The production and decay of Ho-166 and Dy-166 are summarized in figure 2.5.
As the half-life of Dy-166 time is three times longer than Ho-166, the Dy-166/Ho-166 generator is capable of delivering higher radiation dose per administrated activity compared to treatment with Ho-166 alone. [12, 15, 30]

An example of an increase in treatment effectiveness is found in the study performed by Pedraza-Lopez et al. [33]. For the study, a potential candidate for the preparation of bone marrow transplantation was studied for treatment of hematologic malignancies (blood cancers). Prior to the transplantation, high local radiation doses were needed to destroy the old bone marrow. High doses generated by external radiation would cause damage to other organs. Therefore, bone-seeking radiopharmaceuticals were used to generate a high local dose and limit the dose given to healthy tissue. [14] The Dy-166/Ho-166 generator was attached to a bone-seeking agent, which was EDTMP (short for ethylene- diamine-tetramethylene phosphonic acid). The generator/bone-seeking agent combination was injected into the blood stream during animal studies. It was found that the skeletal uptake was 22%. The absorbed dose by the bone marrow with the generator system was 3.47 times higher than the dose from Ho-166 alone. The same study (Pedreza-Lopéz et al. [33]) reported considerable cytotoxicity and severe bone marrow suppression as a result of treatment with the Dy-166/Ho-166 generator.

The results in these studies [33, 24] are example of the succesful improvement of disease treatment with Ho-166 by implementation of the Dy-166/Ho-166 generator. Although promising, there is an important consideration for the Dy-166/Ho-166 generator that could cause instability of the carrier/radionuclide complex. This instability can arise as a consequence of a process known as internal conversion.

2.2.3. Internal conversion

Internal conversion (IC) is a proces that can occur after β^-- or α-decay has left a radionuclide in an excited state. It is an atomic decay process in which the excited nuclide interacts with one of the inner shell electrons. This results in the emission of a high-energy K-shell or an L-shell electron along with the creation of electron vacancies. As such, these electrons are not called β^--particles, since they do not originate from the nucleus of the atom. Where β^--particles typically have an energy range with a maximum value, IC electrons have a discrete sharply defined energy (K-shell, L-shell or even M-shell). Figure 2.6 schematically shows to process of IC for an excited state of Thallium-203.

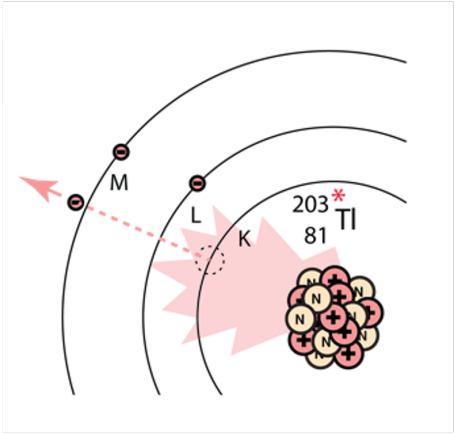

Figure 2.6: Schematic showing internal conversion occurring in an excited state of Thallium-203. A K-shell electron is ejected, thereby leaving an electron vacancy that will be filled by higher orbiting electrons. As a result, X-Rays, Auger electrons or both will be emitted. Image taken from [34].

The atomic number remains the same under internal conversion and it is an alternative to gamma decay. The hole that is created in the inner shell is filled by other electrons in higher shells. This can lead to a cascade of electrons that fill the holes that arise this way. The vacancies are filled by higher energy electrons. The excess of energy of the higher energy electrons is released in their transition to the lower energy shells. The transfer of energy to an outer electron orbit electron could cause the electron to be freed from the atom. This electron is called an Auger electron.
The process of internal conversion is one of the concerns of the stability of the Dy-166/Ho-166 generator. A study performed by Zeevaart et al. [5] looked into the radiolabelling and stability of the Dy-166/Ho-166 generator combined with a dodecane tetraacetic acid (DOTA) carrier. It was reported that 72% of the daughter Ho-166 was liberated from the DOTA complex. Zeevaart et al. [5] attributed the Ho-166 loss from DOTA to internal conversion. As a result, the de-excited Ho-166-ions became highly charged and attracted nearby electrons from the environment, which was the DOTA complex. Due to the electron transfer to Ho-166, the DOTA complex became positively charged, leading to a repulsive force that broke Ho-166 from DOTA. The freed Ho-166-ions can accumulate in the liver, spleen, kidney and bone and may cause severe effects on patients.

2.2.4. Gallium-68

In nuclear medicine, germanium-68 (Ge-68) is used as a generator for gallium-68 (Ga-68) to act as radio tracer for positron emission tomography (PET) and computed tomagraphy (CT) imaging. A Ga-68 PET/CT full-body scan can capture neuroendrocrine tumours (NETs) that overexpress somatostatin receptors and show the location of tumours in the body. [35, 36] Germanium-68 is a radionuclide that decays purely by electron-capture with a half-life time of $t_{1/2}$ = 270.95 days to the ground state of Ga-68. Ga-68 then decays by positron emission or electron capture to an excited state or the ground state of zinc-68 (Zn-68). Ga-68 has fourteen gamma transitions, thirteen of which have a combined probability of less than 0.4% from 5 excited level in Zn-68. The gamma transition with γ = 1077.35 keV has highest probability with 3.24%. [37, 38] Figure 2.7 shows the decay scheme of Ge-68/Ga-68.

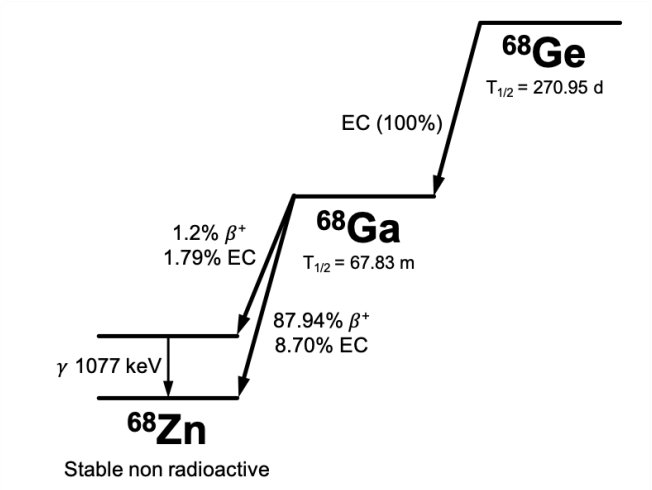

Figure 2.7: Decay scheme of 68-Ge and 68-Ga.

The positrons emitted by Ga-68 can have three different energies (with probability in %): 243,2 keV (0,00026%), 821,7 keV (1,20%) and 1899,1 keV (87,68%). [38] These positrons annihilate with surrounding electrons to form two gammas, both with an energy of at least 511 keV and that travel in opposite directions. The stable non-radioactive Zn-68 is in principle not toxic for the human body. Zinc is an essential trace element for all organisms. It is a component in more tan 300 enzymes and proteins and it is found in muscle, bone, prostate, liver, kidney, skin, lung, brain, heart and pancreas. [39]

2.3. RNT and nanocarriers

There are high expectations for the application of nanomedicine for solving various issues related to drug delivery. Nanocarriers are a promising option for the improvement of the water-solubility of hydrophobic drugs and the stabilization of easily degradable compounds. The treatment efficacy could be greatly improved with the potential of nanocarriers to promote drug retention in tissues, enhance cellular uptake and deliver drugs highly targeted. This is achieved by exploiting either the Enhanced Permeability and Retention (EPR) effect (see section 2.3.2) or a controlled drug release by internal (such as a biomarker or pH) or external stimuli (like temperature or ultrasound). Nanocarriers have been studied to help in diagnosis, treatment and monitor tumour evolution. [40] For RNT applications, nanocarriers are still under study and have yet to be implemented in the clinic.

Different types of nanocarriers exist, varying in physiochemical properties, morphologies and function, each with their own advantages and limitations. They are classified as: lipidic, polymeric, inorganic and peptide-based. Lipid-based nanosystems are lipid nanoparticles and liposomes, which are round-shaped structures of lipid bilayers with an acqueous core. Polymeric nanosystems are formed by natural or synthetic polymers to create several structures (nanoparticles, micelles and nanocapsules). These organic particles can be easily modified and stimuli responsive. [40, 6] Inorganic nanocarriers such as gold, silica or metal oxide nanoparticles have the ability to respond to external stimuli and allow easy surface modification. [15, 40] The advantages and limitations of some nanosystems are

summarized in table 2.2.

Table 2.2: Overview of the advantages and limitations of nanoparticles (NPs) in the field of drug delivery. These are either under study or used in clinical research. [40] *Dendrimers are branched, radially symmetric, dispersed polymeric systems.

nanoparticle (NP) type	composition	advantages	limitations
lipidic NPs	triglycerides fatty acids steroids waxes	multiple drug loading biocompatable biodegradable	complex & costly manufacturing
polymeric micelles	diblock polymer triblock polymer synthetic polymer natural polymer	loading hydrophobic drugs drug release regulation easy preparation	low stability in blood stream complex characterisation
dendrimers*	polyamidoamines polyamines polyamides	drug loading capacity	high toxicity non biodegradable
inorganic NPs	gold silver silica iron oxide zinc oxide	stimuli-response behaviour	high toxicity long-term effects unknown poor stability

The expectations and advantages of nanocarriers have not always been met. A couple of limitations are already mentioned in table 2.2, such as low stability, high toxicity or being non biodegradable. The production method of nanoparticles depends on many factors, like application, preparation material and loading capacity of the nanosystems. An appropriate method of production is required because the in vitro and in vivo performances of the nanocarriers depend on the material characteristics and might differ significantly. [41]
Another major factor of consideration is the scalability of the deployment of nanocarriers. The scalability of nanomedicine can be challenging due to complexity in production and physiochemical translation at the nanoscale level. Nanoparticles are often prepared by either nanoprecipitation (molecules forming nanosized single carriers) or by size reduction (milling of larger particles to nanosize). The formation of nanoparticles mainly comprises the use of organic solvents, centrifugation, homogenization and crosslinking (chemically joining two or more molecules by a covalent bond). The use of these chemicals or preparation methods on a large scale can lead to unacceptable limits from a production point of view. [40, 42]
Nevertheless, a growing number of nanocarriers receives approval for clinical trials due to their versatility, high targeting ability and variety to be tailored to specific treatments. [42, 43] A particular set of nanocarriers with easier preparation and higher scale-up feasibility are polymeric micelles. These smaller nanoparticles enable passive targeting to solid and poorly-permeable tumors and show a prolonged blood circulation time. [40] Therefore, it is this type of nanoparticles that is focused upon in this study.

2.3.1. Polymeric micelles as delivery system

Polymeric micelles are nano-sized drug delivery systems with a core-shell structure organized by self-assembly of amphiphilic block copolymers in aqueous solution. [40] The most commonly used polymers for micelles are diblock copolymers (composed of two different chemical blocks) and triblock copolymers (composed of three different chemical blocks). Typically, the block copolymers consist of a hydrophobic and a hydrophilic segment, making them amphiphilic.

In aqueous solution below the Critical Micelle Concentration (CMC), the amphiphilic copolymers exist seperately. Above the CMC, the copolymers spontaneously form polymeric micelles by aggregation. The number at which the individual copolymers form micelles is called the aggregation number. The hydrophobic segments form the core while the hydrophilic form the outher layer. The formation of the micelles is driven by the decrease of free energy in the system by the removal of the hydrophibic segments from the acqueous environment. Additionally, the hydrophobic segments attract under Van der Waals forces. When used as drug carriers in an acqueous environment, micelles solubilize poorly soluble (radio)pharmaceuticals within the micelle core, while polar molecules are absorbed by the shell of the micelle. [40, 42, 44] Figure 2.8 shows a schematic of polymeric micelle formation.

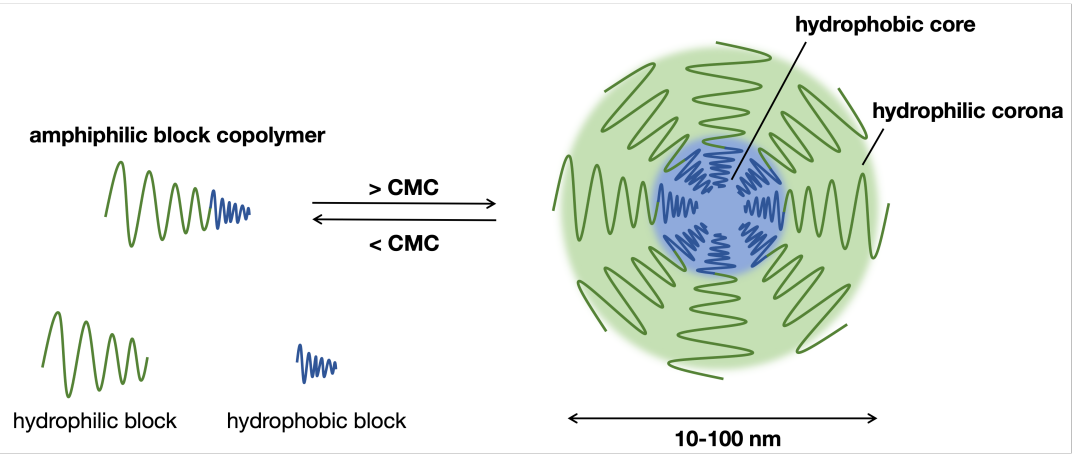

Figure 2.8: A schematic displaying the principle of the formation of polymeric micelles above the CMC. The amphilic block copolymers can form micelles of various shapes above the CMC. When the concentration of the polymers is below the CMC, they exist as unimers.

There are several advantages to using micelles as drug carriers [44]: (1) increase of solubilization of hydrophobic drugs and improved bioavailability; (2) reduction of toxicity and other adverse effects; (3) better permeability across physiological barriers, thereby increasing biodistribution of the drug; (4) certain amphiphilic molecules that form micelles extend the blood half-life of the micelle-drug complex; (5) the small size allows for spontaneous penetration into body tissue with leaky vasculature by the EPR effect (see section 2.3.2); (6) drugs inside micelles are well-protected from the biological surroundings trying to eliminate the foreign molecules introduced into the body.

Polymeric micelles offer a great variety in composition, which plays into their ability to be fine-tuned for specific theurapeutic applications. The typical size of these particles lays between 10 and 100 nm and they can vary structurally as core shell micelles, nanospheres and polymeric tubes. [40, 45] They posses good thermodynamic solution stability and the hydrophilic shell of the micelle prevents rapid elimination by the blood stream once the micelles are inserted into the body. [6] Another critical parameter is the low critical micelle concentration for polymeric micelles. Lower CMC values are advantageous for stable micelles, which is especially important concerning (radio)pharmaceutical applications. If a micelle has a high CMC value, it may dissolve into separate polymers on dilution with a large volume of blood. This induces the release of the encapsulated drug molecules or radionuclides. Micelles with low CMC values are more likely to remain stable even in large blood volumes. [44]

One requirement of polymeric micelles is to be biodegradable. Once degraded, *in vivo* non-toxic polymer fragments should be excreted through metabolic processes in the body. Two types of micelles that are biodegradable contain molecules such as poly-caprolactone (PCL) and poly-lactic acid (PLA), which can be decomposed by hydrolysis and enzymatic processes. [7] Combined with polyethylene oxide (PEO), PCL-PEO and PLA-PEO block copolymers can be formed that, under the influence of PEO, have longer circulation times. The hydrophilic PEO corona prevents rapid elimination from the blood stream [6], thereby increasing the circulation times.
Since the formation of polymeric micelles relies heavily on hydrophobic forces, the ability to alter the

hydrophobic and hydrophilic segments of the amphiphilic block copolymers allow a precise desiging of the nanoparticles. The physiochemical characteristics like the size and the loading capacity can be adjusted accordingly. This can be done by adjusting the molecular weight of the hydrophobic or hydrophilic blocks. Polyethylene oxide (PEO) is commonly used as hydrophilic block of nanoparticles with, for example, the hydrophobic PLA (polylactic acid) or PCL (poly-caprolactone) blocks. [45]

PEO is build with the basic monomer -(CH_2CH_2O)- and when dissolved in water, is characterized by hydrophilic interactions (hydrogen bonding of water molecules to the oxygen atoms on the monomer) and hydrophobic interactions (the remaining section of the monomer repels water). PEO can dissolve in water due to the formation of a hydration layer around the macromolecule. [46] The hydrophobicity of a copolymer like PCL arises from its abundance of methylene (-CH_2-) groups (five per monomer). The more methylene groups in a monomer, the higher its hydrophobicity. The combined amphiphilic poly(ϵ-caprolactone-b-ethylene oxide) (PCL-b-PEO) is shown in figure 2.9. It is a block copolymer undergoing various clinical studies on its biocompatibility, stability, structure, drug interaction and application in radio(chemo)therapy. [6, 7, 47, 48] Park et al. [6] concluded that the CMC for PCL-PEO polymers with a total molecular weight of 4800 g/mol is 9 mg/L.

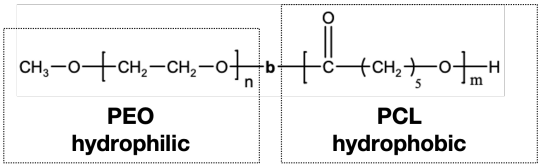

Figure 2.9: PCL-b-PEO polymer molecule.

Once formed, the idea is that these polymeric micelles will exploit the EPR effect to effectively treat tumour sites in the body. The next section will discuss that effect briefly.

2.3.2. The EPR effect

Passive targeting is based on the Enhanced Permeability and Retention (EPR) effect. The effect has been well observed in solid tumors of rodents, rabbits, canines and human patients. [49] It is based on three characteristics of solid tumors:

- The massive irregular build-up of and abonormalities in new blood vessels (neovascularization). The fast growing tumor tissue has urgent demands for nutrients and oxygen supplies, the tumor vessels are dense and convoluted. This leads to non-structured membranes and endothelial structures with openings. This makes the structures around the tumor tissue highly permeable to nutrients and other particles such as nano-carriers. [49]
- Elevated inflammatory factors sustain the EPR effect. This stimulates the permeability for nutrients and other particles to enter the tumour blood vessels. [49, 50]
- Reduced or lack of efficient lymphatic drainage. This results in the retention of molecules and other particles in tumor tissue and opens up the opportunity for passive targeting delivery of therapeutic agents. [50, 51]

The EPR effect is not always succesful in targeting therapy, since the strength of the EPR effect varies with type and location of tumors, local blood flow in tumours and the physiochemical properties of the therapeutic agents. [49, 52]

2.4. Interaction mechanism isotopes and micelles

In order to use micelles for the application in RNT, they must be loaded with radionuclides. The loading mechanism of chemical species with micelles was studied extensively by Liu et al. [7], with the main focus on loading indium species. The current work is an expansion on the study by Liu et al. [7], with different isotopes to test the described mechanism.

In the work by Liu et al. [7], the metal speciation of indium was determined with CHEAQS Next [53], which is a software that predicts chemical speciation of metal ions under different concentrations under different pH values. In the study, indium was added to micelles as indium chloride and according to CHEAQS, was expected to form In(OH)3 (aq) under spontaneous hydrolysis of indium chloride. It was observed that the indium ions form insoluble hydroxides once present in a HEPES (4-(2-hydroxyethyl)-1- piperazineethanesulfonic acid) buffer solution with neutral pH. When it was observed that indium

species, once added to a micelle solution, gradually entered the hydrophobic core of the micelles, a proposition for the loading mechanism was made. The idea was that the addition of indium to an aqueous micelle solution leads to soluble indium-hydroxides ($In(OH)_3$ (aq)) that can easily enter the micelle core via the hydrophilic shell. The increase of accumulated indium in the hydrophobic core lead to the formation of solid precipitates of $In(OH)_3$ (s). The idea was that it is difficult for these solid precipitates to diffuse or be taken out of the micelles. This gave rise to a high stability of the loading. [7, 54]
The loading mechanism is schematically shown in figure 2.10.

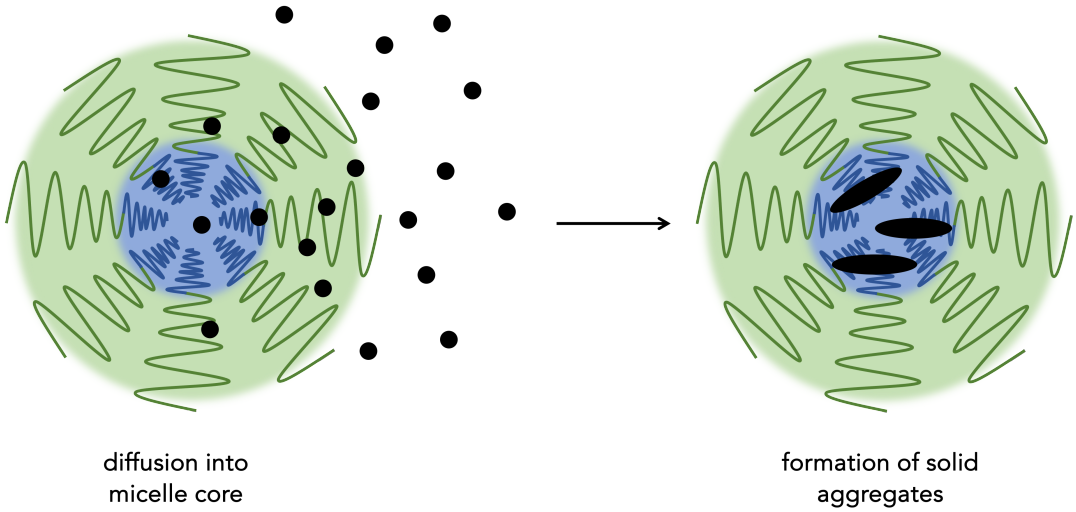

Figure 2.10: A proposed formation process of solid aggregates inside PCL-PEO micelles under diffusion of soluble aqueous isotope-hydroxides (black spheres). The larger black ovals indicate solid precipitates.

In the study by Liu et al. [54], the assumption was made that water is crucial for the diffusion process of isotopes getting into the core. It was stated that 'the less water content there is in the core, the less indium species would be found inside the micelles'. Fourier-Transform Infrared Spectroscopy was performed to determine if the chemical species encapsulated by the micelles and the micelle polymers would interact with each other. It was found there was no chemical interaction between the encapsulated chemical species and the polymers. It was then concluded that the hydrophobic nature of the polymers is the limiting factor in the interaction mechanism between isotopes/chemical species and the micelles. Another finding was to in order have a high labelling efficiency, metallic species should be loaded into micelles as aqueous hydroxides. When the concentration of the aqueous hydroxides would be high enough, they would form solid hydroxide precipitates, leading to a high stability. [7, 54]

Although hypothetical, this mechanism will be the basis of this thesis to determine if it is applicable for other chemical species as well, in particular: the Dy-166/Ho-166 generator and Ga-68.

2.5. Instruments and characterisation

2.5.1. DLS

Dynamic Light Scattering (DLS) is a spectroscopy method to determine the size distribution of particles like polymers, proteins and micelles in a solution or a suspension. In a DLS experiment, a laser provides a monochromatic source of light, which falls onto a solution with particles undergoing Brownian motion. The particles scatter light according to the Rayleigh scattering process. For Rayleigh scattering, the particle size should be sufficiently small compared to the wavelength of the incident light for the light to be diffracted in all directions with different wavelengths and light intensities.

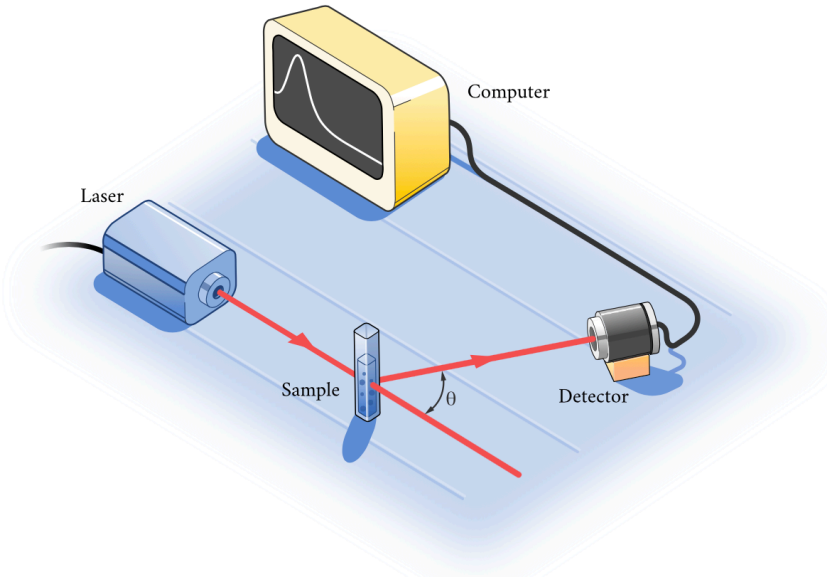

Figure 2.11: A schematic representation of a light-scattering experiment. [55] The laser light is scattered by the sample. The detector captures the scattered light, the intensity of which depends on the scattering angle θ. The angle is determined by the particle size in the sample.

As a result of Brownian motion, the distance between particles is changing constantly, resulting in a Doppler shift between the frequency of the incident light and the scattered light. The constructive and destructive interference of the diffracted light creates an intensity profile that changes over time. The rate at which the intensity fluctuates depends on the motion of the particles - smaller particles diffuse faster. The characteristics of the scattered light can be analyzed and reveal the size distribution of the particles. [55]
Typically, the light from the laser passes through a polariser onto the scattering sample. The scattered light is measured by the detector at an angle θ = 90°. The detectors used in a DLS instrument are either a photomultiplier or an avalanche photodiode. This signal is then passed from a spectrum analyzer to determine the particle size. [55, 56]
The size distribution is calculated by measuring the diffusion coefficient D of the particles. From this, the hydrodynamic radius R_H of the particles is determined with the following equation:

$$D = \frac{k_B T}{6\pi\eta R_H} \tag{2.12}$$

in which k_B is the Boltzmann constant, T the temperature and η the viscosity. The hydrodynamic radius R_H is defined as the apparent radius of a particle or molecule as it moves through a solution. [55, 56]

2.5.2. Size exclusion chromotography

Size exclusion chromatography is a separation method for a mixture of molecules and particles in solution based on their size, shape and molecular weight. It is extensively used in separation of biomolecules like sugars, proteins, lipids but also natual polymers. The process of size exclusion

chromatography (SEC) involves the use of a stationary phase (a gel or a resin) held in a column, which allows a liquid phase to pass through. SEC resins consist of a porous matrix of spherical particles that lack absorptive and reactive properties. As a sample mixture enters the column, larger molecules cannot diffuse through the pores and will diffuse first. Smaller particles elute in order of decreasing size. An example is shown in figure 2.12, showing larger particles diffusing faster than smaller molecules. The system is typically eluted with a suitable mobile phase (often a buffer) to maintain a constant environment. [57, 58]
Different gels and resins have a so-called fractionation range, which is the optimal molecular weight range that will allow good linear separation. Fractionation ranges from 100 to 7000 g/mol are appropriate for peptides, other small biomolecules and smaller proteins while a range of 100 000 to 300 000 g/mol is best for separation of antibodies and larger proteins. The degree of separation between different particle sizes is called the resolution. [57, 58] As can be seen in figure 2.12, particles of different sizes form so-called bands as they traverse through the resin. Good separation is typically achieved if the molecular weight of the different particles differs at least by 10%.

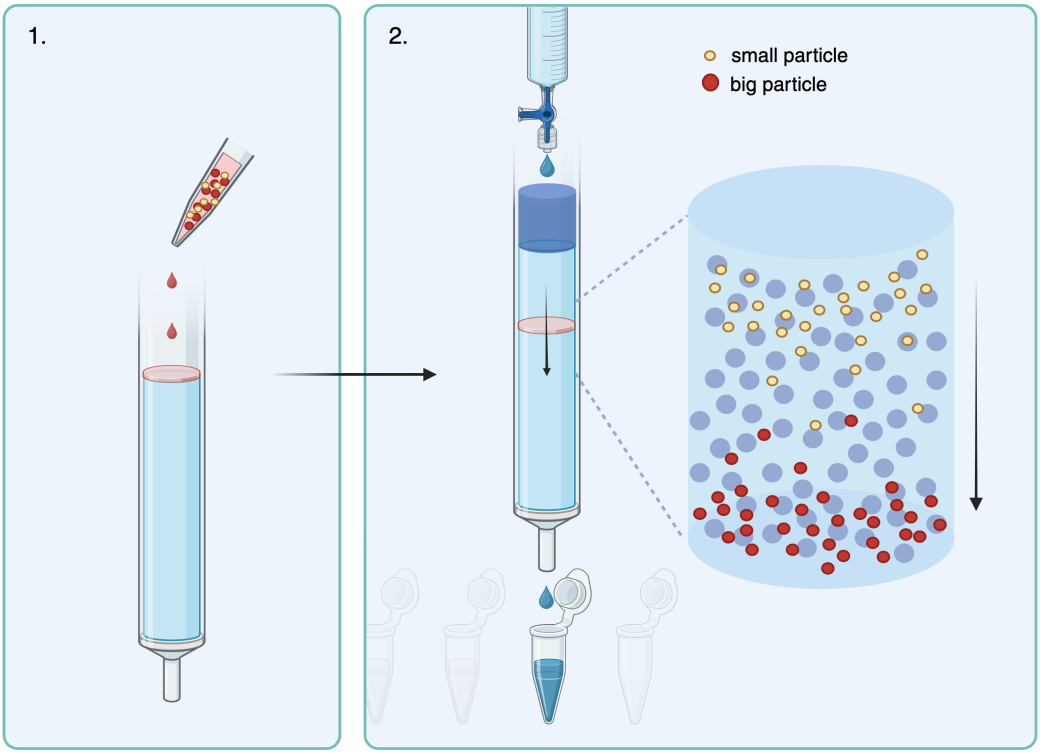

Figure 2.12: Schematic showing the working principle of size exclusion chromatography. 1. Shows the addition of a mixture of larger (red) and smaller (yellow) particles. 2. Shows how seperation of the mixture takes place when an eluent is added to the column. The larger, red particles diffuse faster through the column and are collected in fraction vials. The smaller, yellow particles pass through the pores in the resin matrix and are therefore extracted at a later stage. Image created with Biorender [59].

Factors that affect separation in SEC are: column packing, column dimensions, flow rate, sample volume and mobile phase composition. The sample volume and flow rate must be kept low for an optimal resolution. Likewise, increasing column lengths improve resolution. Advantages of this separation method are ease of operation, re-usability of resins and gels after use, little temperature influence on resolution and high sensitivity. [57]
As stated, each size exclusion column has a range of molecular weight that can be separated. The exclusion limit defines the upper limit of the column range, above this limit, particles that are too large get trapped in the stationary phase of the resin. The permeation limit defines the lower limit of the molecular weight. All particles that fall below this limit elute as a single band.

2.5.3. Radiation detectors

Below, some background theory about the radiation detectors used in this project is given. The principles of the detector in the Perkin Elmer 2480 WIZARD2 3 inch Automatic Gamma counter are explained. The Germanium detector and higher sensitive Germanium detector are discussed subsequently.

Scintillation detection (Wallac Gamma Counter)

The Gamma counter uses a thallium (Tl) activated, sodium iodine (NaI) scintillation crystal as detector. This scintillation material has a small amount of Tl mixed into the NaI. Typically, scintillation light is produced when a fast, charged particle excites an electron in the NaI crystal from the valence band into the conduction band. This leaves a hole in the valance band. The impurities in the NaI crystal formed by Tl are called *activation centers* that allow the electrons and the holes in the crystal to recombine quickly under the emission of visible light. An attached photo-multiplier (PMT) than produces an electrical pulse proportional to the energy of the incident particle. A scintillation detector should convert the kinetic energy of the incoming particle linearly, meaning the higher the energy of the incoming particle, the stronger the resulting electrical pulse. [60, 61]

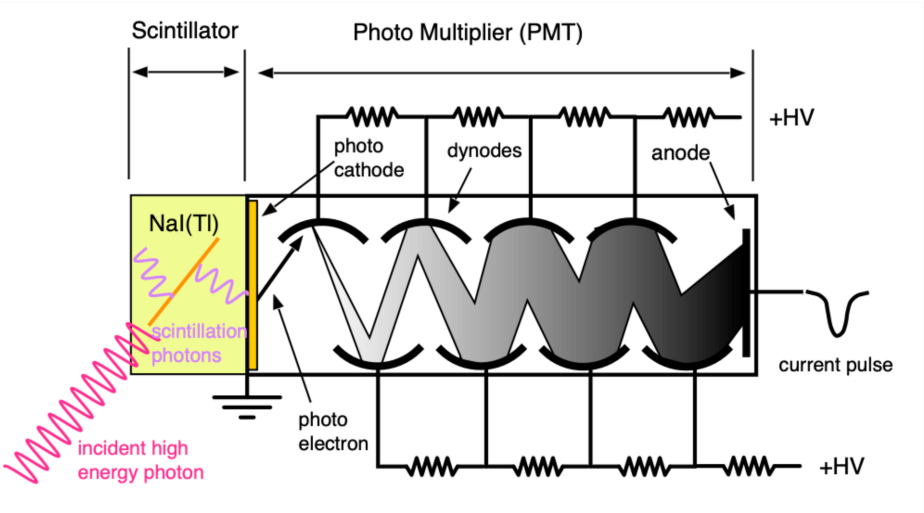

Figure 2.13: Schematic of a scintillation detector and a photo multiplier. [60] An incoming particle or photon interacts with the NaI crystal, which then emits a scintillation photon. The photon causes a cascade of accelerated electrons in the PMT. The signal strength depends on the amount of electrons detected at the anode.

A photo-multiplier is an instrument that detects scintillation photons. An incoming scintillation photon hits the photo-cathode, which releases electrons under the photo-electric effect. The released electrons are accelerated to a dynode, where it releases more electrons upon impact. Those are accelerated to the next dynode to produce more electrons. In the end, a cascade of electron reaches the anode, which is measured as an electrical pulse, the strength of which depends on the amount of electrons that reach the anode. An overview of the process can be seen in figure 2.13. [61]
Photons are detected if they interact to produce a fast charged particle that interacts with the scintillation material as described above. The measured energy is the energy deposited by particles that interact with the incoming high-energy photon. The most important photon-particle interactions in the scintillation detector are the photo-electric effect, Compton scattering, pair production and Rayleigh scattering. The dominant interaction is Compton scattering, which occurs for photon energies between 100 keV and 100 MeV. [60, 61]

Semiconductor detector (Germanium)

A semiconductor detector is an instrument that uses a semiconductor to measure incident radiation. In such a detector, the detector material is arranged between two electrodes. When the energy of an incident radiation particle is greater than the bad gap energy of the semiconductor material, it lifts an electron from the valence band to the conduction band. This creates an electron-hole pair. Under the

influence of an electric field, the electrons and holes move in opposite directions. This induces a current and detection occurs by measuring the current intensity. [62]

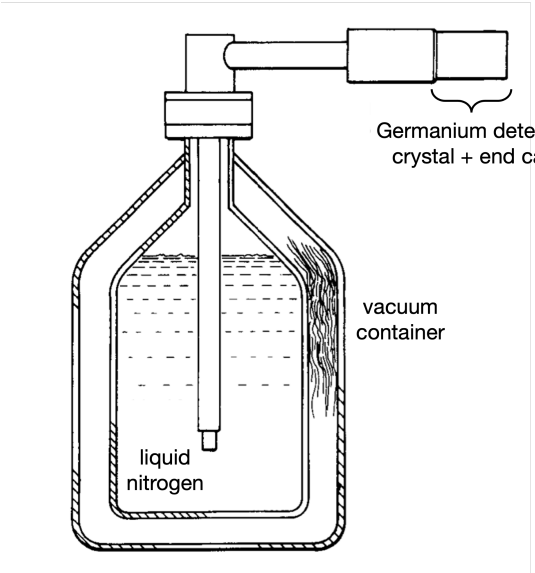

Figure 2.14: Schematic overview of a Ge detector with liquid nitrogen cooling. The germanium detector is housed at the top, closed off by an end cap to protect the crystal. It is connected by an cryostat to the cooling reservoir filled with liquid nitrogen. Image adjusted from [63].

Typically, the semiconductor material is Silicon (Si) or Germanium (Ge). The average energy needed to create an electron-hole pair is approximately 3.7 eV in Si and 2.9 eV in Ge. Germanium detectors are mostly used for gamma spectroscopy and X-Ray spectroscopy. Germanium is advantageous to choose here, since the higher atomic number (Z=32 for Ge) allows for a higher photoelectric cross section than silicon (Z=14). The detector material can be several centimeters thick in case of pure Germanium, allowing it to detect gammas up to a few MeVs. [62, 64]
Germanium detectors typically have a high energy resolution if the purity of the germanium crystal is high. But the band gap in germanium is smaller than that in silicon. This means that thermally generated charge carriers (electrons and holes) generate a potential detection problem. As a result, (nearly) all germanium detectors must be cooled with liquid nitrogen during their use. Additionally, the germanium crystal is housed inside a vacuum enclosure or cryostat that provides thermal contact with the liquid nitrogen. Figure 2.14 shows a schematic of a Ge detector with cooling.
The energy resolution of semiconductor detectors allows the separation of γ differing in energy by a few keV as opposed to a 20-80 keV resolution with NaI scintillation crystals. [65] This makes the use of semiconductor detectors favorable when the resolution of the radiation detection is critical.

3 Methodology

Firstly, an overview of the different chemicals used in this study is provided in table 3.1. The preparation of the PCL-b-PEO [2800-2000] micelles as well as the loading of the radioisotopes are based on the research done by Liu et al. [7]. The production the Dy-166/Ho-166 generator and the milking of Ga-68 are discussed. The specifics about the SEC separation method and the details about the loading tests are provided as well. Lastly, information about the measurement devices are given and data analysis and error calculations are addressed.

3.1. Materials

Table 3.1: The used chemicals listed with their CAS number and supplier.

Chemical	CAS Number	Supplier
Chloroform	865-49-6	VWR Chemicals
DTPA	67-43-6	Merck Sigma
Dy_2O_3	1308-87-8	Sigma Aldrich
$Dy(NO_3)_3{\cdot}5H_2O$	SC197180	Alfa Aesar, Thermofisher GmbH
Ga-68	-	Ge-68/Ga-68 generator
$Ga(NO_3)_3{\cdot}H_2O$	SC199263	Merck KGaA
H_2O (milli-Q water)	-	Merck Millipore
HCl	7647-01-0	VWR International
HEPES	7365-45-9	Sigma Aldrich or Carl Roth
MES	1266615-59-1	Merck Sigma
NaOH	1310-73-2	Merck Sigma
PEO-b-PCL [2800-2000]	SC087472	Polymer Source, Inc.
Sephadex G25	9041-35-4	Merck Sigma

The weighing of chemicals was done with the Mettler Toledo AG245 Analytical Balance. The pH of non-radioactive substances such as unloaded micelles, buffers and other compounds were measured with a Metrohm 691 pH Meter.

3.2. HEPES and MES buffer

HEPES was used to maintain a constant pH in the loading experiments of micelles with dysprosium. The HEPES (MW = 238,31 g/mol) buffer solution was made by adding 4.766 gram to 1 L of MQ water

to make a 20 mM buffer solution. The pH was then adjusted with NaOH pellets to the desired value. For a 1 L buffer solution with a pH 6.8, 1.5 NaOH pellets were added. For a 1 L buffer solution with a pH 7.5, 3 NaOH pellets were added. For a pH 8, 5-6 NaOH pellets were needed.

Likewise, MES buffer (2-(N-morpholino)ethanesulfonic acid) or $C_6H_{13}NO_4S$)) and HEPES buffer were used for experiments with Ga/Ga-68. It has a useful range of pH 5.5-6.7 and has a molecular weight of 195.24 g/mol. For a 20 mM MES stock solution, 3.905 g was added to 1 L of MQ water. Again, NaOH pellets were used to adjust the pH of the solution. For pH 5.5, 1 NaOH pellet was needed. For pH 6.5, a total of 7.5 NaOH pellets were added.

3.3. Synthesis of polymeric micelles

The micelles were prepared according to the solvent evaporation method. Typically, 20 mg of polymer stock (PCL-PEO [2800-2000]) was mixed in 200 μL chloroform under sonication for 20 minutes. Sonication was done with a BRANSON 200 ultrasonic cleaner. This mixture was added dropwise to 2.3 mL MQ and left stirring overnight to let the chloroform evaporate. This gave a polymer concentration of 8.7 g/L, well above the CMC. A 220 nm cut-off filter was used to remove large aggregates in the polymeric micelle-MQ mixture.
To confirm micelles were formed, DLS measurements were performed. The expected hydrodynamic radius of the formed micelles was 20 nm [7] for this particular copolymer, confirmed by the DLS measurement found in appendix A.

3.4. Production of Dy-166

Dysprosium-166 was produced using two different compounds: dysprosium(III) nitrate pentahydride ($Dy(NO_3)_3{\cdot}5H_2O$) and dysprosium(III)oxide (Dy_2O_3). $Dy(NO_3)_3{\cdot}5H_2O$ was used for experiments with lower activity (0.6-3.0 MBq/mL after cooling). 15+/-1.9 milligrams of $Dy(NO_3)_3{\cdot}\ 5H_2O$ was irradiated in a polyethylene rabbit for 10 hours (TU Delft Reactor Institute, BP3, thermal neutron flux 4.89 $\times$ 10^{16} s^{-1} m^{-2}). After a cooling time of 55 hours, the total activity of ^{166}Dy and ^{166}Ho was calculated in VIPS to be around 3 MBq. Other isotopes were formed as well (N-14, Dy-156, Ga-157, Tb-157, Dy-157, Dy-158, Dy-159), all with either a negliglibe activity (a few Becquerel), a short half-life (2-8 hr) or both. After irradiation, the $Dy(NO_3)_3{\cdot}\ 5H_2O$ was dissolved by adding it to 1 or 5 mL of MQ. The amount of MQ depended on the desired dysprosium concentration in the stock.
Dy_2O_3 was used for experiments with higher activity (30 MBq/mL after cooling). 5+/-0.25 milligrams of Dy_2O_3 was put in a quartz tube and irradiated for 5 h (TU Delft Reactor Institute, smallBeBe-L, thermal neutron flux of 4.24 $\times$ 10^{17} s^{-1} m^{-2}). After a 60 h cooling period, the total Dy-166 and Ho-166 was calculated in VIPS to be around 30 MBq. After cooling, the quartz tube was opened, 200 μL 1M HCl was added to the tube and it was placed on a heater (50 degrees Celsius) until the irradiated Dy_2O_3 was completely dissolved. Afterwards, 1M and 0.1M NaOH solution was added to adjust the pH to be in the range 5-6. Depending on the amount of milligrams of Dy_2O_3, 120-135 μL 1M NaOH was added. Although a pH meter was available, the pH was checked with pH paper to prevent radioactive contamination of the meter. The NaCl salt that formed when NaOH was added to the HCl was incorporated in the ion speciation study.

3.5. Milking Ga-68

The extraction (better known as 'milking') of Ga-68 was done from the Ge-68/Ga-68 generator from Eekert & Ziegler IGG100 and IGG101 GMP, Pharm. Grade. The Ga-68, generated by Ge-68 decay, was eluted from the column with 0.1 M HCl.
The activity of Ge-68 in the Ge-68/Ga-68generator was 329 MBq on October 13th, 2020. The experiments with Ga-68 were done in August 2023, meaning the activity of Ge-68 in the generator was around 22.5 MBq.
To estimate the concentration of Ga-68, the 5 mL eluent was collected in 1 mL fractions after running through the G10$^-$68/Ga-68 generator. These fractions were measured with a Wallac Gamma counter. The efficiency of the Wallac for Ga-68 (measuring the 511 keV annihilation gammas) is 0.0321 Bq/cpm. From the counts per minute from the Wallac, the activity and hence the amount of Ga-68 were calculated with the relation:

$$A = \text{efficiency} \times \text{measured counts} = N \times \lambda = N \times \frac{\ln(2)}{t_{1/2}} \tag{3.1}$$

with A the activity, N the amount of atoms, λ the decay coefficiency and $t_{1/2}$ the half life time. Per fraction, the concentration of Ga-68 was determined. The estimated concentration Ga-68 in the stock solution was 7.9010^{-12} M, calculation found in Appendix A, section A.7.
For experiments with Ga/Ga-68 thereafter, the 5mL active Ga-68 was collected in one glass vial with a screw cap. The pH was then adjusted with either 0.1M or 1.0M NaOH to the desired pH. Typically, 0.5 mL 1M NaOH was added to have a stock Ga-68 with pH 7. It should be noted that the addition of NaOH created NaCl salt in the stock Ga-68. This was accounted for in CHEAQs analysis and revealed not to be of influence in ion speciation.

3.6. Loading procedure

The loading procedure as described below is based on the work done by Liu [7] for the Applied Radiation and Isotopes group at the TU Delft Reactor Institute.

3.6.1. Dysprosium/holmium

The stored micelle solutions were kept in vials with 2.3 mL MQ. In preparation of a loading experiment, 0.5 mL micelle stock (8.81+/-0.15 mg/mL polymer) solution was mixed with 0.5 mL 20 mM HEPES buffer (to create a 1 mL solution with HEPES 10 mM).

Dysprosium(III)nitrate

For the loading experiments with dysprosium, the first compound used was dysprosium(III)nitrate. The stock concentration dysprosium, made with 15+/-1.9 mg $Dy(NO_3)_3{\cdot}5H_2O$, varied between 6.84·10^{-3} M (diluted in 5 mL MQ) and 3.42·10^{-2} to 3.95·10^{-2} M (diluted in 1 mL MQ). The loading procedure was done by simply adding the target isotope solution to the stirring micelle and buffer mixture [7]. Typically, 10-20 kBq Dy-166 was added to the micelle-buffer mixture, the volume of which depended on the elapsed time to compensate for decay. This ranged from 0.0056 to 0.018 mL (for 1 mL dysprosium stock) or 0.088 to 0.365 mL (for 5 mL dysprosium stock). This was then left stirring for one hour, after which Size Exclusion Chromatography (SEC) removed the loaded micelles from the unloaded isotopes. The activity of the samples was measured before and after the seperation. The optimal loading conditions in PCL-b-PEO [2800-b-2000] were determined with dysprosium(III)nitrate.

Dysprosium oxide

The stock concentration dysprosium was made with 5.0+/-0.25 mg Dy_2O_3 in 1 mL MQ, leading to 2.2510^{-2} to 2.84·10^{-2} M Dy. Under optimal loading conditions, the added activity varied typically from 77 to 333 kBq, accounting to 0.025 mL of stock Dy solution. No change was made to the loading procedure. With dysprosium oxide, experiments were carried out to compare 1 hour loading to 18 hour (overnight) loading time. The activity of the samples were measured before and after SEC.
The optimal loading conditions were analysed beforehand with CHEAQs Next [53].

3.6.2. Gallium

A stock Ga-68 solution was produced by flushing 5 mL 0.1 M HCl through a Ge-68/Ga-68 generator. The pH of the collected Ga-68 stock is then adjusted with 0.1 M and 1 M NaOH solution. The loading procedure is similar to that of dysprosium by adding 50 μL of Ga-68 stock to the micelle/buffer sample and letting it stir for 1 hour. The added activity was 80 kBq and the concentration Ga-68 in the micelle/buffer samples is around 4·10^{-13} M (for the estimation calculation, see appendix A.7). The ion speciation for gallium revealed that for low concentrations, the most abundant species strongly varies (see appendix B) at different pH values. To study the influence of the different pH values, a variety of buffers was used to maintain a constant environment in the micelle samples. Next to HEPES (useful range pH 6.8-8.2), MES buffer was introduced as buffer agent, as it has a useful pH range 5.5-6.7. This allowed the exploration of more a acidic environment, in which $Ga(OH)_3$ can be the dominant species. The loading is therefore done for a maximum of 1 hour.

The influence of higher gallium concentrations on the loading efficiency was studied by adding non-radioactive $Ga(NO_3)_3 \cdot H_2O$ solution to the micelles/buffer samples. 50 μL non-active gallium stock with a concentration of 4.7 mM is added with 50 μL active Ga-68 to get a gallium concentration of 0.21 mM in 1 mL micelles + buffer. The ion speciation analysis shows that at $1 \cdot 10^{-}06$ M and higher, gallium forms Ga_2O_3 (s). Hence, the loading efficiency of $Ga(OH)_3$ (aq) and Ga_2O_3 can be compared directly.

3.7. SEC method

The unloaded isotopes were separated from the labelled micelles by size exclusion chromatography. The separation columns have a width of 1 cm and are filled with Sephadex G-25 fine resin, which has a pH stability between pH 2-13. The resin was prepared by mixing 56 gr of Sephadex with 500 mL of MQ water. The resin swells up in combination with water. Before used, it was left to swell for at least 3 hours at room temperature. The separation columns were prepared by filling them with 31+/-1.5 cm Sephadex resin and packing the resin by flushing 3 times 90 mL MQ through each column. Then, the column was flushed with 1-2 column volumes of buffer. During periods of non-use, the columns were kept wet with buffer solution to prevent dehydration.
For a separation procedure, the radiolabelled micelles were slowly added with a 2 mL disposable plastic pipet as to not disturb the resin too much. The vial containing the micelles was rinsed with 5 drops of buffer solution, which was then added to the column as well. The column tap at the bottom was opened and collection of fractions started as soon as the volume micelles disappeared in the resin. The 1 mL fractions were collected in plastic counting vials. The eluent was typically the buffer used in loading the micelles with a molarity of 10 mM (either HEPES or MES with appropriate pH and 10 mM concentration). Once seperation of the sample was complete, the columns were flushed with 40 mL 1M HCl and 90 mL 10mM buffer solution. The micelles typically appeared fraction 10-14.

3.8. DTPA challenge

The stability of the loaded micelles was tested by adding 0.1 mL diethylenetriaminepentaacetic acid (DTPA, 11 mM) to 1 mL of the ^{166}Dy/^{166}Ho or ^{68}Ga radiolabeled micelles (in 10 mM HEPES or MES buffer, varying pH). After stirring for 1h, 2h, 4h or 24h, the mixture was passed through a SEC column to seperate the free radionuclid10^{-}DTPA complexes and the radiolabeled micelles. The radionuclide-DTPA complexes were typically found in fractions 16-20, the radiolabeled micelles in fractions 10-14.

3.9. Characterisation

3.9.1. DLS

The dynamic light scattering (DLS) instrument was an ALV sp 125 s/w 93 goniometer equipped with a JDS uniphase 633 nm 35 mW laser, a Perkin Elmer Photon Counter and an ALV-599/epp electronis system. It was used to determine the hydrodynamic radius of the micelles. 1 mL of non-diluted micelle solution (produced as described in 3.3) was pipetted in a borosilicate glass cuvette and closed with a stopper. The measurements were done at room temperature (293 K) at a fixed scattering angle of 90° for 30 seconds. The scattering intensity against the hydrodynamic radius data was fitted in the ALV-5000 v3.0 correlator software with an exponential fit. The x-axis displayed the unweighted radius in nm.

3.9.2. Radiation detection

Wallac Gamma Counter

Most gamma measurements were performed with the Perkin Elmer 2480 WIZARD2 3 inch Automatic Gamma counter (see figure 3.1). The detector is a thallium activated, sodium iodine crystal with a height of 80 mm and diameter of 75 mm. The detector measures a sample from nearly all directions. The detector assembly is shieled with 50 mm lead and it has a measurable energy range of 15-2000 keV. The efficiency was determined by [66] (window 15-2000 keV):

$$\text{efficiency} = \frac{\text{CPM}}{\text{DPM}} \times 100\%$$

with CPM counts per minute and DPM disintegrations per minute. The gammas emitted by Dy-166 and Ho-166 are measured in a mix range 80-82 keV, which measures the gammas from Dy-166 and Ho-166 combined. Additionally, it measures a 340-460 keV range for Dy-166 alone. Ho-166 has a 80.6 keV gamma with 6.2% yield and Dy-166 emits a 82.5 keV gamma with 14% yield. The resolution of the Wallac Gamma counter is too low to make a distinction between the two gamma energies. Hence, the counted gammas were treated as having the same energy. The efficiency for the gammas of Ho-166 and Dy-166 is 7.5-8.0%. Ga-68 emits positrons that annihilate with surrouding electrons, hence the annihilation gammas with minimum 511 keV energy are measured. For Ga-68, the efficiency of measuring the 511 keV annihilation gammas is 0.0321 Bq/cpm, or 51.9%, provided by one of the technicians.

Figure 3.1: Perkin Elmer 2480 WIZARD2 3 inch Automatic Gamma Counter. [67]

Germanium detector

The germanium detector was a Princeton Gamma Tech model LG22 with nitrogen cooling from EG&G ORTEC AL30-0. It has mainly acted as a backup for radiation measurements during the period the Wallac Gamma Counter was under maintenance. Specifications about the detector like its size and material are unknown. Data acquisition and analysis was done with the Genie 2000 Gamma Acquisition and Analysis software, V3.2 (Mar 18, 2009) by Canberra [68].

Higher sensitive Germanium detector

The higher sensitive Germanium detector is a Canberra model GL2020R 7500L Cryostat with preamplifier 2002CPSL. With a detector area of 2000 mm^2 it has a resolution (in eV Full Width Half Maximum) of 400 eV and 680 eV at respectively gamma energies of 5.9 keV and 112 keV. On top is a 3 inch diameter aluminium end cap. It has a Zinc (Zn) window to allow low energy gammas to reach the detector.
The Zn window Ge detector is a Low-Energy Germanium detector (LEGe) that is able to differentiate the gammas emitted by Ho-166 and Dy-166. The detectable range is 6 keV - 3MeV with a maximum energy rate of 40000 MeV/s. The absolute efficiency of the detector is found in figure 3.2. For this detector, the 0.5mm thick Be Window in the figure was taken as the efficiency, as recommended by one of the technicians. This means that for a sample with minimum 10 kBq gamma activity and energy between 20 and 100 keV, the efficiency is around 2%. Data acquisition and analysis was done with the Genie 2000 Gamma Acquisition and Analysis software, V3.2.1 (Aug 26, 2009) by Canberra [69].

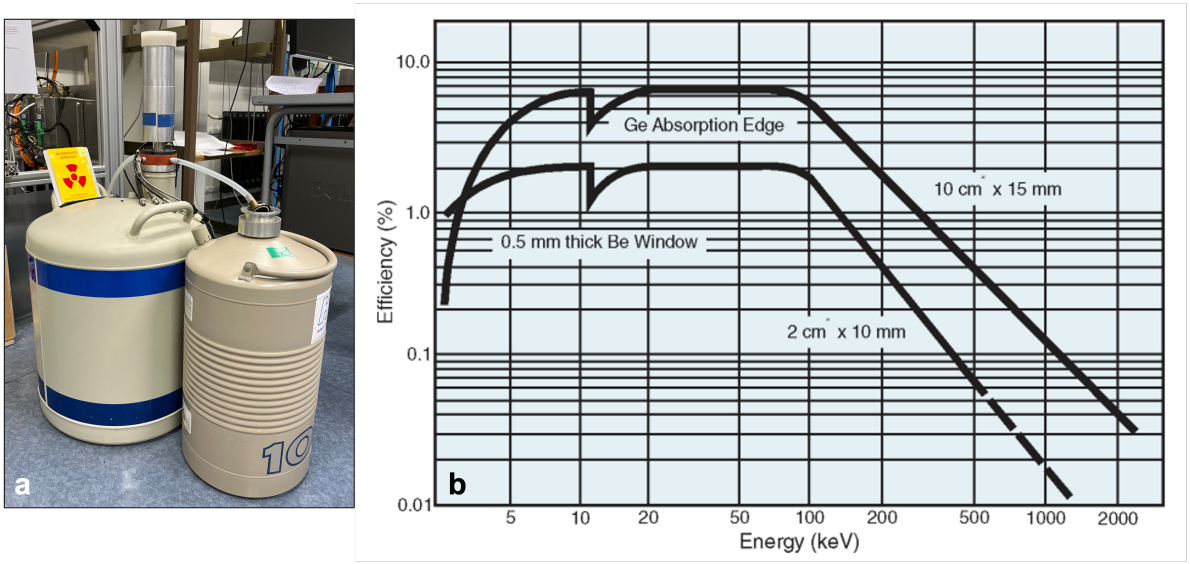

Figure 3.2: (a) The Canberra GL2020R LEGe detector and (b) the absolute efficiency curve as a function of energy for two detector sizes. The Ge absorption edge refers to the photoelectric absorption of x-ray photons close to the binding energy of the k-shell electrons of the absorbing atom. The Be (Beryllium) window denotes an optional protection window for the detector with a desired thickness. [64] The detector in (a) follows the 0.5 mm thick Be Window.

3.10. Data analysis

3.10.1. Radiolabelling and loading efficiency

The efficiency of the loading of the radioisotopes in the micelles was expressed as the radiolabelling efficiency. It was calculated as follows:

$$\text{RE (\%)} = \frac{\text{measured counts } ^{166}\text{Dy}/^{166}\text{Ho encapsulated in micelles}}{\text{measured counts of initially added } ^{166}\text{Dy}/^{166}\text{Ho}} \times 100\% \tag{3.2}$$

and

$$\text{RE (\%)} = \frac{\text{measured counts } ^{68}\text{Ga encapsulated in micelles}}{\text{measured counts of initially added } ^{68}\text{Ga}} \times 100\% \tag{3.3}$$

in which the measured counts were corrected for the decay of the radioisotope. The counts were measured with the Wallac Gamma Counter, the Ge-detector and the XRF detector.

3.10.2. Mass loading

The mass loading of an isotope loaded in the micelles was calculated as follows:

$$\text{mass loading (mol)} = \text{RE (\%)} \times \text{molarity isotope in stock (M)} \times \text{volume added to micelles (L)} \quad (3.4)$$

which gives the amount of moles of the isotope in the micelles. From the amount of moles, an estimation for the isotope concentration and hence its speciation in the micelle core were determined. Appendix A.3 shows how such an estimation was made.

3.10.3. Stability

The stability of the loading of radiolabelled micelles was expressed as loading retention. It was calculated as follows:

$$\text{retention (\%)} = \frac{\text{measured counts } ^{68}\text{Ga labelled micelles after DTPA and SEC}}{\text{measured counts } ^{68}\text{Ga labelled micelles before adding DTPA}} \times 100\% \quad (3.5)$$

for which only the fractions containing micelles are taken into account. Likewise, for the fractions containing the isotop10^{-}DTPA complex, the 'DTPA-complex' (%) was determined:

$$\text{DTPA complex (\%)} = \frac{\text{measured counts } ^{68}\text{Ga-DTPA after SEC}}{\text{measured counts } ^{68}\text{Ga labelled micelles before adding DTPA}} \times 100\%. \quad (3.6)$$

The same calculations hold for Dy-166 and Ho-166.

3.10.4. Error treatment

The sample measurements in this study were corrected by subtracting the background radiation. A background measurement was done directly before or after a series of sample measurements, to have similar measuring conditions for the sample and the background. The same measuring time was used both.

Samples containing Dy-166/Ho-166 were measured for 180 seconds on the Wallac Gamma Counter. With the regular germanium detector and the Zn window Ge detector, the measuring time was 300 seconds. Samples containing Ga-68 had a measuring time of 120 seconds on the Wallac Gamma Counter.

Detection errors

The three radiation detectors used in this study included detection errors automatically with each measurement. These errors were based on the amount counts within the measuring time window and the dead time. For statistically relevant results, the detector error for the Wallac Gamma Counter had to be below 10%, achieved typically at 100 CPM, or 4 times the background. For the regular Ge detector and the high sensitive Ge detector, the error had to be below 1%, achieved for samples with at least 10 kBq gamma activity.

The Wallac Gamma Counter had a dead time of 2.5 μs, thereby limiting the count rate to around 8 million CPM [66]. The dead time error was less then 1% for 2 million CPM. Above 8 million CPM, some gammas that do hit the detector will not be registered or corrected for. Efficiency and gamma yield included, the maximum total activity for Dy-166/Ho-166 containing samples could be 13.6 MBq and for Ga-68 containing samples 0.5 MBq.

Both the regular Ge detector and the high sensitive Ge detector are older detectors (respectively around 30 and 25 years old) and efficiency and resolution curves for these detectors have never been made.

Therefore, measurements done with either of these detectors will only be compared with other results gained from the same detectors. A quantitative distinction between the Dy-166 and Ho-166 to determine their ratios inside labelled micelles was measured with the high-res Ge detector.

Data error

The experiments done in this study were, unless denoted otherwise, performed in triplets. Standard variations (SD) represented experimental uncertainties and were used to express the errors in radiolabelling efficiency, mass loading, retention and Ge-detector gamma measurements. The standard deviation was calculated as follows:

$$SD = \sqrt{\frac{\sum (x - \mu)^2}{n}} \tag{3.7}$$

in which x represented a point in the data set, μ the mean of the data set and n the amount of data points within the set.

4

Results

This chapter contains findings for loading experiments with Dy-166/Ho-166 and for Ga-68 into PCL-PEO [2800-2000] micelles. The radiolabelling efficiency, the mass loading and the retention were studied under various pH values and isotope concentrations. The first part (section 4.1) discusses the findings for Dy-166/Ho-166. The results of the Ga-68 experiments are found in section 4.2. A comparison between the Dy-166/Ho-166 and Ga-68 results is made in chapter 5 (Discussion).

4.1. Dy-166/Ho-166 generator with PEO-b-PCL micelles

4.1.1. Chemical speciation

The chemical speciation for both dysprosium and holmium was determined with CHEAQS Next [53]. The tables containing the chemical speciation data can be found in Appendix B. The experiments were organized according to the chemical speciation predictions, of which the most important findings are discussed here.

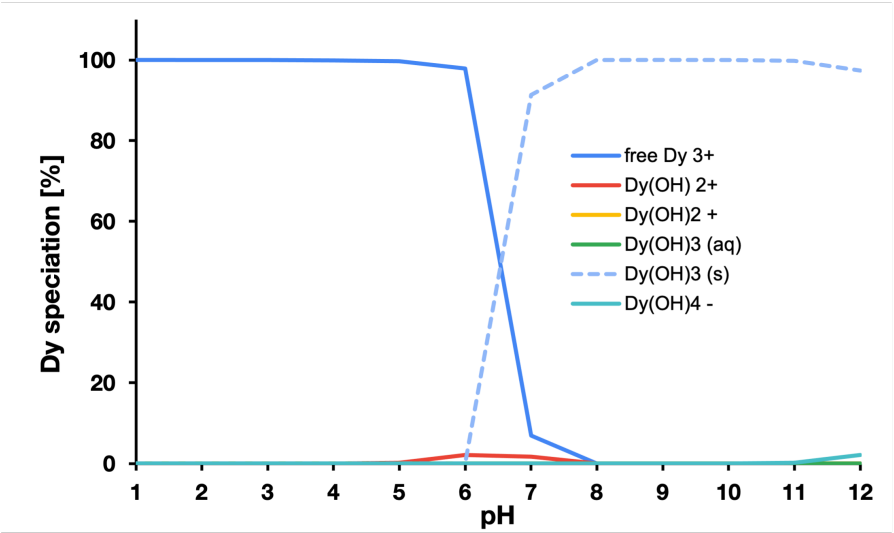

Figure 4.1: The speciation of Dy at chemical equilibrium as a function of different pH values. The Dy concentration was 0.2 mM, equal to 20 kBq of Dy-166 activity, the Cl^- concentration: 0.1 mM. The figure is based on plotted CHEAQS data points. For more details, see table B.8.

The minimum concentration of dysprosium was limited by the amount of activity that could be produced according to the methods as described in section 3.4. The irradiation of 15+/-1.9 milligrams of $Dy(NO_3)_3 \cdot 5H_2O$ caused around 1% of the dysprosium to become Dy-166. The minimum activity per micelle sample was 20 kBq. The minimum dysprosium concentration was therefore 0.2 mM. Since the

Dy-166 decayed, higher concentrations of Dy were needed maintain the minimum 20 kBq activity. As such, three different concentrations were chosen to run Dy/Dy-166 experiments with: 0.2 mM, 0.7 mM and 2.0 mM.

The three figures in this section display the speciation at the three different Dy concentrations: 0.2 mM, 0.7 mM and 2.0 mM. Figure 4.1 shows the speciation at [Dy] = 0.2 mM for varying pH values. The figure shows that six different species can exist: free Dy^{3+}, $Dy(OH)^{2+}$, $Dy(OH)_2^+$, $Dy(OH)_3$ (aq), $Dy(OH)_3$ (s) and $Dy(OH)_4^-$. Two of those species are overall dominant. At low pH and until pH 6, free Dy^{3+}-ions are nearly the only form of Dy. Between pH 6 and 7, there is a sharp transition from free Dy^{3+} to $Dy(OH)_3$ (s). Above pH 7, $Dy(OH)_3$ (s) is the only existing species, until $Dy(OH)_4^-$ comes up at pH 11.
Below, the chemical speciation graphs of Dy at varying pH for [Dy] = 0.7 mM and [Dy] = 2.0 mM an be found.

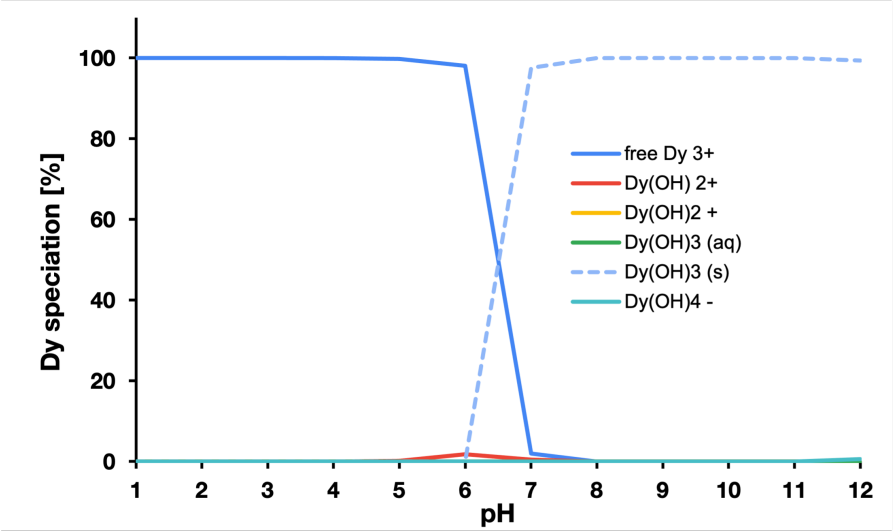

Figure 4.2: The speciation of Dy at chemical equilibrium as a function of different pH values. The Dy concentration was 0.7 mM, equal to 20 kBq of Dy-166 activity, the Cl^- concentration: 0.1 mM. The figure is based on plotted CHEAQS data points. For more details, see table B.9.

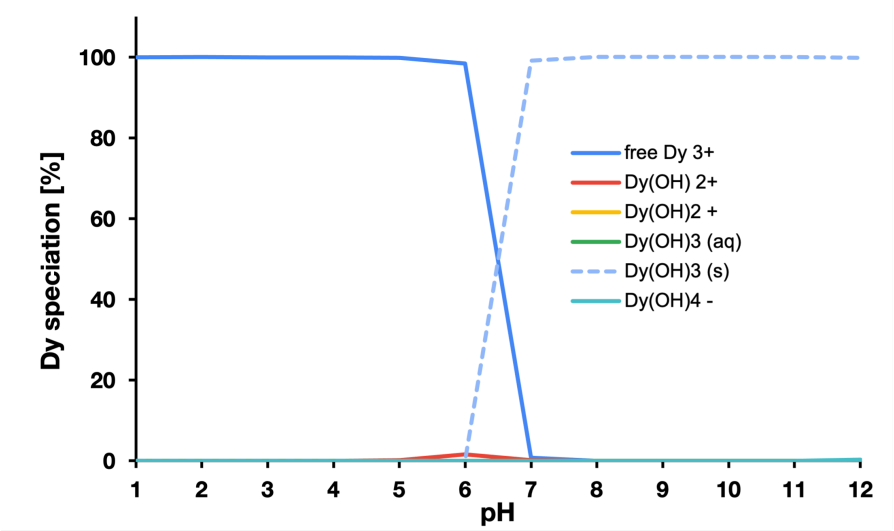

Figure 4.3: The speciation of Dy at chemical equilibrium as a function of different pH values. The Dy concentration was 2.0 mM, equal to 20 kBq of Dy-166 activity, the Cl^- concentration: 0.1 mM. The figure is based on plotted CHEAQS data points. For more details, see table B.10.

Figures 4.2 and 4.3 reveal little new information compared to figure 4.1. Below a pH of 6, free Dy^{3+}-ions are dominant. Between pH 6 and 7, there is a transition from free Dy^{3+} to $Dy(OH)_3$ (s). Above pH 7, $Dy(OH)_3$ (s) is the only present species.
More chemical speciation analysis was done for dysprosium. The speciation of Dy at pH 6-12 for concentrations ranging from $1{\cdot}10^{-10}$ to 1 M was determined. The tables containing the data can be found in Appendix B, section B.1.

The chemical speciation of Ho-166 was determined in the same way as for Dy/Dy-166 and can be found in appendix B, section B.2. As Ho-166 was formed only by the decay of Dy-166 and only 1% of the available dysprosium was active, the concentration of Ho-166 was overall low. The concentration Ho-166 during loading is estimated to be $7{\cdot}10^{-10}$ M maximum. The calculation of this estimate is given in Appendix A, section A.4. According to CHEAQS Next, in order of dominance, holmium forms free Ho^{3+}-ions, $Ho(OH)^{2+}$, $Ho(OH)_2^+$, $Ho(OH)_3$ (aq) and $Ho(OH)_4^-$ for pH 6, 7 and 8.

4.1.2. Different loading methods

To test the loading mechanism as described by Liu et al. [7], three different loading methods were tested. Two of those were 'extremes' of the proposed loading mechnism to investigate if isotopes actually had to be loaded as aqueous hydroxides to gain a high labelling efficiency and stability.

DLS and micelles

A PCL-PEO [2800-2000] micelle sample was measured to determine the micelles' hydrodynamic radius. The micelles in this project had a hydrodynamic radius of 20 nm (see Appendix A, figure A.1).

Loading Dy at low pH

The first extreme that was tested was loading Dy/Dy-166 as Dy^{3+}-ions. From the chemical speciation analysis, it was known that Dy existed mostly as Dy^{3+} at lower pH at the three experimentally used Dy concentrations (see figures 4.1), 4.2 and 4.3. To test if these free Dy^{3+}-ions could be loaded, 20 kBq Dy/Dy-166 was added to 0.5 mL PCL-PEO [2800-2000] micelles (pH around 3-4) without buffer solution. This gave a Dy concentration of 2 mM during loading. The mixture was stirred for 30 minutes, after which 0.5 mL HEPES buffer pH 7.5 20 mM was added. The HEPES increased the pH to 7.5. After stirring and SEC, all fractions were measured with the Wallac Gamma Counter. None of the fractions revealed to contain activity. This meant that the micelles were not labelled with Dy-166/Ho-166. The experiment was done in triplet and since no activity was measured, the labelling efficiency was 0+/-0%. Because no labelling took place, it was not necessary to perform stability studies.

Forming $Dy(OH)_3$ (s) and adding micelles later

The second extreme that was tested was loading Dy/Dy-166 in $Dy(OH)_3$ (s) form. According to the chemical speciation (see figures 4.1, 4.2 and 4.3), Dy/Dy-166 would form $Dy(OH)_3$ (s) at pH 7 and higher once in chemical equilibrium. Therefore, Dy/Dy-166 was allowed to first form $Dy(OH)_3$ (s) in 0.5 mL HEPES pH 7.5 20 mM solution before micelles were added. The concentration of Dy/Dy-166 was again 2 mM. The idea was that before adding micelles, Dy was given more time to make possibly larger precipitates outside the micelles. The Dy/Dy-166 and HEPES mixture was stirred for 30 minutes. After these 30 minutes, the solutions in the vials had become cloudy and less transparent. Then, 0.5 mL PCL-PEO [2800-2000] micelles was added and the mixture was stirred for an additional 30 minutes. After stirring and SEC were completed, all fractions were measured with the Wallac Gamma Counter. Here too, no activity was measured in any of the collected fractions. The experiment was done in triplet and the labelling efficiency was 0+/-0%.s

Loading Dy in the presence of micelles

The two 'extreme' experiments revealed that either loading free Dy^{3+} or $Dy(OH)_3$ (s) formed outside the micelles was not possible. The loading procedure as proposed by Liu et al. [7] was therefore tested. For this loading procedure, 0.5 mL buffer solution (pH 6.8-8) was first mixed with 0.5 mL PCL-PEO micelles solution. While this mixture was stirring, 20 kBq Dy/Dy-166 was added to get Dy concentrations of 0.2 mM, 0.7 mM or 2.0 mM during loading. This would allow Dy to form $Dy(OH)_3$ (s) in the presence of

micelles. The total loading time was 1 hour. Different pH values were tested to find the optimal loading conditions for Dy/Dy-166. Once the optimal loading conditions were found, Dy_2O_3 was used with higher activity to study the influence of loading loading times and the retention of the loading. The results of finding the optimal loading conditions can be found in the next section.

4.1.3. Optimal loading conditions

The optimal loading conditions were determined based on the chemical speciation results for Dy/Dy-166. Three different pH values were tested. pH 6.8, which falls in the beginning of the transition of free Dy^{3+} to $Dy(OH)_3$ (s). pH 7.5, where $Dy(OH)_3$ presence nears 100%. pH 8, with 100% expected $Dy(OH)_3$ (s). This data can be found in figures tables B.26, B.27, B.28, B.29 and B.3. The loading time was 1 hour and the labelled micelles typically came off the SEC columns between fraction 10-14. Figure A.2 is an example of counts measured per fractions to show when the labelled micelles came off the columns. For radiolabelling experiments, 20 fractions in total were collected. Unless stated otherwise, all experiments were carried out in triplets.

For three different pH values and three different dysprosium concentrations, the radiolabelling efficiency and the mass loading were determined. For every experiment, 20 kBq activity was needed. The maximum concentration of dysprosium was limited to 2 mM. Above 2 mM, the pH as stabilized by the buffer would fluctuate and not be maintained any more by the presence of Dy^{3+} and hydroxide complexes it formed.
The radiolabelling efficiencies for pH 6.8 were 1.47+/-0.4% ([Dy] = 0.2 mM), 1.27+/-0.4% ([Dy] = 0.7 mM) and 0.22+/-0.03% ([Dy] = 2.0 mM). For pH 7.5, the labelling efficiencies were 2.05+/-0.4% ([Dy] = 0.2 mM), 3.00+/-0.3% ([Dy] = 0.7 mM) and 0.41+/-0.2% ([Dy] = 2.0 mM). Lastly, for pH 8, the labelling efficiencies were 2.53+0.46% ([Dy] = 0.2 mM), 1.1+/-0.1% ([Dy] = 0.7 mM) and 0.71+/-0.02% ([Dy] = 2.0 mM). These results are displayed in figure 4.4 and summarized in table 4.1.

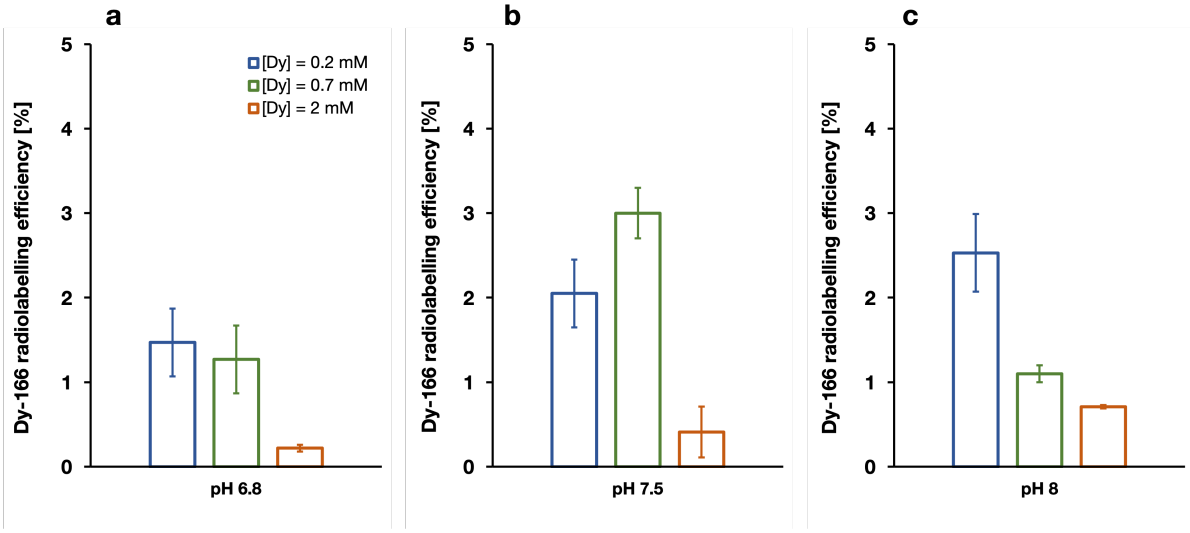

Figure 4.4: The radiolabelling efficiencies of PCL-PEO [2800-2000] micelles labelled with Dy/Dy-166 and Ho-166 for Dy concentrations 0.2 mM, 0.7 mM and 2.0 mM for pH values of (a) 6.8, (b) 7.5 and (c) 8.0 and 1 hour of loading. The polymer concentration was 4.4+/-0.15 mg/mL (before filtration) in the radiolabelling process. The error bars represent standard deviations with n = 3.

The radiolabelling efficiency is low, with a maximum of 3.00+/-0.3% for pH 7.5 and [Dy] = 0.7 mM. This means that from the initially added activity, little remains to study the retention of the loading. With the highest radiolabelling efficiency, only 0.6 kBq was actually loaded.

The radiolabelling efficiency reveals little useful information about the actual loading of the isotopes, as most Dy is not radioactive. Therefore, the calculation of the mass loading (in nmol) of Dy into the micelles allowed for a better comparison of the different loading conditions. The mass loading,

calculated as shown in section 3.10.2, was derived directly from the radiolabelling efficiency. The results are shown in figure 4.5.

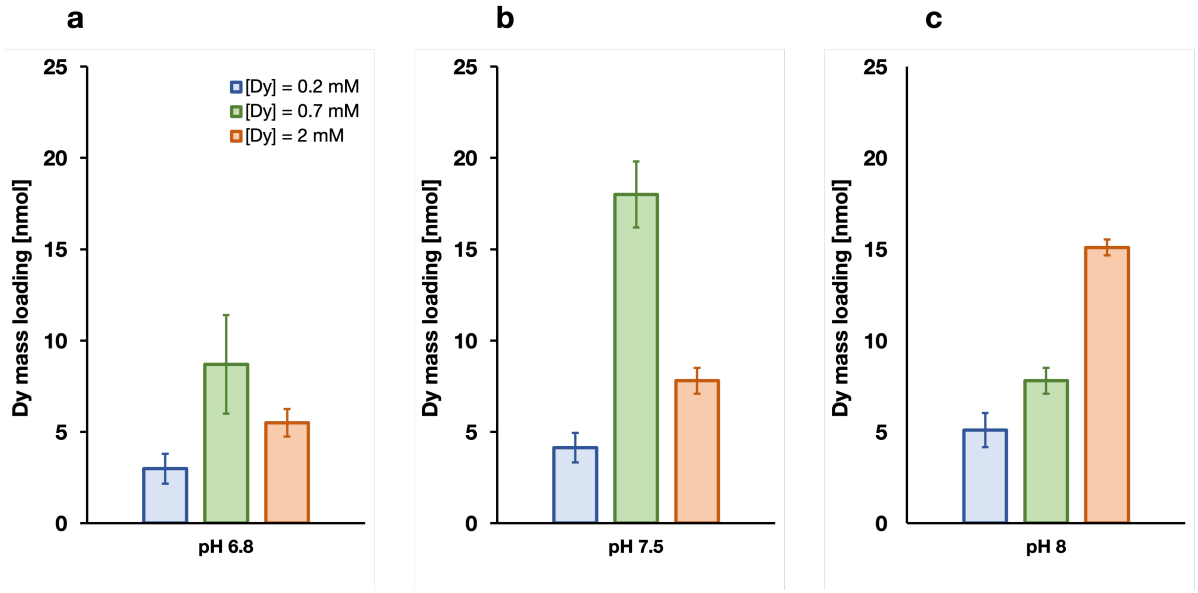

Figure 4.5: The mass loading of PCL-PEO [2800-2000] micelles labelled with Dy/Dy-166 and Ho-166 for Dy concentration 0.2 mM, 0.7 mM and 2.0 mM for pH values of (a) 6.8, (b) 7.5 and (c) 8.0 and 1 hour of loading. The polymer concentration was 4.4+/-0.15 mg/mL (before filtration) in the radiolabelling process. The error bars represent standard deviations with n = 3.

The lowest mass loading was achieved at the lowest concentration for pH 6.8. With a mass loading of 2.98+/-0.2 nmol, the mass loading was 1/6 of the maximum achieved loading. A concentration of 0.7 mM and a pH of 7.5 achieved a mass loading of 18+/-1.8 nmol. The labelling efficiencies of [Dy] = 0.7 mM at pH 7.5 was comparable to that of [Dy] = 0.2 mM at pH 8. However, the mass loading of [Dy] = 0.7 mM at pH 7.5 and [Dy] = 2.0 mM at pH 8 were closer: 18+/-1.8 nmol against 15.1+/-0.43 nmol, respectively.
From the chemical speciation, it was clear that the higher the pH, the more $Dy(OH)_3$ (s) was formed. In contrast, the mass loading of [Dy] = 0.7 mM at pH 7.5 is significantly higher than all other results. From these nine different loading conditions, it shows to be the most optimal.

Retention

The radiolabelling efficiency of the optimal loading condition experiment was low - a maximum value of 3.00+/-0.3% was reached. With the initially added activity of 20 kBq per sample, this meant that a maximum of 0.6 kBq activity remained after loading and SEC. The Wallac Gamma counter has an efficiency for Dy-166 and Ho-166 of 7.5-8% (see section 3.9.2). This meant that the error per measurement after loading increased significantly. Although carried out for every experiment, the labelled micelles and labelled DTPA-complex counts could not be distinguished from the background.

The data of the results for the optimal loading experiments are summarized in table 4.1.

Table 4.1: A summary of the Dy/Dy-166 loading results. All experiments were done in triplet. The loading time was 1 hour. The DTPA challenge was performed for 24 hours. Dy-166 was made with $Dy(NO_3)_3 \cdot H_2O$. [a] concentration of Dy in mM. [b] radiolabelling efficiency. [c] mass loading Dy in nmol. [d] mass loading Dy per polymer weight in nmol/mg. [e] retention of the loading in the micelles. [f] percentage of loading taken out of the micelles by DTPA.

	[Dy][a]	rad. eff.[b] (%)	m load.[c] (nmol)	m/p[d] (nmol/mg)	ret.[e] (%)	DTPA[f] (%)
	0.2	1.47+/-0.4	2.98+/-0.82	0.15	x	x
pH 6.8	0.7	1.27+/-0.4	8.7+/-2.7	0.43	x	x
	2.0	0.22+/-0.03	5.5+/-0.75	0.28	x	x
	0.2	2.05+/-0.4	4.14+/-0.81	0.21	x	x
pH 7.5	0.7	3.00+/-0.3	18+/-1.8	0.9	x	x
	2.0	0.41+/-0.2	7.8+/-0.71	0.45	x	x
	0.2	2.53+/-0.46	5.10+/-0.94	0.25	x	x
pH 8.0	0.7	1.1+/-0.1	7.8+/-0.71	0.38	x	x
	2.0	0.71+/-0.02	15.1+/-0.43	0.74	x	x

4.1.4. Influence of temperature

During the experimental phase, interesting findings were made that showed the influence of the temperature in the laboratory on the loading efficiency of dysprosium into PCL-PEO [2800-2000] micelles. At the start of the summer, in June and July 2023, it was 30° Celsius and higher outdoors for a period of a few weeks. Due to the lack of airconditiong, the temperature in the lab was significantly higher than during spring. The general finding was that the higher the temperature in the lab, the lower the labelling efficiency of Dy/Dy-166 into the micelles. Most likely, the fluctuating temperatures had an influence on the chemical speciation of Dy/Dy-166 and Ho-166. When airconditioning was installed and the temperature indoors back to ambient, the labelling efficiency for Dy/Dy-166 at [Dy] = 0.7 mM and pH 7.5 were found to be around 3% again.
As these findings were not the core focus of the study and found as outliers, the results were placed in Appendix A, section A.5. It should be noted that these results should solely be seen as support information.

4.1.5. Influence of loading time

From the optimal loading conditions found in the previous section, the influence of an increased loading time was tested. This was done because the chemical speciation analysis done in CHEAQS Next [53] assumed chemical equilibrium between the various present chemicals. A longer loading time might help the chemicals reaching chemical equilibrium.

For these experiments, Dy_2O_3 samples were irradiated to produce the Dy-166/Ho-166 generator. The increased activity achieved by irradiating Dy_2O_3 allowed for the study of longer loading times and a the retention of the loading.

Two different loading times were compared: 1 hour vs 18 hours (overnight). After stirring, the micelle mixture was passed through a SEC column and the radiolabelling efficiency was determined. The labelling efficiencies for 1 hour and 18 hours of loading are presented in figure figure 4.6 (a). The 1 hour loading gave a labelling efficiency of 3.0+/-0.3%. 18 hours of loading gave a labelling efficiency of 3.28+/-0.13%. These results fell within the standard deviation of each other. The mass loading, however, was slightly higher for 18 hours, see figure 4.6(b). The calculated mass loading for 1 hour loading time was 18+/-1.8 nmol and for 18 hours, it was 23.6+/-1.0 nmol. Although the labelling efficiences are comparable, the longer loading time gave a 31% increase in mass loading.

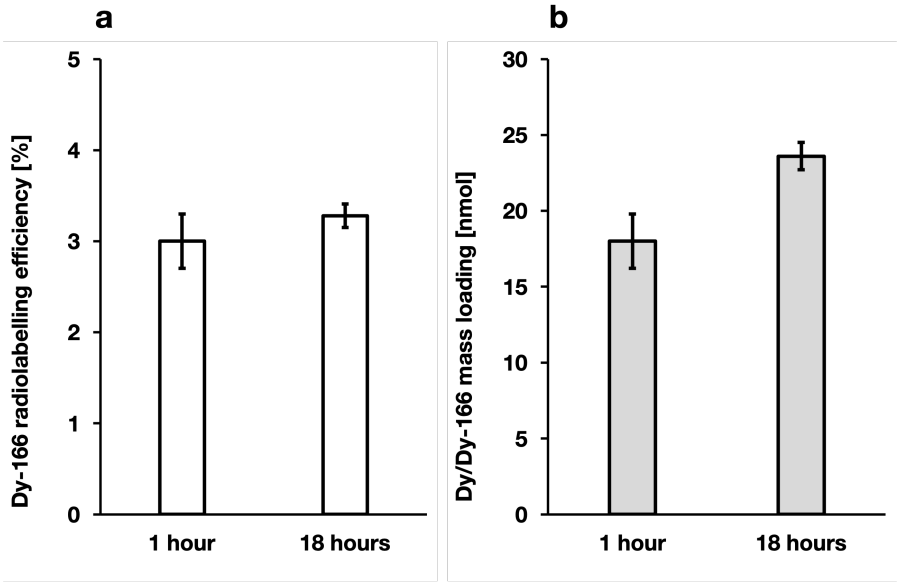

Figure 4.6: The (a) radiolabelling efficiencies and (b) mass loading of PCL-PEO [2800-2000] micelles labelled with Dy/Dy-166 and Ho-166 for [Dy] = 0.7 mM for 1 hour and 18 hours of loading. The polymer concentration was 4.4+/-0.15 mg/mL (before filtration) in the radiolabelling process. The error bars represent standard deviations with n = 3.

Retention

Previous experiments with 20 kBq did not allow for stability studies due to the low labelling efficiency and therefore low residual activity. With the use of the higher active Dy_2O_3 this problem was eliminated and the stability of the loading could be tested. This was done by challenging the loading with DTPA incubation for 2 hours, 4 hours and 24 hours. The PCL-PEO [2800-2000] micelles labelled with Dy/Dy-166 and Ho-166 from the 1 hour loading (3.0+/-0.3% labelling efficiency) versus the 18 hours loading (3.28+/-0.13% labelling efficiency) experiments were used.

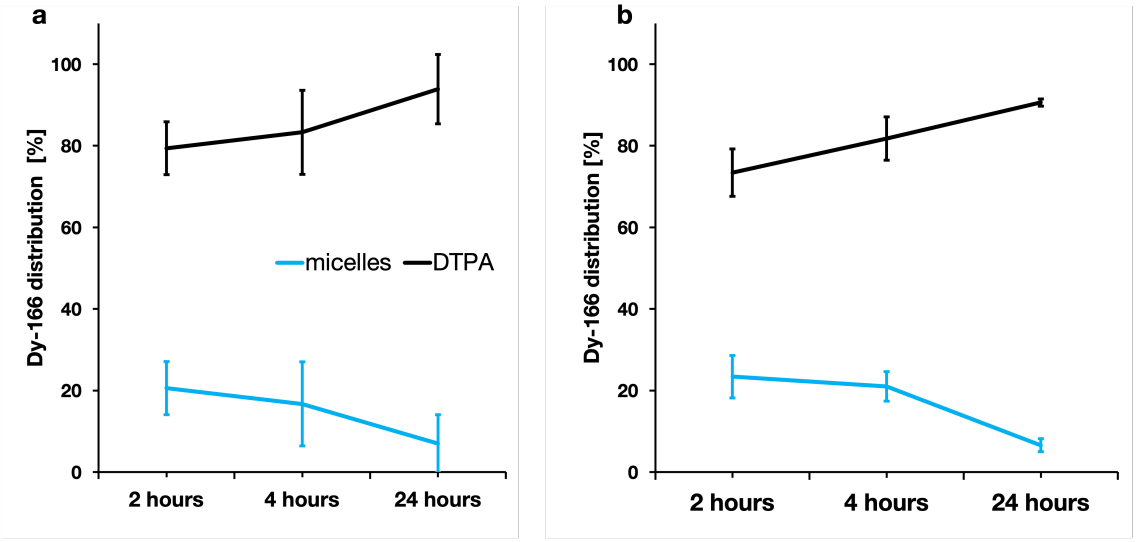

Figure 4.7: The results of stability tests performed with PCL-PEO [2800-2000] micelles labelled with Dy/Dy-166 and Ho-166 for (a) 1 hour loading and (b) 18 hour loading time. The Dy-166 distribution is shown after the labelled micelles were challenged with DTPA for 2 hours, 4 hours and 24 hours. The error bars represent standard deviations with n = 2 for (a) 2 hours and 4 hours and n = 3 for (a) 24 hours and all results in (b).

There was good separation during SEC between the labelled micelles and the labelled DTPA complexes, as shown by distinction between the first and second peak in figure A.3. The DTPA complexes were typically collected between fractions 16-20. The results are shown in figure 4.7, in which (a) shows the retention after 1 hour of loading and different DTPA incubation times and (b) the same for 18 hours of loading. The results of the stability tests of the 1 hour loaded and 18 hours loaded micelles show to be highly comparable. The longer the DTPA incubation time, the more of the loading was taken out of the micelles. There is no 'plateau' behavior visible for these incubation times. For both 1 hour and 18 hour loaded micelles, almost 80% of the Dy/Dy-166 and Ho-166 was taken out by DTPA after 2 hours incubation already. Due to the large standard deviations in figure 4.7a in figure 4.7b, the results show overlap. The trends in both figures are similar. This means that a longer loading time does not increase the stability of the loading. It means that within the 1 hour loading, chemical equilibrium is already reached and no additional Dy/Dy-166 is retained inside the micelles.

Tables 4.2 and 4.3 summarize the results for 1 hour vs 18 hours loading including the DTPA challenge data. Note that the radiolabelling efficiency and mass loading for the 1 hour experiments is substantially lower than expected. These experiments were performed during a period the temperatures in the lab sometimes exceeded 30 degrees Celsius.

Table 4.2: A summary of the 1 hour dysprosium loading results under optimal conditions ([Dy] = 0.7 mM, pH 7.5) with Dy-166 produced with Dy_2O_3. [a] concentration of Dy in mM. [b] radiolabelling efficiency as percentage. [c] mass loading Dy in nmol. [d] mass loading Dy per polymer weight in nmol/mg. [e] duration of the DTPA challenge. [f] retention of the loading in the micelles as percentage. [g] percentage of loading taken out of the micelles by DTPA. *The temperatures in the lab were close to 30 degrees Celsius, the expected reason for the lower radiolabelling efficiency. **Done in duplo due to stirring rod shortage.

	[Dy][a]	rad. eff.[b] (%)	m load.[c]	m/p[d]	DTPA[e] (hr)	ret.[f] (%)	DTPA[g] (%)
pH 7.5	0.7	1.16+/-0.18*	8.35+/-1.27	0.42	2	20.6+/-6.5**	79.4+/-6.5
pH 7.5	0.7	1.16+/-0.18*	8.35+/-1.27	0.42	4	16.7+/-10.3**	83.3+/-10.3
pH 7.5	0.7	1.16+/-0.18*	8.35+/-1.27	0.42	24	7.0+/-7.1	93.9+/-8.5

Table 4.3: A summary of the 18 hour dysprosium loading results under optimal conditions ([Dy] = 0.7 mM, pH 7.5) with Dy-166 produced with Dy_2O_3. [a] concentration of Dy in mM. [b] radiolabelling efficiency as percentage. [c] mass loading Dy in nmol. [d] mass loading Dy per polymer weight in nmol/mg. [e] duration of the DTPA challenge. [f] retention of the loading in the micelles as percentage. [g] percentage of loading taken out of the micelles by DTPA. *Done in duplo due to clogging of the SEC columns.

	[Dy][a]	rad. eff.[b] (%)	m load.[c]	m/p[d]	DTPA[e] (hr)	ret.[f] (%)	DTPA[g] (%)
pH 7.5	0.7	2.77+/-0.29*	19.9+/-2.1	0.97	2	23.4+/-5.2	73.4+/-5.8
pH 7.5	0.7	3.28+/-0.13	23.6+/-1.0	1.17	4	21.0+/-3.6	81.8+/-5.3
pH 7.5	0.7	3.28+/-0.13	23.6+/-1.0	1.17	24	6.6+/-1.6	90.6+/-0.9

4.1.6. Retention of Dy-166 versus Ho-166

To distinguish the loading of Dy/Dy-166 and Ho-166, the high sensitive Zn-window Ge detector was used. The Zn-window Ge detector was able to make a distinction between gammas there were emitted by Dy-166 and Ho-166 (82.5 keV and 80.6 keV respectively). The energies of the gammas differ only 1.9 keV. This difference was too little for the Wallac Gamma counter and the regular Ge detector to measure the gamma separately. As will become clear, the Zn-window Ge detector was able to make a perfect distinction between the two energies.
For these experiments, the loading ratio between Dy-166 and Ho-166 was determined from the quantitative information provided by the Ge detector. To make a prediction about the ratio Dy-166/Ho-166, the Bateman equation as described in section 2.2.1 were solved from the initial activity of a Dy_2O_3 irradiated sample. The typical starting activity of Dy-166 directly after irradiation and before cooling was around 30 MBq. The development of the activity was calculated over the course of 800 hours,

starting at t = 0 directly after irradiation. The assumption here is that Ho-166 only starts forming once the irradiation is finished. The time of maximum activity of Ho-166, as confirmed by equation 2.9, was around 80 hours, hence roughly 4 times the half-life of Ho-166.
Once in equilibrium, the ratio daughter activity/parent activity is 1.49. This means that the activity of Ho-166 is 1.49 times higher than that of Dy-166 once in equilibrium. This is shown in figure 4.8. The figure shows the contribution og Ho-166 and Dy-166 to the total activity of the Dy-166/Ho-166 generator. Dy-166 is responsible for around 40% of the total activity, while Ho-166 contributes 60%.

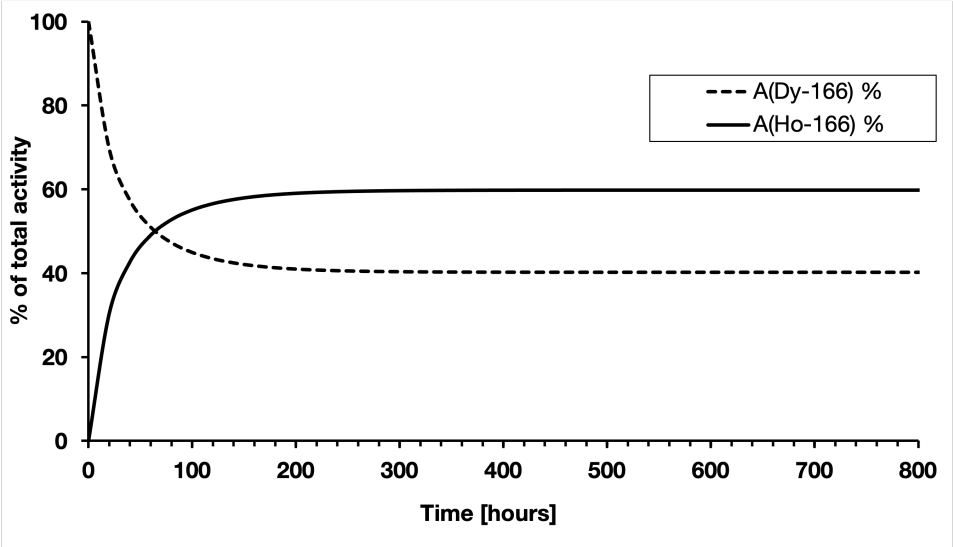

Figure 4.8: The contribution to the total activity by Dy-166 and Ho-166 for a start activity of Dy-166 of 30 MBq. After 360 hours, the activity ratio between Ho-166 and Dy-166 is stable at 1.49.

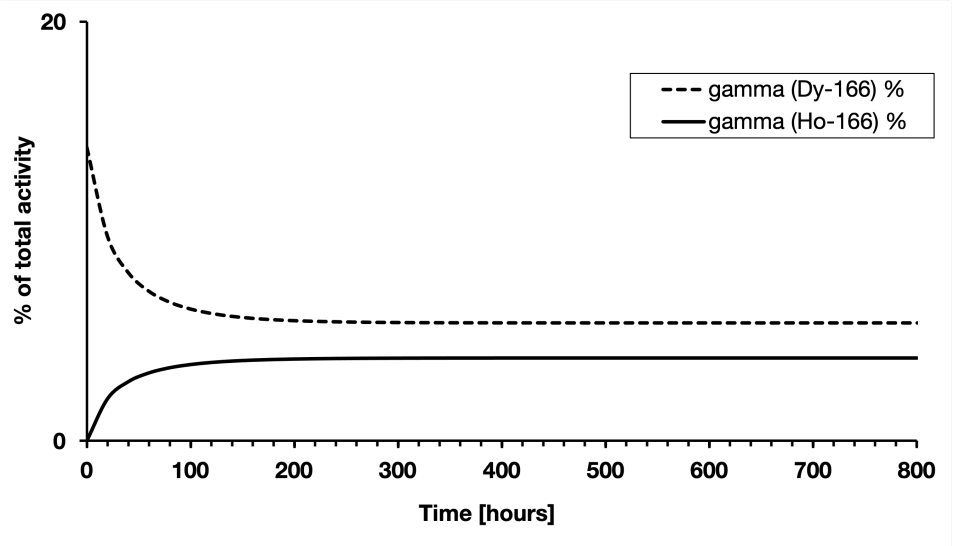

Figure 4.9: Percentage of total activity by the gammas emitted by Dy-166 (14% gamma yield) and Ho-166 (6.6% gamma yield) for a start activity of Dy-166 of 30 MBq. The expected contribution of the Dy-166 gammas to the total activity if 5.6% and for the Ho-166 gammas it is 3.96%.

The Zn-window Ge detector is only able to measure the gammas emitted by Dy-166 and Ho-166 decay. Although the ratio of Ho-166/Dy-166 for the total activity is expected to be 1.49, the ratio of their respective gammas is expected to be different. The 80.6 keV gamma emitted by Ho-166 has a 6.7% yield and the 82.5 keV gamma from Dy-166 has a 14% yield. That means that the 80.6 keV Ho-166

gamma contributes for 3.96% to the total activity and the 82.5 keV Dy-166 gamma for 5.6% to the total activity at equilibrium. This is shown in figure 4.9.

With the predicted values for the activities and ratios for the Dy-166/Ho-166 generator in equilibrium, the actual ratio found in labelled micelles was determined. This was done for PCL-PEO [2800-2000] micelles loaded for 18 hours with 315 kBq Dy-166 activity. The labelling efficiency was 3.28+/-0.13%. This high activity ensured that there were enough counts after labelling for the Zn-window to sufficiently measure the gammas emitted by Dy-166 and Ho-166.

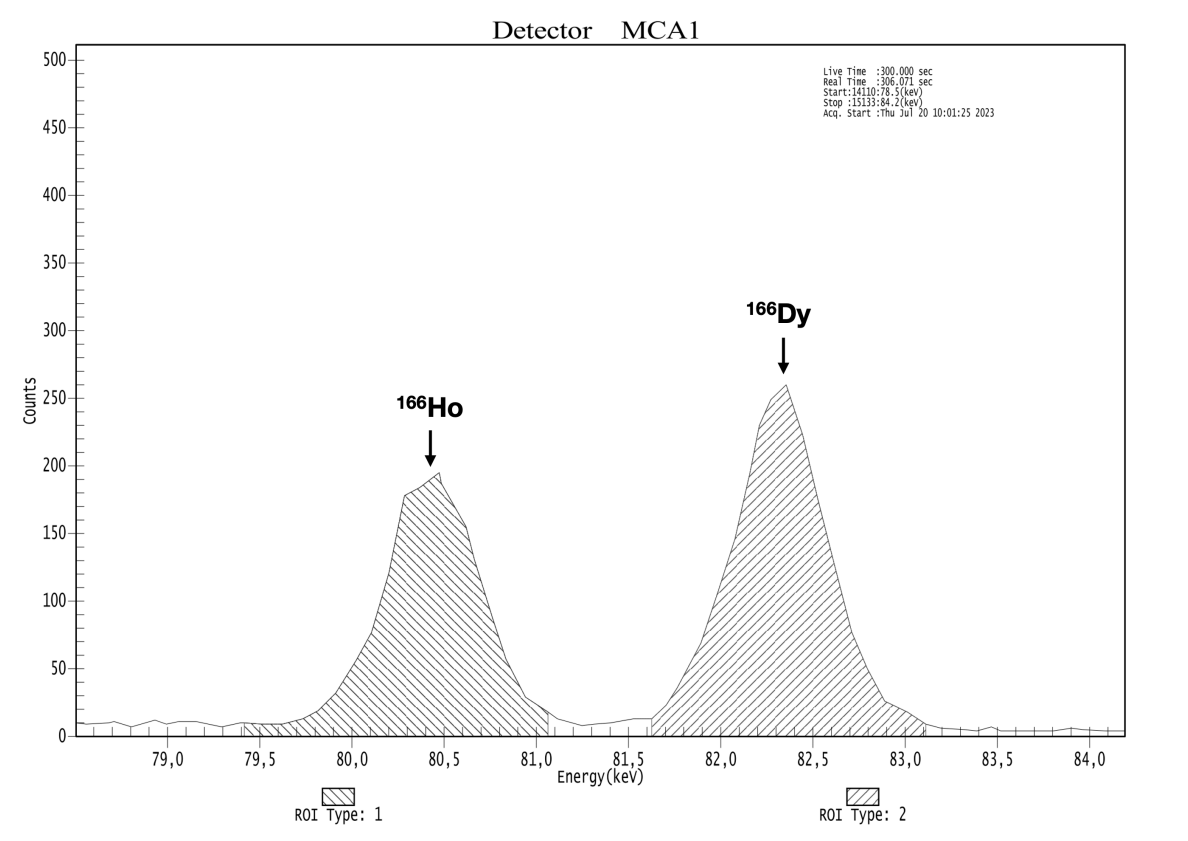

Figure 4.10: A gamma measurement of Dy-166 and Ho-166 encapsulated in PCL-PEO [2800-2000] micelles done with the high sensitive Zn-window Ge detector for 5 minutes. The labelled micelles were used from the 18 hours loading time experiment and had a radiolabelling efficiency of 3.28+/-0.13%. ROI stands for Region of Interest. ROI Ho-166: 79.5-81.5 keV. ROI Dy-166: 81.7-83.2 keV. An enlarged version can be found in appendix A, figure A.7.

Figure 4.10 shows an example of a direct measurement of Dy-166/Ho-166 labelled micelles with the Zn-window Ge detector. The region of interest (ROI) for Ho-166 was set at 79.5-81.5 keV and for Dy-166 at 81.6-83.2 keV. The counts shown are the total counts for 5 minute measurements. As can be seen, there was good separation between the two gamma energies and a distinction could be made between them. Another interesting finding was that the amount of counts for Ho-166 are similar to the expected ratio of Ho-166/Dy-166 gammas. The expected gamma ratio Ho-166/Dy-166 is 0.7. And, from the figure, this seems in line with the measured values.
This was further confirmed by the gamma measurement of labelled micelles that were loaded for 18 hours. The counts can be found in table 4.4. It shows there was relatively more Dy-166 to be found inside the micelles than Ho-166.

Table 4.4: Amount of counts measured in 5 min on the high-res Ge detector for samples containing Dy-166 and Ho-166 labelled PCL-PEO [2800-2000] micelles.

	Ho-166 counts	error (%)	Dy-166 counts	error (%)
sample 1	19249	1.05	25545	0.78
sample 2	18109	1.07	24612	0.79
sample 3	18134	1.06	24302	0.85
average	18497		24820	

After loading and these gamma measurements with the Zn-window Ge detector, DTPA incubation of the labelled micelles was done for 4 h and 24 h. Separation of the labelled micelles and the DTPA complexes was done with SEC. The goal was to determine if there was a difference between the ratio of Ho-166/Dy-166 inside the micelles and the ratio of Ho-166/Dy-166 attached to the DTPA complexes compared to the expected theoretical ratio.

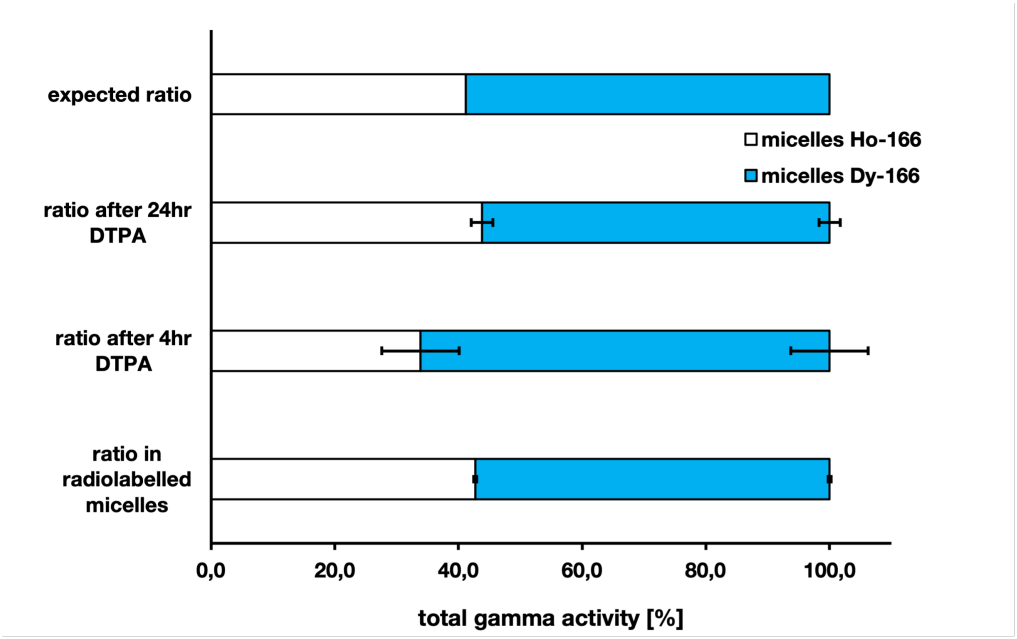

Figure 4.11: The ratio of Dy-166 and Ho-166 in labelled PCL-PEO micelles and micelles after a satbility test with DTPA. The top bar shows the expected % ratio of Ho-166 and Dy-166 (see also figure 4.8. The bottom three bars shows the ratio of the isotopes in loaded micelles: after loading, after 4 hour DTPA challenge, after 24 hour DTPA challenge. The error bars represent standard deviations with n = 3.

Figure 4.11 shows the expected percentage of the total activity compared to the measured counts with the Zn-window Ge detector. On the bottom of the figure, it was measured that the labelled micelles contained more Dy-166 than Ho-166. Then, with a 4 hour DTPA challenge, there seemed to be slightly more Ho-166 being taken out of the micelles than Dy-166. However, with the standard deviation included, this result was comparable to the % of total counts labelled micelles. The 24 hour DTPA reveals little new information. The same ratio Ho-166 and Dy-166 remains. Overall, this means that a similar amount of Ho-166 is loaded into the micelles as expected and both Ho-166 and Dy/Dy-166 have the same stability once loaded.

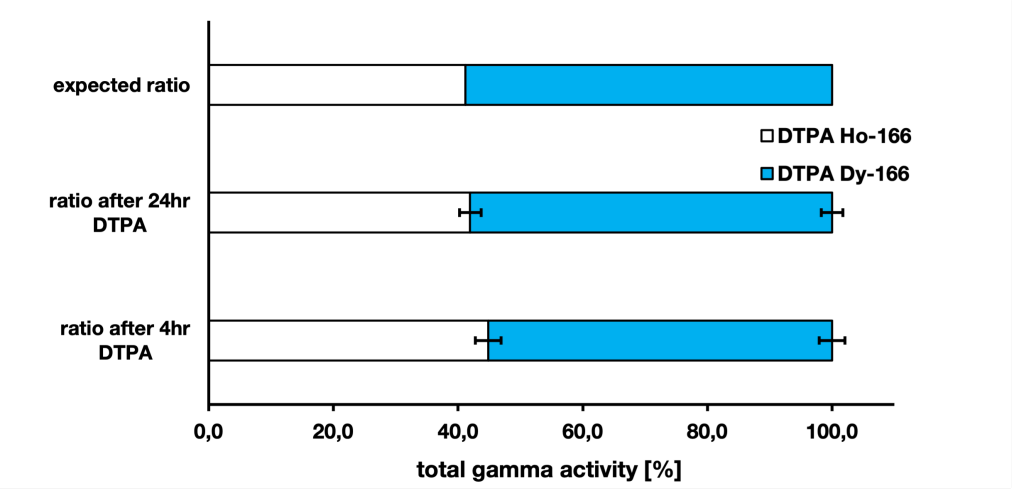

Figure 4.12: The ratio of Dy-166 and Ho-166 attached to DTPA after a a stability test with DTPA. The top bar shows the expected % ratio of Ho-166 and Dy-166. The bottom two bars show the ratio of the isotopes attached to the DTPA complex: 4 hour DTPA challenge and 24 hour DTPA challenge. The error bars represent standard deviations with n = 3.

Likewise, the ratio of Ho-166 and Dy-166 was measured in the samples containing DTPA. Figure 4.12 reveals similar results as the labelled micelles in figure 4.11. The overall abundance of Dy-166 and Ho-166 is similar to the expected value: 41-44% of the gammas were from Ho-166 and 56-59% from Dy-166.

4.1.7. Loading and retention of holmium

The mass loading and concentration of holmium during and after the loading procedure is estimated from the Bateman equations. With a radiolabelling efficiency of 3.0+/-0.3%, the mass loading and concentration of holmium are estimated in Appendix A, section A.4. The results are placed in an Appendix to provide extra insightful information about the loading procedure, but it should be seen as a rough estimate.

4.2. Ga-68 with PEO-b-PCL micelles

4.2.1. Chemical speciation

The chemical speciation for Ga/Ga-68 was determined with CHEAQS Next [53]. The tables containing the chemical speciation data can be found in Appendix B. The experiments were organized according to the chemical speciation predictions, of which the most important findings are discussed here.

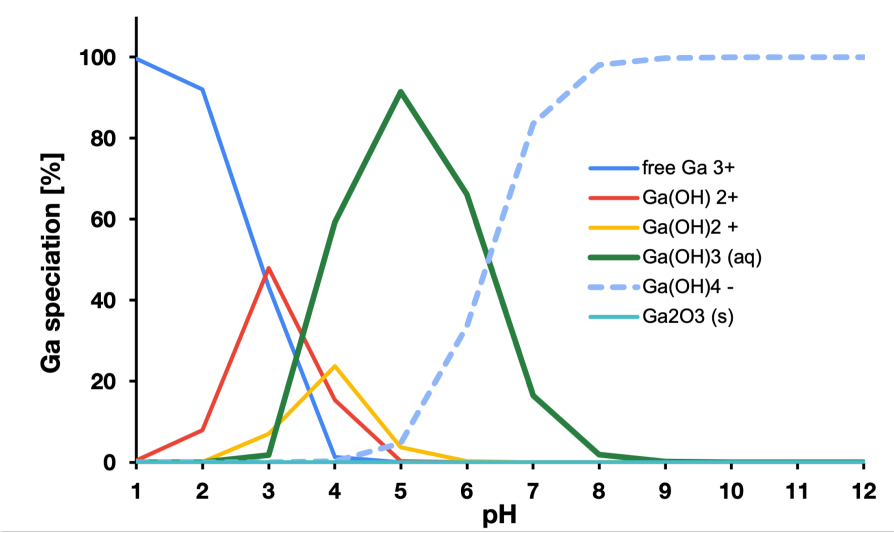

Figure 4.13: The speciation of Ga-68 at equilibrium as a function of different pH values. The Ga-68 concentration was based on using 80 kBq, calculated to be around $3.8{\cdot}10^{-13}$ M (see Appendix A, section A.7), the Cl^- concentration: 0.1 mM. The figure is based on plotted CHEAQS data points. For more details, see table B.32.

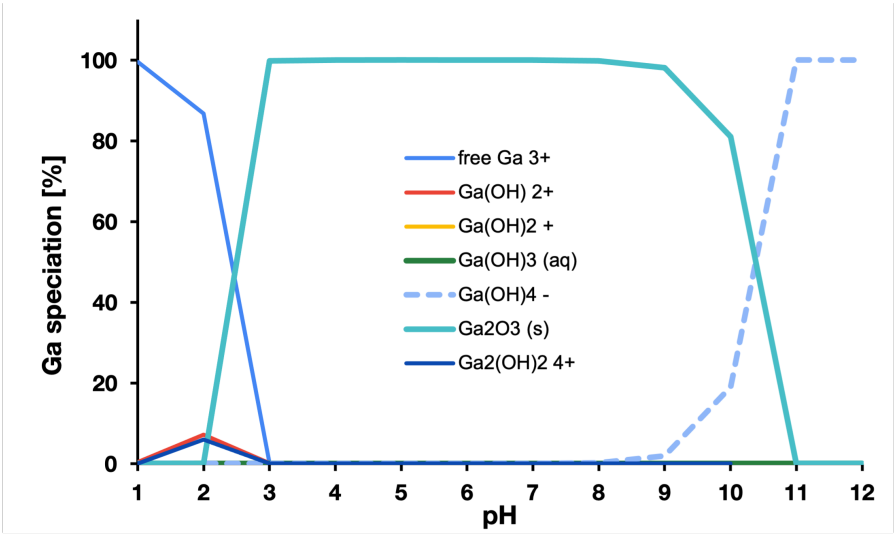

Figure 4.14: The speciation of Ga at equilibrium as a function of different pH values. The Ga concentration was 0.2136 mM, the Cl^- concentration: 0.1 mM. The figure is based on plotted CHEAQS data points. For more details, see table B.33.

Ga-68 was produced with a Ge-68/Ga-68 generator. The first experiments with Ga-68 were performed by adding 80 Bq Ga-68 to a buffer/micelle solution. The concentration of Ga-68 was low and estimated to be $3.8{\cdot}10^{-13}$ M (the calculation of the concentration estimation is shown in Appendix A, section A.7). Figure 4.13 shows the chemical speciation of Ga-68 at this low concentration at varying pH values. As can be seen in the graph, depending on the pH, Ga-68 exists in six different forms. Ga^{3+} is dominant between pH 1-3. From pH 3 $Ga(OH)_3$ (aq) emerges and is most abundant between pH 4 and 6.

From pH 5 $Ga(OH)_4^-$ is formed, which takes over as being the most dominant from pH 7 and higher. The formation of $Ga(OH)_3$ (aq) is promising to test the loading mechanism as proposed by Liu et al. [7].

The advantage of using Ga-68 from the Ge-68/Ga-68 generator was that non-active Ga could be added to increase the Ga concentration. The concentration Ga for higher concentration experiments was 0.2136 mM. The chemical speciation of [Ga] = 0.2136 mM at varying pH values is displayed in figure 4.14. The dominant species between pH 3-10 is Ga_2O_3 (s). At pH 11 and higher, a new species of Ga that was not formed at low Ga concentrations becomes dominant: $Ga_2(OH)_2^{4+}$.

The chemical speciation of Ga was done for various concentrations at different pH values as well. The data of CHEAQS speciation analysis for Ga/Ga-68 can be found in Appendix B, section B.4.

4.2.2. Low vs. high concentration

This section discusses the loading efficiency and mass loading of gallium in PCL-PEO [2800-2000] micelles under three different pH values: 5.5, 6.5 and 7.5. At these values, the existence of $Ga(OH)_3$ (aq) varies greatly. The low gallium concentration is estimated from activity measurements from the stock Ga-68 obtained from the Ge/Ga-generator. The calculation can be found in A, section A.7.

Low Ga concentration

The low concentration experiments were done at one Ga-68 concentration ($\approx 3.8{\cdot}10^{-13}$ M) during loading. 50 μL Ga-68 was added to 0.5 mL buffer solution and 0.5 mL PCL-PEO [2800-2000] micelles. Loading was done for one hour at pH 5.5, 6.5 and 7.5. The labelling efficienes were 36.0+/-1.0%, 25.3+/-3.3% and 33.8+1.8% respectively. The results are shown in figure 4.15 and summarized in table 4.5. For pH 5.5 and 6.5, MES buffer was used as it buffers well for a pH range of 5.5-6.7. HEPES buffer, like for the Dy experiments, was used for the pH 7.5 experiment.

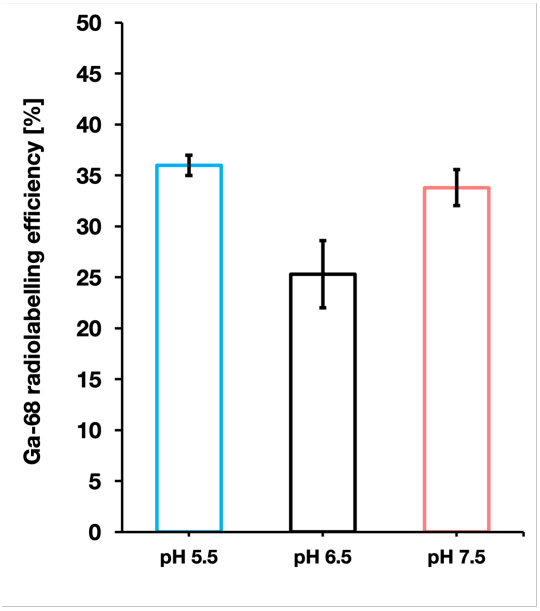

Figure 4.15: The radiolabelling of PCL-PEO [2800-2000] micelles labelled with 80 kBq Ga-68 for pH 5.5, 6.5 and 7.5 and 1 hour of loading. The polymer concentration was 4.4+/-0.15 mg/mL (before filtration) in the radiolabelling process. The error bars represent standard deviations with n = 3.

The mass loading of Ga-68 inside the micelles was calculated from the estimated initial Ga-68 concentration and the radiolabelling efficiency. The results can be found in figure 4.16. As Ga-68 decays fast, the mass loading is shown purely as supportive information. With the low concentration of Ga-68 during loading, the mass loading was calculated to be of the order of fmol.

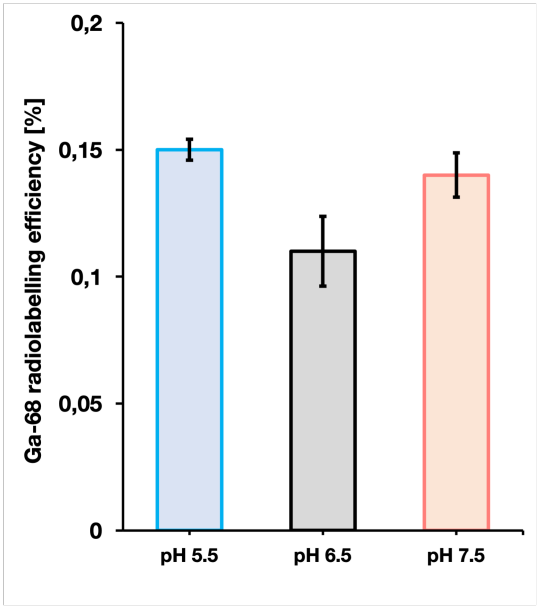

Figure 4.16: The mass loading of PCL-PEO [2800-2000] micelles labelled with 80 kBq Ga-68 for pH 5.5, 6.5 and 7.5 and 1 hour of loading. The polymer concentration was 4.4+/-0.15 mg/mL (before filtration) in the radiolabelling process. The error bars represent standard deviations with n = 3.

DTPA challenge experiments were done to gain insight into the retention of Ga-68. The DTPA incubation time was 1 hour per sample and there were significant differences between the retention at the three different pH values.

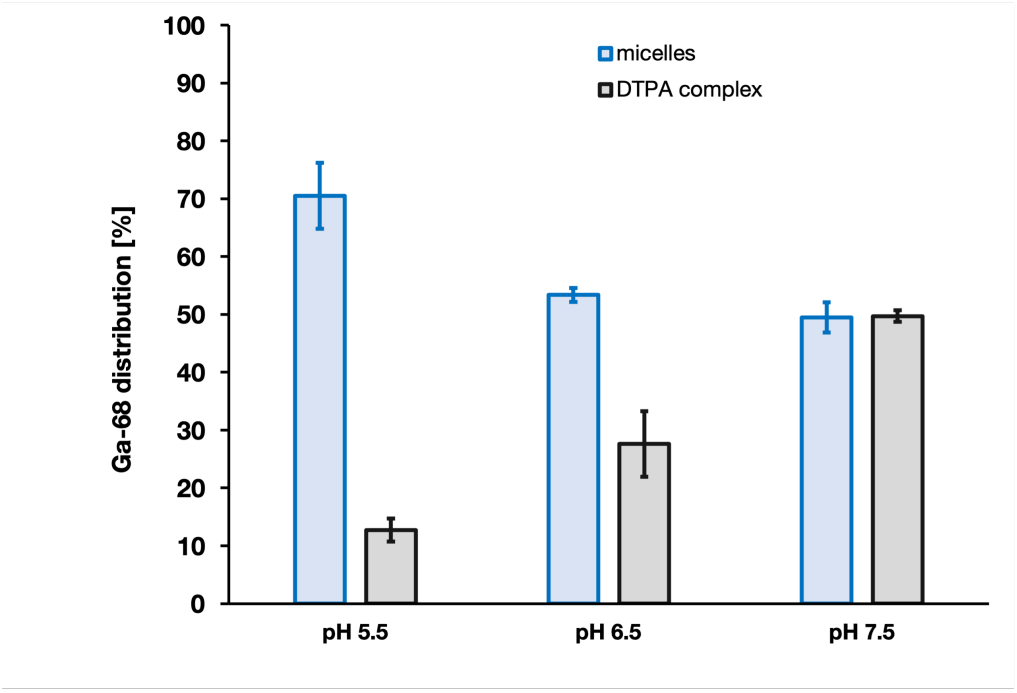

Figure 4.17: The results of stability tests performed with PCL-PEO [2800-2000] miceles labelled with 80 kBq Ga-68. The Ga-68 distribution is shown after the labelled micelles were challenged with DTPA for 1 hour. The error bars represent standard deviations with n = 3.

Figure 4.17 displays the retention of Ga-68 in the micelles when using a low Ga concentration of the loading process at pH values of 5.5, 6.5 and 7.5. Noticeable is the difference in retention between the

different pH values. When adding up the retention (blue) and DTPA (black) bars in figure 4.17, the total % of pH 5.5 and 6.5 is not equal to 100%. At pH 7.5, all Ga-68 present before SEC came off the columns after SEC. This means that pH 5.5 and 6.5, part of the Ga-68/DTPA complexes or Ga-68 isotopes were taken out the micelles and got left behind in the Sephadex G-25 resin in the columns.

Furthermore, the retention at pH 5.5 is the highest: 70.5+5.7% with DTPA at 12.7+/-2.0%. At pH 6.5 and 7.5, it is clear that the retention decreases: 53.4+/-1.2% (pH 6.5) and 49.5+/-2.6% (pH 7.5). This is partly in line with the chemical speciation shown in figure 4.13. Between pH 4 and 6, the $Ga(OH)_3$ (aq) species is predicted to be dominant. At pH 6.5, the $Ga(OH)_3$ (aq) presence is 66.10% and at pH 7.5, it is 5.85% (see tables B.25, B.27 and B.29 for the data).
The highest retention at pH 5.5 might be explained by the dominant presence of $Ga(OH)_3$ (aq) at that pH value. As proposed by Liu et al. [7], a high stability of the loading is achieved when the loading in the core is able to form solid precipitates. From the chemical speciation as shown in figure 4.14, it became clear that Ga_2O_3 (s) is formed when the Ga concentration is high enough. Hence, the most likely explanation for the high retention at pH 5.5 is that inside the core, Ga was able to form Ga_2O_3 (s). It hints strongly that the proposed mechanism by Liu et al. [7] works at least for Ga.

To test the mechanism further, Ga was loaded into micelles at high concentration (0.2136 mM). This was done by adding non-active Ga to the Ga-68 stock extracted from the Ge-68/Ga-68 generator. Figure 4.14 revealed that at this higher concentration of Ga, the dominant species would be Ga_2O_3 (s) between pH 3 and 10. The loading of Ga_2O_3 (s) would make a great comparison to the loading of $Dy(OH)_3$ (s) as done in the previous sections.

High Ga concentration

The concentration of gallium during the high concentration experiments was done at [Ga] = 0.2136 mM. This was achieved by adding 50 μL of 4.7 mM non-active Ga solution to the micelles, buffer and 50 μL Ga-68 (80 kBq) mixture. This was then stirred for 1 hour, giving the labelling efficiencies found in figure 4.18.

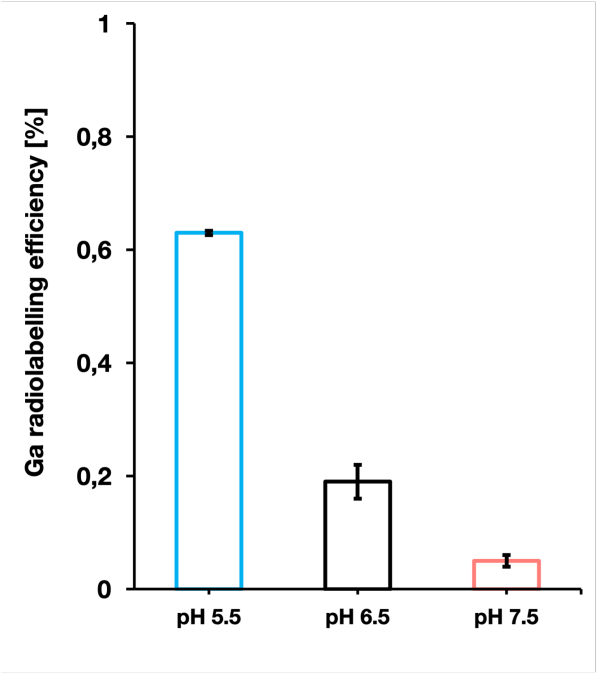

Figure 4.18: The radiolabelling of PCL-PEO [2800-2000] micelles labelled with Ga/Ga-68 for pH 5.5, 6.5 and 7.5 and 1 hour of loading. The Ga concentration was 0.1236 mM. The polymer concentration was 4.4+/-0.15 mg/mL (before filtration) in the radiolabelling process. The error bars represent standard deviations with n = 3.

The labelling efficiencies were 0.63+/-0.1% (pH 5.5), 0.19+/-0.03% (pH 6.5) and 0.05+/-0.01 (pH 7.5).

This is substantially lower than was achieved for low concentrations. These labelling efficiencies revealed the increased difficulty of loading a solid molecule like Ga_2O_3 (s) compared to $Ga(OH)_3$ (aq) and $Ga(OH)_4^-$. The low labelling efficiencies prevented DTPA challenges from being performed - of the total 80 kBq added activity, only a small fraction remained after loading. Together with the half-life of Ga-68, the stability tests with DTPA revealed to be fruitless.

Since the concentration of added gallium was much higher than in the previous section, the mass loading was expected to be significantly higher than for lower concentrations. This is because the bulk of gallium added is 10 billion times higher than for the lower concentration experiments. The mass loading of Ga/Ga-68 can be found in figure 4.19.

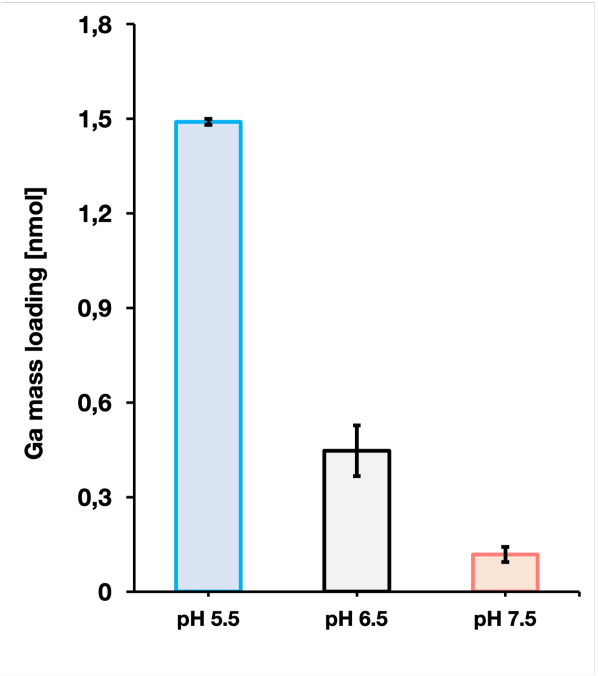

Figure 4.19: The mass loading of PCL-PEO [2800-2000] micelles labelled with Ga/Ga-68 for pH 5.5, 6.5 and 7.5 and 1 hour of loading. The Ga concentration was 0.1236 mM. The polymer concentration was 4.4+/-0.15 mg/mL (before filtration) in the radiolabelling process. The error bars represent standard deviations with n = 3.

The mass loading for pH 5.5 was overall the highest: 1.48+/-0.01 nmol gallium was loaded inside the micelles. For pH 6.5 and 7.5, the mass loadings were 0.45+/-0.08 nmol and 0.12+/-0.02 nmol respectively.

The data of the Ga/Ga-68 loading experiments can be found in table 4.5 and 4.6.

4.2.3. Summary of the results

This section contains a summary of the data for the experiments with Ga/Ga-68 loaded into PCL-PEO [2800-2000] micelles. Table 4.5 contains the data of the low concentration Ga-68 experiments. Table 4.6 contains the data of the high concentration Ga experiments.

Table 4.5: Summary of the gallium low concentration loading results. All experiments were done in triplet. The loading time was one hour. The DTPA challenge was performed for 1 hour. Ga-68 was produced by the Ge-68/Ga-68 generator. [a] concentration of gallium in M. [b] radiolabelling efficiency as percentage from originally added activity. [c] mass loading gallium in fmol. [d] DTPA challenge duration in hr. [e] retention of the loading in the micelles as percentage. [f] percentage of loading taken out of the micelles by DTPA.

	[Ga][a]	rad. eff.[b] (%)	mass loading[c] (fmol)	DTPA[d] (hr)	ret.[e] (%)	DTPA[f] (%)
pH 5.5	3.8E-13	36.0+/-1.0	0.15+/-0.004	1	70.5+/-5.7	12.7+/-2.0
pH 6.5	3.8E-13	25.3+/-3.3	0.11+/-0.01	1	53.4+/-1.2	27.6+/-5.7
pH 7.5	3.8E-13	33.8+/-1.8	0.14+/-0.01	1	49.5+/-2.6	49.7+/-1.0

Table 4.6: Summary of the [Ga] = 0.2136 mM loading results. All experiments were done in triplet. The loading time was one hour. The DTPA challenge was not performed. Ga-68 was produced by the Ge-68/Ga-68 generator. [a] concentration of gallium in mM. [b] radiolabelling efficiency as percentage from originally added activity. [c] mass loading gallium in nmol. [d] mass loading gallium per polymer weight in nmol/mg. [e] retention of the loading in the micelles as percentage. [f] percentage of loading taken out of the micelles by DTPA.

	[Ga][a]	rad. eff.[b] (%)	mass loading[c]	m/p[d]	ret.[e] (%)	DTPA[f] (%)
pH 5.5	0.2136	0.63+/-0.01	1.48+/-0.03	0.33	x	x
pH 6.5	0.2136	0.19+/-0.03	0.45+/-0.08	0.042	x	x
pH 7.5	0.2136	0.05+/-0.01	0.12+/-0.02	0.011	x	x

5 Discussion

This section contains a discussion and comparison of the results gained throughout the course of this project.

The goal of this project was to investigate the interaction mechanism as proposed by Liu et al. [7] for metallic species and study it for Dy and Ho to be applied as an Dy-166/Ho-166 generator and PCL-PEO micelles [2800-2000]. The results gained by Liu et al. [7] are first discussed in order to compare the results found for loading Dy/Dy-166 (and Ho-166).
In the study by Liu et al. [7], PCL-PEO micelles of varying molecular weight were radiolabelled with Indium-111 (In-111), Lutetium-177 (Lu-177) and Zirconium-89 (Zr-89), with the main focus on In-111. The concentration of In-111 was $2.88 \cdot 10^{-11}$ M during loading experiments. As found from the chemical speciation analysis, In-111 was predicted to be in $In(OH)_3$ (aq) form. The radiolabelling efficiency and stability of In-111 were found to be 80% for PCL-PEO [2800-2000] micelles. Other isotopes like Lu-177 and Zr-89 were explored to determine the interaction mechanism of the isotopes with the micelles. These other isotopes were loaded as aqueous hydroxides as well ($Lu(OH)_3$ (aq) and $Zr(OH)_4$ (aq)) with comparable labelling efficiencies and stabilities after the addition of phosphate ions. From these results, the interaction mechanism based on the loading of aqueous hydroxides was proposed.

Although promising for In-111, the question remained whether the proposed interaction mechanism worked for other isotopes as well. The Dy-166/Ho-166 generator was the subject of this thesis, since the use of the generator could potentially increase the effective dose given to tumour tissue by Ho-166. Next to that, micelles might form a solution to the internal conversion effects on the treatment efficiency with Ho-166.
To test the theory found by Liu et al. [7], the loading of Dy/Dy-166 was tested in similar fashion. Liu et al. [7] reported that micelles are best labelled with isotopes forming aqueous hydroxides. To put this to the test, two extremes were investigated to figure out if the proposed interaction mechanism was indeed needed to gain high labelling efficiency and stability. The two extremes were: loading Dy/Dy-166 in Dy^{3+}-ion form into micelles and loading Dy/Dy-166 by first forming large $Dy(OH)_3$ (s) precipitates and later adding the micelles.
According to chemical speciation analysis with CHEAQS Next [53], Dy mostly exists as Dy^{3+}-ions at lower pH values. To test if these free Dy^{3+}-ions could be loaded, Dy/Dy-166 was added to PCL-PEO micelles without buffer solution. The pH of this mixture was between 3 and 4. After stirring and SEC, the radiolabelling efficiency was 0+/-0%. This showed that the loading of free charged Dy^{3+}-ions into micelles was not possible.
The other extreme was to add Dy/Dy-166 ([Dy] = 2 mM) to HEPES buffer (pH 7.5) and thereby allowing Dy to first form precipitates ($Dy(OH)_3$ (s)) without micelles. The idea here was that before adding micelles, Dy was given more time to make possibly larger precipitates outside the micelles. When the micelles were added after 30 min, the loading was carried out for an additional 30 min. Again the radiolabelling efficiency was found to be 0+/-0%. This meant that when larger $Dy(OH)_3$ (s) precipitates formed outside the micelles, they were not able to penetrate the hydrophilic shell and could therefore not be loaded.

Both these extremes showed that neither Dy^{3+}-ions nor $Dy(OH)_3$ (s) precipitates could be loaded into the micelles. If the loading of Dy into micelles would be possible at all, it would in the middle of these two extremes. This is where the loading procedure developed by Liu et al. [7] was employed.

During the loading procedure, the PCL-PEO micelles were first mixed with a buffer before the Dy was added. The minimum concentration of Dy was limited by the total activity of an irradiated $Dy(NO_3)_3 \cdot H_2O$ or Dy_2O_3 sample. At this minimum and higher concentration, it was not possible for $Dy(OH)_3$ (aq) or other aqueous Dy complexes to form according to CHEAQS Next [53]. Therefore it was decided to still add the Dy at different concentrations and pH values. The idea was that it could be possible that precipitates ($Dy(OH)_3$ (s)) were not formed immediately, but $Dy(OH)^{2+}$ and $Dy(OH)_2^+$ were formed first. These charged hydroxide Dy forms might be able to enter the micelles. The other idea was that Dy could form $Dy(OH)_3$ (s) precipitates that were still small enough to enter the micelles.
It was found that at pH 7.5 and [Dy] = 0.7 mM, the labelling efficiency was highest, namely 3.0+/-0.3% with a mass loading Dy of 18+/-1.8 nmol. Hence it was confirmed that there was some loading of Dy, either in $Dy(OH)^{2+}$, $Dy(OH)_2^+$ or $Dy(OH)_3$ (s) form. The stability revealed to be poor, as the longer a DTPA challenge took place, the more Dy was taken out of the micelles (see figure 4.7). Loading Dy of at the used concentrations and pH values thus proved to give poor results. It was unsure whether Dy was able to form $Dy(OH)_3$ (s) yet and in which state Dy was inside the micelles once loaded.

Next, the influence of the loading time on the labelling efficiency and stability was tested. The loading time was increased from 1 hour to 18 hours. This was done, because the CHEAQS Next software [53] used for chemical speciation analysis assumes chemical equilibrium between the chemical species. The idea was that a longer loading time could potentially increase the loading stability by allowing for chemical equilibrium to be established. The potentially formed $Dy(OH)^{2+}$, $Dy(OH)_2^+$ or $Dy(OH)_3$ (s) would have more time to enter the micelles. As described by Liu et al. [7], a high concentration inside micelles might lead to the formation of solid precipitates by the metallic species. The solid precipitates would provide a high loading stability.
The increase in loading time turned out not to give a significant increase in labelling efficiency and stability (see figure 4.6). The labelling efficiency of 1 hour loading was 3.0+/-0.3% against 3.28+/-0.13% for 18 hours. The mass loading was 18+/-1.8 nmol for 1 hour against 23.6+/-0.1 nmol for 18 hours. These results were quite similar and therefore it was concluded that chemical equilibrium was already reached for Dy within the 1 hour loading time as prescribed by Liu et al. [7].

Although the labelling efficiency and stability of labelled micelles were low, an important factor in this study was to investigate the ratio between Dy-166 and Ho-166 inside labelled micelles. This gave insight into the influence of internal conversion on the retention of Ho-166 once loaded into the micelles. Once Dy-166 and Ho-166 had reached transient equilibrium, it was expected that Dy-166 contributes around 60% to the total gamma activity and Ho-166 around 40%. If IC caused Ho-166 to get separated from the micelles, it was expected that Dy-166 would contribute for more than 60% to the gamma activity than predicted. If IC would play a role in stability, then Ho-166 would leave the micelles once loaded, or would be easily taken out by the DTPA molecules.
The results shown in figure 4.11 indicated that Dy-166 and Ho-166 were in equilibrium amounts inside the labelled micelles. There was no difference between the ratio of stock Dy-166/Ho-166 and Dy-166/Ho-166 found in micelles and after stability tests. Although the labelling efficiency and stability of Dy/Dy-166 and Ho-166 were low, Ho-166 was retained just as well as Dy/Dy-166, as is confirmed by the results presented in figure 4.12. The 72% Ho-166 loss from a conventional carrier (DOTA) as found by Zeevaart et al. [5] did not appear in this project. The conclusion here was that the loaded micelles prevented the loss of Ho-166 and formed a solution to the IC effects.

The experiments with Ga-68 were performed to act as support for the Dy-166/Ho-166 experiments. The advantage was that Ga-68 could be produced with the Ge-68/Ga-68 generator in the laboratory and non-active gallium could be added to increase the Ga concentration. This allowed the investigation of both $Ga(OH)_3$ (aq) at low Ga concentrations and Ga_2O_3 (s) at high Ga concentrations. If $Ga(OH)_3$ (aq) was loaded as well as In-111 ($In(OH)_3$ (aq)) in Liu et al. [7] and Ga_2O_3 (s) as poorly as $Dy(OH)_3$ (s), it would confirm the proposed interaction mechanism.
At first, the Ga-68 low concentration studies were performed at three different pH values. At pH 5.5,

with [Ga-68] = $3.8 \cdot 10^{-13}$ M, the radiolabelling efficiency was 36.0+/-1.0%. Although the labelling efficiency already revealed to be promising, the stability studies with Ga-68 indicated that the proposed loading mechanism might indeed work for other metallic species.
The retention of Ga-68 was 70.5+/-5.7% (after 1 hour DTPA incubation) compared to a maximum retention of Dy/Dy-166 of 23.4+/-5.2%. Ga-68 was loaded in an environment where it could form $Ga(OH)_3$ (aq) according to CHEAQS Next [53], while Dy could form $Dy(OH)_3$ (s). These findings signalled the importance of the way radioisotopes were loaded into micelles.
The efficiency of loading Ga-68 as $Ga(OH)3$ (aq) was further confirmed in the high concentration experiments with Ga/Ga-68. In the high concentration experiments, Ga/Ga-68 could form Ga_2O_3 (s). In this environment, the loading of a high concentration of Ga gave similar results to loading of Dy as $Dy(OH)_3$ (s). Both species proved to load more difficult into micelles than aqueous hydroxides. Furthermore, the retention for both Ga_2O_3 (s) and $Dy(OH)_3$ (s) showed to be poor.
These findings confirm that the interaction mechanism as proposed by Liu et al. [7] correctly predicted that aqueous hydroxides are easily loaded into the micelle, where they are retained and likely form solid precipitates. In an environment where metallic species can form solid hydroxide or oxide complexes, some loading takes place. However, this loading is not retained.

From the Dy/Dy-166 loading results and their comparison to loading aqueous hydroxides with Ga-68 and In-111, it is clear that the Dy-166/Ho-166 generator in the current form is not suitable for micelle applications. Typical activities used in cancer treatments are in the order of GBq [14, 35, 70]. With a labelling efficiency of 3.0+/-0.3%, loading would have to be done with 100 GBq to 1 TBq Dy-166/Ho-166 activity. Despite the deficient results for the Dy-166/Ho-166, it did provide further insight into the loading mechanism of metal ions into micelles. In order for micelles to be radiolabelled efficiently, the isotopes must be in an aqueous hydroxide form to have high labelling efficiency and high stability.

6

Conclusions and recommendations

6.1. Conclusions

The main objective of this thesis was to investigate and understand the loading mechanism of metallic species into polymeric micelles as proposed by Liu et al. [7] study it for Dy and Ho for the application of the Dy-166/Ho-166 generator.

The first goal was to investigate whether Dy could be loaded into polymeric micelles and what the mechanism behind this loading was. It was found the the loading of free ions and solid precipitates into the micelles is not effective. The results with Dy/Dy-166 and Ga/Ga-68 showed that aqueous hydroxides play an important role in achieving a good loading and high stability.
The second goal was to found out if the use of micelles could positively influence the retention of Ho-166. The 72% loss of Ho-166 attributed by internal conversion from a conventional carrier reported by Zeevaart et al. [5] was not seen in the stability studies. The ratio Dy-166/Ho-166 inside the micelles and after stability studies were as predicted for Dy-166/Ho-166 in transient equilibrium. Hence it was concluded that micelles prevented the loss of Ho-166 under IC effects.

With the low radiolabelling efficiency and poor stability, it was further concluded that the Dy-166/Ho-166 generator in the current form is not a suitable candidate for micelle application in RNT. The labelling efficiency is too low and the poor stability indicate that the Dy, Dy-166 and hence Ho-166 were not retained inside the micelle core. For RNT, this is highly undesired.

6.2. Recommendations

Dysprosium is able to form $Dy(OH)_3$ (aq) at lower concentrations (10^{-8} M and lower) at pH 9 according to chemical speciation analysis, see table B.4, Appendix B. With the hypothesized interaction mechanism and the insights gained in this report, Dy is expected to have higher labelling efficiency and higher stability in PCL-PEO micelles when loaded as $Dy(OH)_3$ (aq). It is expected that with the loading of Dy as $Dy(OH)_3$ (aq), high enough concentrations in the micelles could be reached for aqueous ions to form solid precipitates. The only way that it is viable for studying lower Dy concentrations, is if the specific activity of Dy could be higher. The maximum concentration at which $Dy(OH)_3$ (aq) is present is around 10^{-8} M (pH 9). The lowest [Dy] concentration used in this project was 0.2 mM. Hence in order to properly study the loading of $Dy(OH)_3$ (aq), the specific activity of the Dy/Dy-166 stock must be at least 20000 times higher. In practise, this means irradiation with a higher neutron flux and for a longer time. An increase in the presence of Dy-166 in the Dy/Dy-166 stock would allow studying of lower concentrations of Dy for the loading into micelles.

In the study done by Liu et al. [7], cryogenic electron microscopy images were captured at different times during the loading procedure of Indium species into PCL-PEO micelles. These images can be found in Appendix A, figure A.8. Similar studies can be performed for Dy and for Ga to investigate why the behaviour between the isotopes is different. After $Dy(OH)_3$ (s) was loaded, it was expected

to be in $Dy(OH)_3$ (s) form in the core as well. However, the stability tests and the comparison with the retention of Ga-68 and In-111 have shown that $Dy(OH)_3$ (s) was not retained. With cryogenic electron microscopy images, it can be visualized if Dy forms large precipitates in the micelles. Cryogenic electron microscopy could also be used to compare the difference in size between the Dy hydroxides, Ga hydroxides and In hydroxides as used in Liu et al. [7] formed outside the micelles. This could be done by starting a loading experiment and freeze the samples at different times, for example 2 min, 10 min, 30 min and 1 hour. This would give visual insight into where the isotopes form precipitates and how the loading of $Dy(OH)_3$ (s) differs from the loading of Ga/Ga-68 and In/In-111 in aqueous hydroxide form.

A previous MSc thesis done by Villareal-Gómez [71] looked into the use of phosphate-ions ($(PO_4)^{3-}$) to increase the labelling efficiency and stability of the Dy-166/Ho-166 generator. The chemical speciation analysis for adding phosphates to Dy has been done (see Appendix B, section B.3). The idea is that phosphate-ions bind to free Dy^{3+}-ions to form $DyPO_4$ (s). The addition of phosphates in the form of phosphate buffer saline had a significant impact on the stability of micelles loaded with Lu-177 and Zr-89 in Liu et al. [7]. The phosphate ions stimulated the formation of precipitates inside the micelle core. This idea could be explored to determine the maximum size limit for Dy aggregates to enter the micelles by varying the amount of phosphates and whether this influences the stability of Dy in the micelles.

References

[1] National Research Council (US) and Institute of Medicine (US) Committee. *Advancing Nuclear Medicine Through Innovation*. National Academies Press, 2007. ISBN: 0-309-11068-8.

[2] X. Zhong et al. “Polydopamine as a Biocompatible Multifunctional Nanocarrier for Combined Radioisotope Therapy and Chemotherapy of Cancer”. In: *Adv. Funct. Mater.* 25 (2015), pp. 7327–7336. DOI: 10.1002/adfm.201503587.

[3] M. et al. Stella. “Holmium-166 Radioembolization: Current Status and Future Prospective”. In: *Cardiovascular and interventional radiology* 45.11 (2022), pp. 1634–1645. DOI: doi:10.1007/s00270-022-03187-y.

[4] J.K. Kim et al. “Long-term Clinical Outcome of Phase IIb Clinical Trial of Percutaneous Injection with Holmium-166/Chitosan Complex (Milican) for the Treatment of Small Hepatocellular Carcinoma”. In: *Clinical Cancer Research* 12 (2006), pp. 543–548. DOI: https://doi.org/10.1158/1078-0432.CCR-05-1730.

[5] et al. Zeevaart J. “Recoil and conversion electron considerations of the Dy-166/Ho-166 in vivo generator”. In: *Radiochimica Acta* 99 (2011). DOI: 10.1524/ract.2011.1841.

[6] Yoon Jeong Park et al. “Radioisotope carrying polyethylene oxide–polycaprolactone copolymer micelles for targetable bone imaging”. In: *Biomaterials* 23.3 (2002), pp. 873–879. DOI: https://doi.org/10.1016/S0142-9612(01)00196-X.

[7] Huanhuan Liu. “Application of Poly (ϵ-caprolactone-b-ethylene oxide) Micelles Combined with Ionizing Radiation in Cancer Treatment”. PhD thesis. Delft University of Technology, 2021.

[8] S.M. Qiam. “Nuclear data for production and medical application of radionuclides: Present status and future needs”. In: *Nuclear Medicine and Biology* 44 (2017), pp. 31–49. ISSN: 0969-8051. DOI: https://doi.org/10.1016/j.nucmedbio.2016.08.016. URL: https://www.sciencedirect.com/science/article/pii/S0969805116302190.

[9] A. Dash, F.F. Knapp, and M.R. Pillai. “Targeted radionuclide therapy - an overview”. In: *Curr. Radiopharm.* 6, 3 (2013), pp. 150–80. DOI: 10.2174/1874471011306666002.

[10] D.E. Milenic, E.D. Brady, and M.W. Brechbiel. “Antibody-targeted radiation cancer therapy”. In: *Nat. Rev. Drug Discov.* 3 (2004), pp. 488–499. DOI: https://doi.org/10.1038/nrd1413.

[11] D. Eriksson and T. Stigbrand. “Radiation-induced cell death mechanisms”. In: *Tumor Biol.* 31 (2010), pp. 363–372. DOI: 10.1007/s13277-010-0042-8.

[12] S.V. Smith et al. “[166Dy]Dysprosium/[166Ho]Holmium In Vivo Generator”. In: *Appl. Radiat. Isot.* 46, 8 (1995), pp. 759–764. DOI: https://doi.org/10.1016/0969-8043(94)00149-t.

[13] N. Salek, S. Vosoughi, and B. Samani. “Radiolabeled TPP with 166Dy/166Ho in vivo generator as a novel therapeutic agent”. In: *J. Radioanal. Nucl. Chem.* 326 (2020), pp. 813–821. DOI: https://doi.org/10.1007/s10967-020-07364-6.

[14] N.J.M. Klaassen et al. “The various therapeutic applications of the medical isotope holium-166: a narrative review”. In: *EJNMMI radiopharm. chem.* 4, 19 (2019). DOI: https://doi.org/10.1186/s41181-019-0066-3.

[15] R. Wang et al. “Core–shell structured gold nanoparticles as carrier for 166Dy/166Ho in vivo generator”. In: *EJNMMI radiopharm. chem.* 7, 16 (2022). DOI: https://doi.org/10.1186/s41181-022-00170-3.

[16] P.E. Edem et al. “In Vivo Radionuclide Generators for Diagnostics and Therapy”. In: *Bioinorg Chem Appl.* 2016 (2016). DOI: doi:10.1155/2016/6148357.

[17] T. Das and M.R.A. Pillai. “Options to meet the future global demand of radionuclides for radionuclide therapy”. In: *Nuclear medicine and biology* 40 (2013), pp. 23–32. DOI: doi:10.1016/j.nucmedbio.2012.09.007.

[18] S. Gudkov et al. “Targeted Radionuclide Therapy of Human Tumors”. In: *International journal of molecular sciences* 17 (2015), pp. 103–124. DOI: doi:10.3390/ijms17010033.

[19] Meghana Parsi et al. “PSMA: a game changer in the diagnosis and treatment of advanced prostate cancer”. In: *Medical Oncology* 38 (Aug. 2021). DOI: 10.1007/s12032-021-01537-3.

[20] M. Makrigiorgos, S. Adelstein, and A. Kassis. “Auger electron emitters: Insights gained from in vitro experiments”. In: *Radiation and environmental biophysics* 29 (Feb. 1990), pp. 75–91. DOI: 10.1007/BF01210552.

[21] R.B. Michel, M.W. Brechbiel, and M.J. Mattes. “A Comparison of 4 Radionuclides Conjugated to Antibodies for Single-Cell Kill”. In: 44.4 (2003), pp. 632–640.

[22] United States Nuclear Regulatory Commission. *Effective half-life*. 2021. URL: https://www.nrc.gov/reading-rm/basic-ref/glossary/effective-half-life.html# (visited on 10/15/2023).

[23] Y. et al. Chai-Hong. “Therapeutic radionuclides in nuclear medicine: current and future prospects”. In: *Journal of Zhejiang University* 15.10 (2014), pp. 845–863. DOI: doi:10.1631/jzus.B1400131.

[24] R. Lambrecht, K. Tomiyoshi, and T. Sekine. “Radionuclide Generators”. In: *Radiochimica Acta* 77 (1997), pp. 103–124. DOI: https://doi.org/10.1524/ract.1997.77.12.103.

[25] Jerzy Cetnar. “General solution of Bateman equations for nuclear transmutations”. In: *Annals of Nuclear Energy* 33.7 (2006), pp. 640–645. ISSN: 0306-4549. DOI: https://doi.org/10.1016/j.anucene.2006.02.004.

[26] V. Gopalakrishnan. *Physics of Nuclear Reactors, Chapter 2 - Nuclear Data*. Academic Press, 2021. ISBN: 9780128224410.

[27] IAEA. *Principles of radionuclide generators*. 2016. URL: https://humanhealth.iaea.org/HHW/Radiopharmacy/VirRad/Eluting_the_Generator/Generator_Module/Principles_of_radionuclide_generators/index.html (visited on 08/28/2023).

[28] R. Gupta and M.F. Hashmi. *Mo99 - Tc99m Generator*. StatPearls Publising, Treasure Island, 2023. ISBN: 9780128224410.

[29] R.G. Helmer and S.B. Burson. “Decay of $_{66}Dy^{166}$”. In: *Phys. Rev.* 119 (2 1960), pp. 788–795. DOI: 10.1103/PhysRev.119.788.

[30] S.Y.F. Chu, L.P. Ekström, and R.B. Firestone. *The Lund/LBNL Nuclear Data Search*. 1999. URL: http://nucleardata.nuclear.lu.se/toi/index.asp (visited on 05/23/2023).

[31] S. Thompson and et al. “166Ho and 90Y labeled 6D2 monoclonal antibody for targeted radiotherapy of melanoma: comparison with 188Re radiolabel”. In: *Nuclear medicine and biology* 41,3 (2014), pp. 276–281. DOI: doi:10.1016/j.nucmedbio.2013.12.015.

[32] D. Nayak and S. Lahiri. “Application of radioisotopes in the field of nuclear medicine”. In: *J. Radioanal. Nucl. Chem.* 242 (1999), pp. 423–432. DOI: https://doi.org/10.1007/BF02345573.

[33] M. Pedraza-Lopéz et al. “Preparation of (166)Dy/(166)Ho-EDTMP: a potential in vivo generator system for bone marrow ablation”. In: *Nuclear medicine communications* 25,6 (2004), pp. 615–621. DOI: doi:10.1097/01.mnm.0000126516.57329.07.

[34] C.R. Nave. *Radioactivity - Internal conversion*. 2017. URL: http://hyperphysics.phy-astr.gsu.edu/hbase/Nuclear/radact2.html (visited on 09/03/2023).

[35] M. Schmidt et al. “(68)Ga-DotaTATE PET-CT followed by Peptide Receptor Radiotherapy in combination with capecitabine in two patients with Merkel Cell Carcinoma”. In: *International journal of clinical and experimental medicine* 5 (Sept. 2012), pp. 363–6.

[36] D.E. Bergeron, J.T. Cessna, and B.E. Zimmerman. “Two determinations of the Ge-68 half-life.” In: *Appl Radiat Isot.* 134 (Apr. 2018), pp. 416–420. DOI: doi:10.1016/j.apradiso.2017.10.038.

[37] F. van Wyngaardt et al. “Development of the Australian Standard for Germanium-68 by two Liquid Scintillation Counting methods”. In: *Applied Radiation and Isotopes* 134 (Oct. 2017). DOI: 10.1016/j.apradiso.2017.10.005.

[38] Laboratory National Henri Becquerel. *Atmoic and Nuclear data*. 2012. URL: http://www.lnhb.fr/nuclear-data/nuclear-data-table/ (visited on 07/26/2023).

[39] L.M. Plum, L. Rink, and H. Haase. “The Essential Toxin: Impact of Zinc on Human Health”. In: *International Journal of Environmental Research and Public Health* 7.4 (2010), pp. 1342–1365. DOI: 10.3390/ijerph7041342.

[40] M. Ghezzi et al. “Polymeric micelles in drug delivery: An insight of the techniques for their characterization and assessment in biorelevant conditions”. In: *Journal of Controlled Release* 332 (2 2021), pp. 312–336. DOI: https://doi.org/10.1016/j.jconrel.2021.02.031.

[41] R. Paliwal, R.J. Babu, and S. Palakurthi. “Nanomedicine Scale-up Technologies: Feasibilities and Challenges”. In: *AAPS PharmSciTech* 15 (2014), pp. 1527–1534. DOI: https://doi.org/10.1208/s12249-014-0177-9.

[42] V. Gadekar et al. “Nanomedicines accessible in the market for clinical interventions”. In: *Journal of Controlled Release* 330 (2021), pp. 372–397. DOI: https://doi.org/10.1016/j.jconrel.2020.12.034.

[43] D.J.A. Crommelin, P. Van Hoogevest, and G. Storm. “The role of liposomes in clinical nanomedicine development. What now? Now what?” In: *Journal of Controlled Release* 318 (2020), pp. 256–263. DOI: https://doi.org/10.1016/j.jconrel.2019.12.023.

[44] S. Rana et al. *Chapter 7 - Interfacial engineering of nanoparticles for cancer therapeutics*. Ed. by Anton Ficai and Alexandru Mihai Grumezescu. Elsevier, 2017, pp. 177–209. ISBN: 978-0-323-46144-3. DOI: https://doi.org/10.1016/B978-0-323-46144-3.00007-6.

[45] D. Sharma et al. “Chapter 13 - Diblock and triblock copolymers of polylactide and polyglycolide”. In: *Materials for Biomedical Engineering*. Ed. by Valentina Grumezescu and Alexandru Mihai Grumezescu. Elsevier, 2019, pp. 449–477. ISBN: 978-0-12-816874-5. DOI: https://doi.org/10.1016/B978-0-12-816874-5.00013-X. URL: https://www.sciencedirect.com/science/article/pii/B978012816874500013X.

[46] B. Hammouda, D. Ho, and S. Kline. “Insight into Clustering in Poly(ethylene oxide) Solutions”. In: *Macromolecules* 37 (Sept. 2004). DOI: 10.1021/ma049623d.

[47] C. Angeliki, T. Mavromoustakos, and S. Pispas. “Biocompatible PEO-b-PCL Nanosized Micelles as Drug Carriers: Structure and Drug-Polymer Interactions”. In: *Nanomaterials* 10 (2020). DOI: doi:10.3390/nano10091872.

[48] H. Liu et al. “Combined Chemoradionuclide Therapy Using Poly(ε-caprolactone-b-ethylene oxide) Micelles as the Delivery Vehicle”. In: *Advanced Therapeutics* 6.5 (). DOI: https://doi.org/10.1002/adtp.202200224.

[49] Jun Wu. “The Enhanced Permeability and Retention (EPR) Effect: The Significance of the Concept and Methods to Enhance Its Application”. In: *Journal of Personalized Medicine* 11 (Aug. 2021), p. 771. DOI: 10.3390/jpm11080771.

[50] Y. Nakamura et al. “Nanodrug Delivery: Is the Enhanced Permeability and Retention Effect Sufficient for Curing Cancer?” In: *Bioconjugate chemistry* 27 (2016), pp. 2225–2238. DOI: https://doi.org/10.1021/acs.bioconjchem.6b00437.

[51] A. Varela-Moreira et al. “Clinical application of polymeric micelles for the treatment of cancer”. In: *Mater. Chem. Front.* 1 (2017), pp. 1485–1501. DOI: https://doi.org/10.1039/C6QM00289G.

[52] Y. Shi et al. “The EPR effect and beyond: Strategies to improve tumor targeting and cancer nanomedicine treatment efficacy”. In: *Theranostics* 10 (2020), pp. 7921–7924. DOI: 10.7150/thno.49577. URL: https://www.thno.org/v10p7921.htm.

[53] W. Verweij. *CHEAQS Next (64 bits)*. Version 0.2.1.8. July 6, 2023. URL: https://www.cheaqs.eu/index.html.

[54] H. Liu et al. “Efficient Radiolabeling of Block Copolymer Micelles through Radiometal Salt Precipitation for Theranostic Applications”. In: *Advanced Therapeutics* 5.9 (2022). DOI: https://doi.org/10.1002/adtp.202200077.

[55] P.M.V. Raja and A.R. Barron. *2.4: Dynamic Light Scattering*. 2023. URL: https://chem.libretexts.org/Bookshelves/Analytical_Chemistry/Physical_Methods_in_Chemistry_and_Nano_Science_(Barron)/02%3A_Physical_and_Thermal_Analysis/2.04%3A_Dynamic_Light_Scattering (visited on 09/04/2023).

[56] R. Sandhu et al. *Dynamic light scattering (DLS) technique, principle, theoretical considerations and applications*. Jan. 2018, pp. 135–137.

[57] P. Hong, S. Koza, and E.S.P. Bouvier. In: *Journal of liquid chromatography and related technologies* 35 (2012). DOI: doi:10.1080/10826076.2012.743724.

[58] D.S.K. Liu et al. In: *Cancers* 12.11 (2020). URL: https://www.mdpi.com/2072-6694/12/11/3156.

[59] BioRender. 2023. URL: https://www.biorender.com/ (visited on 08/14/2023).

[60] W. Boeglin. *22. Scintillation Detector*. 2023. URL: https://wanda.fiu.edu/boeglinw/courses/Modern_lab_manual3/scintillator.html (visited on 09/05/2023).

[61] M.L.C. Passos and M.L.M.F. Saraiva. "Detection in UV-visible spectrophotometry: Detectors, detection systems, and detection strategies". In: *Measurement* (2018). DOI: https://doi.org/10.1016/j.measurement.2018.12.045.

[62] M. García-León. "Semiconductor Detectors". In: *Detecting Environmental Radioactivity*. Springer International Publishing, 2022, pp. 339–374. ISBN: 978-3-031-09970-0. DOI: 10.1007/978-3-031-09970-0_11.

[63] G. Knoll. *Radiation Detection and Measurement*. Jan. 2000. ISBN: 0-471-07338-5.

[64] Mirion Technolgies. *Low Energy Germanium Detector (LEGe)*. 2016. URL: https://www.gammadata.se/assets/Uploads/LEGe-SS-C49322.pdf (visited on 08/23/2023).

[65] S.R. Cherry et al. *Physics in Nuclear Medicine (Fourth Edition)*. 2012. ISBN: 9781416051985.

[66] Perkin Elmer. *2480 WIZARD2 Automatic Gamma Counters*. 2011. URL: https://resources.perkinelmer.com/corporate/cmsresources/images/46-129502spc_02_wizard_2480_final.pdf (visited on 08/23/2023).

[67] LabX. *Perkin Wizard2 3" Gamma Counter 2480-0010 (1) Detector - AV*. 2022. URL: https://www.labx.com/item/perkin-wizard2-3-gamma-counter-2480-0010-1-detector/14544270 (visited on 08/23/2023).

[68] Canberra/Mirion Technolgies. *Genie 2000 Gamma Acquisition and Analysis*. Version 3.2. Mar. 18, 2009. URL: https://www.mirion.com/products/technologies/spectroscopy-scientific-analysis/gamma-spectroscopy/gamma-spectroscopy-software/lab-applications/genie-spectroscopy-software-suite.

[69] Canberra/Mirion Technolgies. *Genie 2000 Gamma Acquisition and Analysis*. Version 3.2.1. Aug. 26, 2009. URL: https://www.mirion.com/products/technologies/spectroscopy-scientific-analysis/gamma-spectroscopy/gamma-spectroscopy-software/lab-applications/genie-spectroscopy-software-suite.

[70] M.T. Sapienze and J. Willegaigon. "Radionuclide therapy: current status and prospects for internal dosimetry in individualized therapeutic planning". In: *Clinics* 74 (2019). DOI: doi:10.6061/clinics/2019/e835.

[71] V. Villarreal Gómez. "Polyermic micelles as carrier fir a Dy-166/Ho-166 in vivo generator". Master's Thesis. Delft University of Technology, 2022.

[72] D.J. Adams et al. "On the mechanism of formation of vesicles from poly(ethylene oxide)-block-poly(caprolactone) copolymers". In: *Soft Matter* 5 (16 2009), pp. 3086–3096. DOI: 10.1039/B907628J. URL: http://dx.doi.org/10.1039/B907628J.

[73] R. Nagarajan and K. Ganesh. "Block copolymer self assembly in selective solvents: Spherical micelles with segregated cores". In: *J. Chem. Phys.* 90 (May 1989), pp. 5843–5856. DOI: https://doi.org/10.1063/1.456390.

[74] E. Struick. "Small-angle X-ray Scattering Capabilities for Investigating Indium Ion Encapsulation in PEO-PCL Micelles". Master's Thesis. Delft University of Technology, 2023.

A

Appendix

A.1. DLS measurement of polymeric micelles

Below, two DLS measurements are shown for PCL-PEO [2800-2000] micelles. Two samples were measured from the same micelles batch.

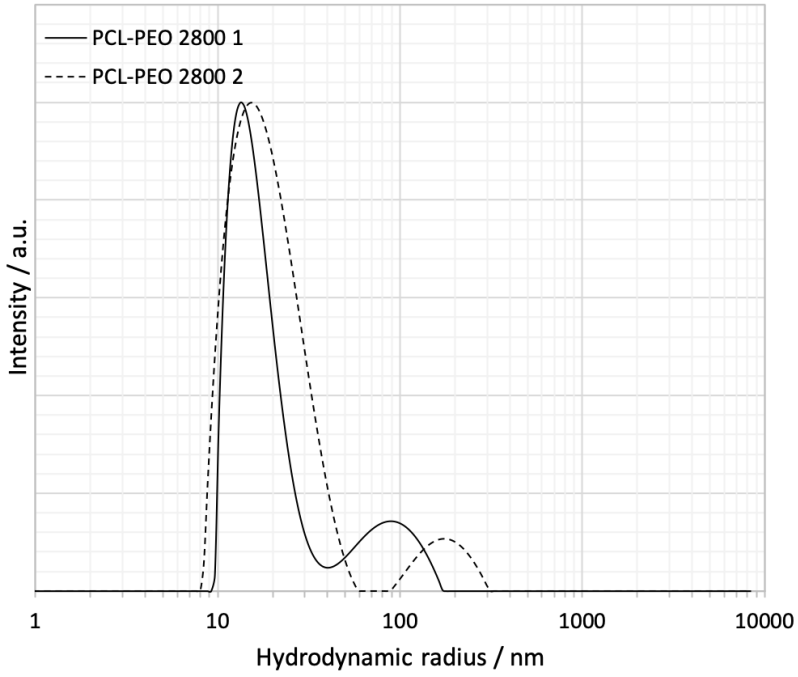

Figure A.1: The size distribution of polymeric micelles before filtration, determined with in two measurements from the same micelle sample. The polymer concentration was 9.2 mg/mL for the DLS measurement.

The hydrodynamic radii were measured to be 20 and 17 nm for PCL-PEO 2800 1 and 2 respectively. In the next section, calculations are made to estimate to concentration of dysprosium inside the micelle core. From the results found above, it is clear that there is a spread in the micelle size distribution. The estimates should therefore be seen as highly rough estimates, solely having the purpose of giving a feel and insight into the 'numbers' of these experiments.

A.2. Counts per fraction

In figure A.2, a graph is presented that shows the fractions in which the Dy-166/Ho-166 labelled micelles came off the SEC columns. The labelled micelles were typically found in fractions 10-14. Per fraction,

one milliliter was collected.

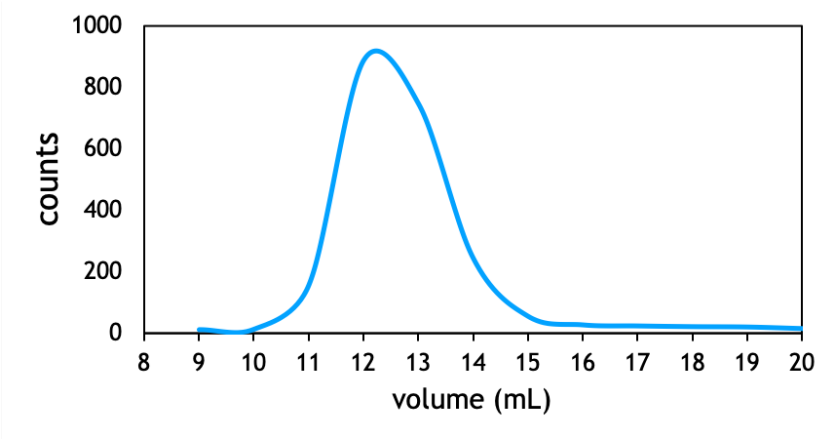

Figure A.2: Counts per fraction for Dy-166/Ho-166 loading experiments with PCL-PEO [2800-2000] micelles. The micelles typically appeared between fraction 10-14. One milliliter was collected per fraction.

Figure A.3 shows a graph with counts per fraction after Dy-166/Ho-166 labelled micelles had undergone a 2 hour DTPA challenge. The DTPA-radionuclide complexes typically appeared in fractions 16-20.

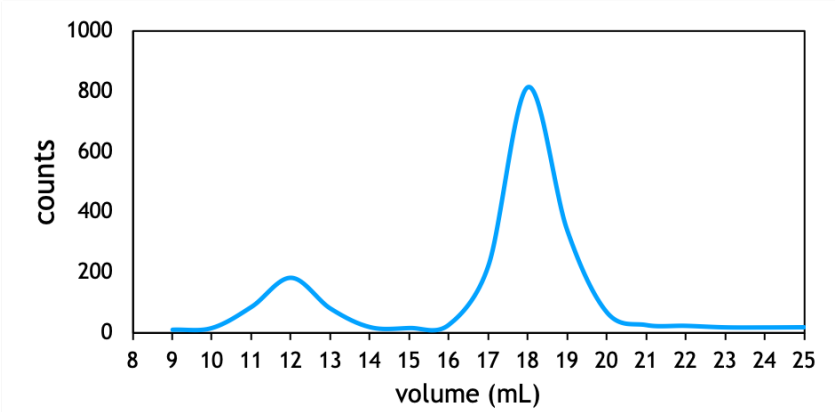

Figure A.3: Counts per fraction for after 2 hour DTPA challenge with PCL-PEO [2800-2000] micelles labelled with Dy-166 for 18 hours. One milliliter was collected per fraction. There is good separation between the micelles and DTPA-complex.

A.3. Calculation amount of micelles and concentration inside core

The PEO-b-PCL micelles are made by adding 20 mg of PEO-b-PCL to 0.2 mL chloroform and 2.3 mL MQ. Assuming that the chloroform evaporates during the self-assembly step of the micelle synthesis, the amount of the PEO-b-PCL is 8.69 mg/mL. Per sample with HEPES and radioactive metal ions, 0.5 mL of micelle solution is used, amounting to 4.35 mg PEO-b-PCL per sample. The molecular weight of PEO-b-PCL [2000 2800] is 4800 g/mol.
The amount of mol n of copolymer is then calculated by dividing the mass by the molar mass. This gives $m = 9.06 \cdot 10^{-7}$ mol polymer. The number of co-polymers in the solution is calculated by multiplying the amount of mol with Avogadro's number (N_A).

$$n \times N_A = 9.06 \cdot 10^{-7}\text{mol} \times 6.022 \cdot 10^{23} = 5.46 \cdot 10^{17} \text{ copolymers}$$

The aggregation number N_{agg} refers to number of (co)polymers making up a micelle. It can be used to estimate the amount of micelles that are formed by self-assembly. In order studies, the aggregation number was determined with Static Light Scattering (SLS) or found with thermodynamic models. For

vesicles composed of the same block co-polymer with similar weight as PEO-b-PCL [2000-b-2800], the aggregation number was found to be 97300. for PEO-b-PCL [2300 2800] with the same molecular mass equals 97300 [72]. It should be noted that the number of polymers per micelle in [72] refers to vesicles and the PEO segment is 2300 g/mol. A similar paper by Nagarajan et al. [73] studying self-assembly of block co-polymers to form micelles used thermodynamic models to estimate the aggregation number for various types of block co-polymers. The block co-polymer resembling PEO-b-PCL [2000-b-2800] is PEO-PPO-water with a weight of 4750 g/mol, with an aggregation number of 976.
With this information, the amount of micelles in the loading experiments with PEO-b-PCL [2000-b-2800] is

$$\text{amount of micelles} = \frac{\text{amount of copolymers}}{N_{agg}}$$

Under optimal loading conditions (pH 7.5, [Dy] = 0.7 mM), the mass loading of dysprosium reached 23.6 nmol 4.3 for 18 hours loading time. The loading is divided over the micelles, hence

$$\text{loading per micelle} = \frac{\text{dysprosium loading (mol)}}{\text{amount of micelles}}$$

All that remains is determine the volume of the micelle core, in which case the concentration of dysprosium inside the micelle can be calculated. The core radius of the same micelle type was determined in the Master Thesis done by Struick [74], with an average radius of 94 Å. Assuming a perfect sphere, the volume of the core is 2.58E-23 m^3.
Then, for both aggregation numbers, the dysprosium concentration inside the micelles is as follows (see A.1).

Table A.1

literature	polymer	weight	h. radius	core radius	N_{agg}	[Dy] core
Nagarajan [73]	PEO-PPO-water	4750 g/mol	113 Å	70 Å	976	1.64E-3
Adams [72]	PEO23-b-PCL28	4800 g/mol	83 Å	x	97300	1.63E-1

From the dysprosium speciation found in appendix B, for a pH of 7 and higher, dysprosium forms $Dy(OH)_3$ (s) under these concentrations. Assuming the micelle core contains dysprosium hydroxides (s), water and HEPES with corresponding pH, the core should contain $Dy(OH)_3$ (s).

It must be pointed out that these calculations assume no losses and that all polymers form micelles.

A.4. Holmium concentration estimate

These two graphs are estimates of the mass loading and concentration of holmium during and after the loading procedure. The calculations are based on those done for dysprosium in section A.3.

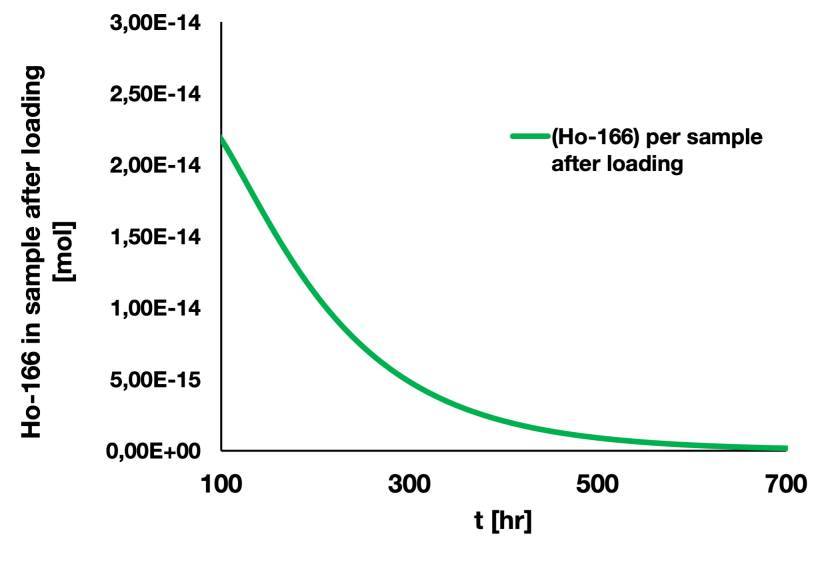

Figure A.4: The mass loading of Ho-166 inside the PCL-PEO [2800-2000] micelles as it decays over time. Time t=100 hr is the moment at which the holmium was loaded into the micelles when t=0 hr after the Dy_2O_3 was irradiated and went through a cooling period. The labelling efficiency for the calculation was 3%.

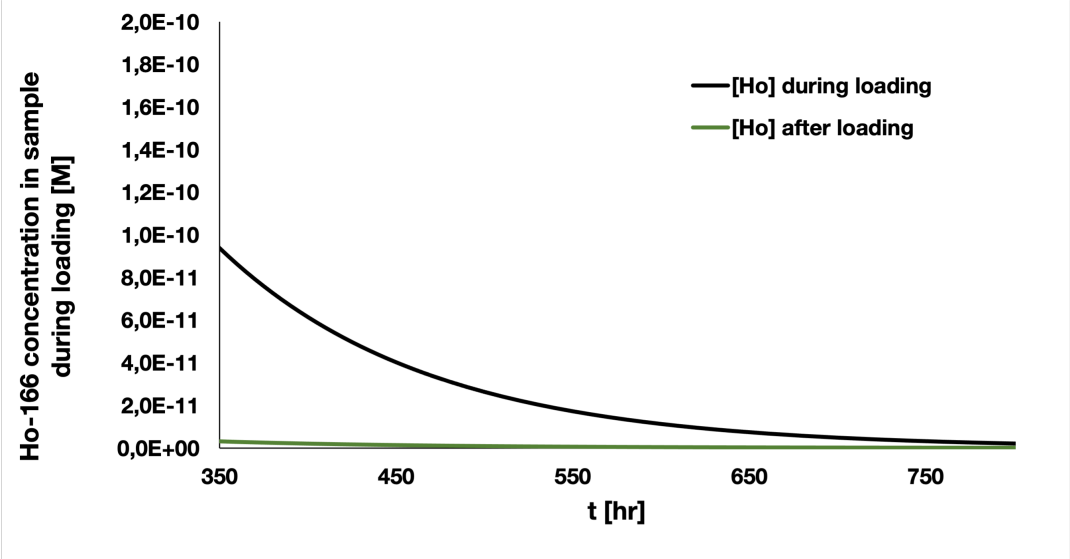

Figure A.5: The concentration of Holmium during the loading procedure (black line) and the actual concentration inside the micelles once the holmium is loaded. The concentration dysprosium was 0.7 mM during loading. The results are based on a radiolabelling efficiency of 3.0+/-0.3%. The actual loading took place at around 350 hr. t=0 hr is the time at which the cooling period of the irradiated Dy_2O_3 started.

A.5. Temperature influence on loading of Dy-166/Ho-166

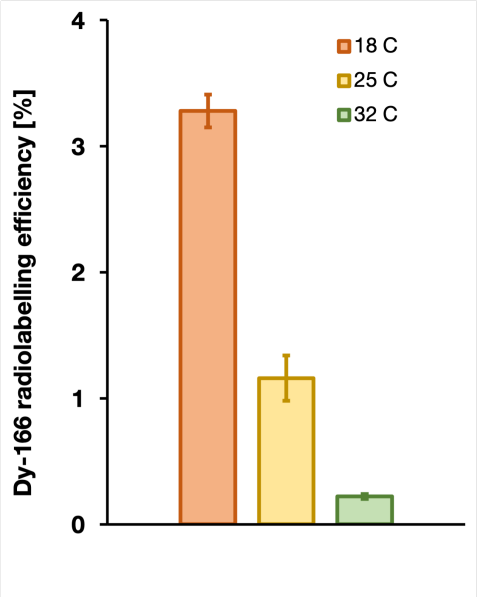

Figure A.6: Temperature influence on dysprosium radiolabelling efficiency under optimal loading conditions ([Dy] = 0.7 mM, pH 7.5) in PCL-b-PEO [2800-b-2000] micelles.

The results above show the difference in labelling efficiency at different lab temperatures. The temperaturs were estimated from a clock-thermostat in the lab and is to be taken as an estimate. Still, the difference in temperature is significant: 3.28+/-0.13% (18 C), 1.16+/-0.18% (25 C) and 0.22+/-0.02% (32 C). After airconditioning was installed in the laboratories at the beginning of July 2023, the labelling efficiency under the optimal conditions was back to around 3%.

A.6. Enlarged image high-res detector Dy-166 and Ho-166

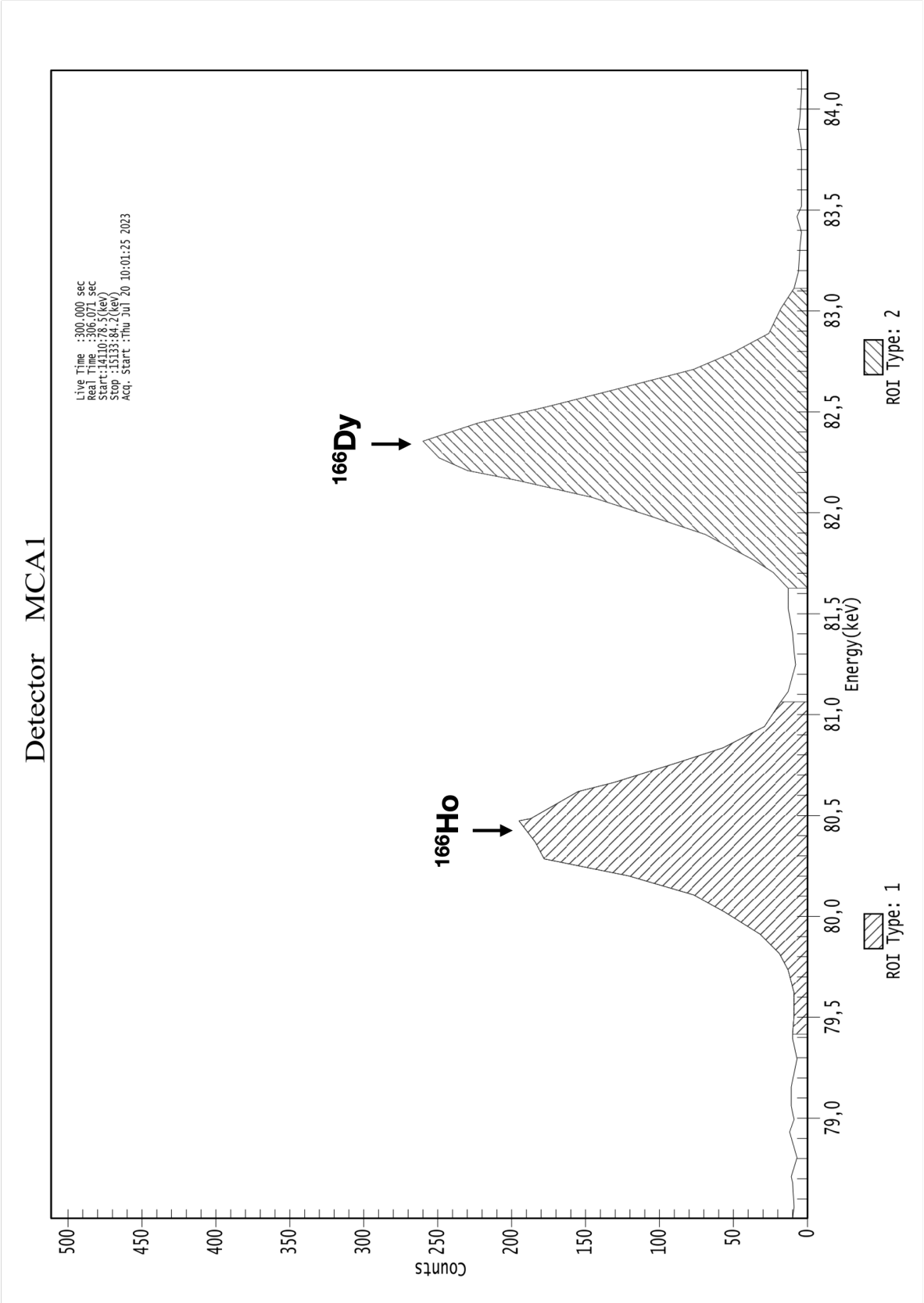

Figure A.7: Enlarged version of figure 4.10: high resolution measurement of Dy-166 and Ho-166 encapsulated in PCL-PEO 2800 micelles.

A.7. Estimation concentration Ga-68 during loading experiments

The concentration of Ga-68 after milking the Ge-/Ga-generator is estimated below.

- Efficiency of measuring Ga-68 activity with Perkin Elmer Wallac gamma counter = 0.0321 Bq/cpm
- Decay constant Ga-68 λ = 1.7062E-04 s^{-1}
- Volume 0.1 M HCl used to extract Ga-68 from generator = 5mL
- Each mL was collected seperately, of which 50 μL was taken to be measured in the Wallac gamma counter. The average was 1579787 cpm. With the efficiency accounted, the total activity of Ga-68 is 4.057 MBq in 5mL 0.1 M HCl
- Amount of Ga-68 atoms can be calculated with A = N $\times\lambda$, hence N = A / λ = 4.057 MBq / 1.7062E-04 s^{-1} = 2.38E10
- Mass of Ga-68 can be calculated with MW(Ga-68) = 67.928 g/mol and N = (mass / MW) $\times$ N_A. Hence the mass Ga-68 is m = (N $\times$ MW) / N_A = (2.38E10 $\times$ 67.928 g/mol)/(6.022E23) = 2.68E-12 gram Ga-68
- Amount of mol n = m / MW = 2.68E-12 gr / 67.928 g/mol = 3.95E-14 mol Ga-68
- In 5 mL, the stock concentration is then 7.90E-12 M
- Volume stock added to micelles = 50 μL
- Volume micelles + buffer = 1 mL
- Concentration Ga-68 per micelle sample = 3.76E-13 M

A.8. Estimation concentration Ga-68 inside micelle core

- Amount of micelles in sample = 5.62·10^{12} (calculated with N_{agg} = 97300 [72])
- Volume micelles + buffer + Ga-68 = 1.05 mL
- Radiolabelling efficiency Ga-68 at pH 5.5 = 36.0+/-1.0%
- Amount of mole Ga-68 inside micelles = 3.76E-13 M * 1.05 mL * 36.0% = 1.42E-16 mol
- Amount of mole Ga-68 per micelle = 1.42E-16 mol / 5.62·10^{12} micelles = 2.53E-29 mol/micelle
- Estimated volume micelle core = 2.58E-23 m^3
- Concentration Ga-68

A.9. Cryogenic electron microscopy images In species

Below, the cryogenic electron microscopy images of loading In species into PCL-PEO micelles done by Liu et al. [7] is shown. The first image, (a) shows empty PCL-PEO micelles, and the mixture on In species and PCL-PEO micelles obtained after reacting for (b) 2 min, (c) 10 min and (d) 30 min.

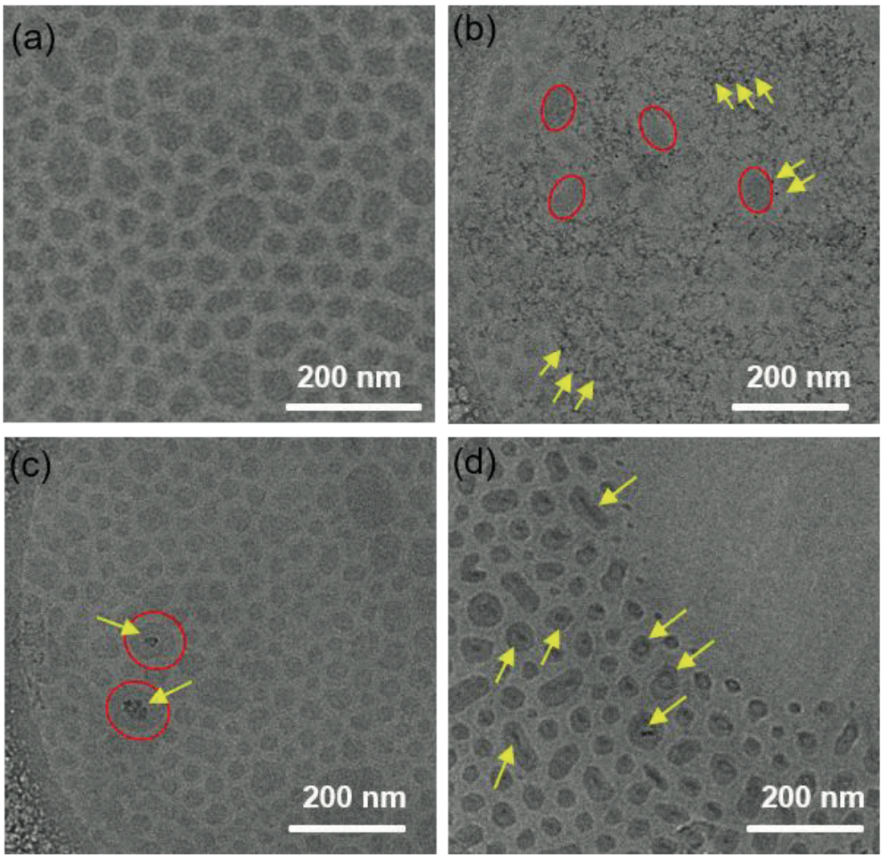

Figure A.8: Cryo-EM images captured by Liu et al. [7] of (a) empty PCL-10000 micelles and In^{3+} species, (b) micelles after reacting for 2 min, (c) 10 min and (d) 30 min. The initial In^{3+} concentration was 0.137 mM in HCl with pH = 2, the concentration of the polymer was 4.3 mg/mL.

As can be seen in figure A.8 (b), aggregates started to appear outisde the micelles. At 10 min (c), the indium aggregation outside the micelles decreased and small dark spots started to appear in the micelle cores. After 30 min (d), most of the micelles contained dark spots.

B

CHEAQS chemical speciation

B.1. Dysprosium speciation

The dysprosium chemical speciation is determined for 25 degrees Celsius in CHEAQS Next.

Table B.1: chemical speciation [%] of dysprosium under pH = 6 and varying concentrations [M].

Dysprosium	Parameters:		Conc(H) 1E-06 M; Allow solids to precipitate			Conc(Cl) 1E-04 M					
Species/[Dy] in M	1E-10	1E-09	1E-08	1E-07	1E-06	1E-05	1E-04	1E-03	1E-02	1E-01	1E-00
free Dy^{3+}	97.54	97.54	97.54	97.54	97.58	97.58	97.74	98.2	98.98	99.36	15.93
$Dy(OH)^{2+}$	2.4	2.4	2.4	2.4	2.39	2.36	2.2	1.75	0.99	0.54	0.1
$Dy(OH)_2^+$	0	0	0	0	0	0	0	0	0	0	0
$Dy(OH)_3$ (aq)	0	0	0	0	0	0	0	0	0	0	0
$Dy(OH)_3$ (s)	0	0	0	0	0	0	0	0	0	0	83.95
$Dy(OH)_4^-$	0	0	0	0	0	0	0	0	0	0	0

Table B.2: chemical speciation [%] of dysprosium under pH = 7 and varying concentrations [M].

Dysprosium	Parameters:		Conc(H) 1E-07 M; Allow solids to precipitate			Conc(Cl) 1E-04 M					
Species/[Dy] in M	1E-10	1E-09	1E-08	1E-07	1E-06	1E-05	1E-04	1E-03	1E-02	1E-01	1E-00
free Dy^{3+}	79.84	79.84	79.84	79.84	79.87	80.07	13.81	1.38	0.14	0	0
$Dy(OH)^{2+}$	19.61	19.61	19.61	19.61	19.59	19.4	3.32	0.33	0	0	0
$Dy(OH)_2^+$	0.48	0.48	0.48	0.48	0.47	0	0	0	0	0	0
$Dy(OH)_3$ (aq)	0	0	0	0	0	0	0	0	0	0	0
$Dy(OH)_3$ (s)	0	0	0	0	0	0	82.87	98.28	99.83	99.98	100
$Dy(OH)_4^-$	0	0	0	0	0	0	0	0	0	0	0

Table B.3: chemical speciation [%] of dysprosium under pH = 8 and varying concentrations [M].

Dysprosium	Parameters:		Conc(H) 1E-08 M; Allow solids to precipitate			Conc(Cl) 1E-04 M				
Species/[Dy] in M	1E-10	1E-09	1E-08	1E-07	1E-06	1E-05	1E-04	1E-03	1E-02	1E-01	1E-00
free Dy^{3+}	23.39	23.39	23.39	13.28	1.33	0.13	0	0	0	0	0
$Dy(OH)^{2+}$	57.46	57.46	57.45	32.62	3.26	0.33	0	0	0	0	0
$Dy(OH)_2^+$	14.01	14.01	14.01	7.95	0.8	0	0	0	0	0	0
$Dy(OH)_3$ (aq)	4.42	4.42	4.42	2.51	0.25	0	0	0	0	0	0
$Dy(OH)_3$ (s)	0	0	0	43.33	94.32	99.43	99.94	99.99	100	100	100
$Dy(OH)_4^-$	0.71	0.71	0.71	0.4	0	0	0	0	0	0	0

Table B.4: chemical speciation [%] of dysprosium under pH = 9 and varying concentrations [M].

Dysprosium	Parameters:		Conc(H) 1E-09 M; Allow solids to precipitate			Conc(Cl) 1E-04 M				
Species/[Dy] in M	1E-10	1E-09	1E-08	1E-07	1E-06	1E-05	1E-04	1E-03	1E-02	1E-01	1E-00
free Dy^{3+}	0.17	0.17	0.13	0	0	0.13	0	0	0	0	0
$Dy(OH)^{2+}$	4.25	4.25	3.29	0.33	0	0.33	0	0	0	0	0
$Dy(OH)_2^+$	10.35	10.35	8	0.8	0	0	0	0	0	0	0
$Dy(OH)_3$ (aq)	32.66	32.66	25.26	2.51	0.25	0	0	0	0	0	0
$Dy(OH)_3$ (s)	0	0	23.09	92.31	99.23	99.92	99.94	99.99	100	100	100
$Dy(OH)_4^-$	52.57	52.57	40.66	4.04	0.4	0	0	0	0	0	0

Table B.5: chemical speciation [%] of dysprosium under pH = 10 and varying concentrations [M].

Dysprosium	Parameters:		Conc(H) 1E-10 M; Allow solids to precipitate			Conc(Cl) 1E-04 M				
Species/[Dy] in M	1E-10	1E-09	1E-08	1E-07	1E-06	1E-05	1E-04	1E-03	1E-02	1E-01	1E-00
free Dy^{3+}	0	0	0	0	0	0	0	0	0	0	0
$Dy(OH)^{2+}$	0	0	0	0	0	0	0	0	0	0	0
$Dy(OH)_2^+$	0.18	0.18	0	0	0	0	0	0	0	0	0
$Dy(OH)_3$ (aq)	5.82	5.82	5.82	2.51	0.25	0	0	0	0	0	0
$Dy(OH)_3$ (s)	0	0	0	56.85	95.69	99.57	99.96	100	100	100	100
$Dy(OH)_4^-$	93.98	93.99	93.99	40.55	4.06	0.41	0	0	0	0	0

Table B.6: chemical speciation [%] of dysprosium under pH = 11 and varying concentrations [M].

Dysprosium	Parameters:		Conc(H) 1E-11 M; Allow solids to precipitate			Conc(Cl) 1E-04 M					
Species/[Dy] in M	1E-10	1E-09	1E-08	1E-07	1E-06	1E-05	1E-04	1E-03	1E-02	1E-01	1E-00
free Dy^{3+}	0	0	0	0	0	0	0	0	0	0	0
$Dy(OH)^{2+}$	0	0	0	0	0	0	0	0	0	0	0
$Dy(OH)_2^+$	0	0	0	0	0	0	0	0	0	0	0
$Dy(OH)_3$ (aq)	0.61	0.61	0.61	0.61	0.25	0	0	0	0	0	0
$Dy(OH)_3$ (s)	0	0	0	0	58.56	95.86	99.59	99.96	100	100	100
$Dy(OH)_4^-$	99.39	99.39	99.39	99.39	41.18	4.12	0.41	0	0	0	0

Table B.7: chemical speciation [%] of dysprosium under pH = 12 and varying concentrations [M].

Dysprosium	Parameters:		Conc(H) 1E-12 M; Allow solids to precipitate			Conc(Cl) 1E-04 M					
Species/[Dy] in M	1E-10	1E-09	1E-08	1E-07	1E-06	1E-05	1E-04	1E-03	1E-02	1E-01	1E-00
free Dy^{3+}	0	0	0	0	0	0	0	0	0	0	0
$Dy(OH)^{2+}$	0	0	0	0	0	0	0	0	0	0	0
$Dy(OH)_2^+$	0	0	0	0	0	0	0	0	0	0	0
$Dy(OH)_3$ (aq)	0	0	0	0	0	0	0	0	0	0	0
$Dy(OH)_3$ (s)	0	0	0	0	0	56.6	95.66	99.57	99.96	100	100
$Dy(OH)_4^-$	99.94	99.94	99.94	99.94	99.94	43.48	4.34	0.43	0	0	0

B.1.1. Dysprosium speciation in experimental loading conditions

Table B.8: chemical speciation [%] of dysprosium with a concentration of 0.2 mM under varying pH.

Dysprosium	Parameters:		Conc(Dy) 2E-04 M; Allow solids to precipitate			Conc(Cl) 1E-04 M					
Species	pH 2	pH 3	pH 4	pH 5	pH 6	pH 7	pH 8	pH 9	pH 10	pH 11	pH 12
free Dy^{3+}	99.96	99.95	99.93	99.73	97.84	6.90	0	0	0	0	0
$Dy(OH)^{2+}$	0	0	0	0.21	2.11	1.66	0	0	0	0	0
$Dy(OH)_2^+$	0	0	0	0	0	0	0	0	0	0	0
$Dy(OH)_3$ (aq)	0	0	0	0	0	0	0	0	0	0	0
$Dy(OH)_3$ (s)	0	0	0	0	0	91.39	99.97	100	99.98	99.79	99.38
$Dy(OH)_4^-$	0	0	0	0	0	0	0	0	0	0.21	2.17

Table B.9: chemical speciation [%] of dysprosium with a concentration of 0.7 mM under varying pH.

Dysprosium	Parameters:		Conc(Dy) 7E-04 M; Allow solids to precipitate			Conc(Cl) 1E-04 M					
Species	pH 2	pH 3	pH 4	pH 5	pH 6	pH 7	pH 8	pH 9	pH 10	pH 11	pH 12
free Dy^{3+}	99.96	99.96	99.94	99.77	98.1	1.97	0	0	0	0	0
$Dy(OH)^{2+}$	0	0	0	0.19	1.85	0.47	0	0	0	0	0
$Dy(OH)_2^+$	0	0	0	0	0	0	0	0	0	0	0
$Dy(OH)_3$ (aq)	0	0	0	0	0	0	0	0	0	0	0
$Dy(OH)_3$ (s)	0	0	0	0	0	97.54	99.99	100	99.99	99.94	99.38
$Dy(OH)_4^-$	0	0	0	0	0	0	0	0	0	0	0.64

Table B.10: chemical speciation [%] of dysprosium with a concentration of 2.0 mM under varying pH.

Dysprosium	Parameters:		Conc(Dy) 2E-03 M; Allow solids to precipitate			Conc(Cl) 1E-04 M					
Species	pH 2	pH 3	pH 4	pH 5	pH 6	pH 7	pH 8	pH 9	pH 10	pH 11	pH 12
free Dy^{3+}	99.97	99.96	99.95	99.81	98.42	0.69	0	0	0	0	0
$Dy(OH)^{2+}$	0	0	0	0.16	1.54	0.17	0	0	0	0	0
$Dy(OH)_2^+$	0	0	0	0	0	0	0	0	0	0	0
$Dy(OH)_3$ (aq)	0	0	0	0	0	0	0	0	0	0	0
$Dy(OH)_3$ (s)	0	0	0	0	0	99.14	100	100	100	99.98	99.78
$Dy(OH)_4^-$	0	0	0	0	0	0	0	0	0	0	0.22

B.2. Holmium speciation

Table B.11: chemical speciation [%] of holmium under pH = 6 and varying concentrations [M].

Holmium	Parameters:		Conc(H) 1E-06 M; Allow solids to precipitate			Conc(Cl) 1E-04 M					
Species/[Ho] in M	1E-15	1E-14	1E-13	1E-12	1E-11	1E-10	1E-09	1E-08	1E-07	1E-06	1E-05
free Ho^{3+}	97.64	97.64	97.64	97.64	97.64	97.64	97.64	97.64	97.64	97.64	97.64
$Ho(OH)^{2+}$	2.32	2.32	2.32	2.32	2.32	2.32	2.32	2.32	2.32	2.32	2.32
$Ho(OH)_2^+$											
$Ho(OH)_3$ (aq)											
$Ho(OH)_3$ (s)											
$Ho(OH)_4^-$											

Table B.12: chemical speciation [%] of holmium under pH = 7 and varying concentrations [M].

Holmium	Parameters:		Conc(H) 1E-07 M; Allow solids to precipitate			Conc(Cl) 1E-04 M					
Species/[Ho] in M	1E-15	1E-14	1E-13	1E-12	1E-11	1E-10	1E-09	1E-08	1E-07	1E-06	1E-05
free Ho^{3+}	76.3	76.3	76.3	76.3	76.3	76.3	76.3	76.3	76.3	76.3	27.74
$Ho(OH)^{2+}$	23.09	23.09	23.09	23.09	23.09	23.09	23.09	23.09	23.09	23.09	8.36
$Ho(OH)_2^+$	0.56	0.56	0.56	0.56	0.56	0.56	0.56	0.56	0.56	0.56	0.2
$Ho(OH)_3$ (aq)											
$Ho(OH)_3$ (s)											63.68
$Ho(OH)_4^-$											

Table B.13: chemical speciation [%] of holmium under pH = 8 and varying concentrations [M].

Holmium	Parameters:		Conc(H) 1E-08 M; Allow solids to precipitate			Conc(Cl) 1E-04 M					
Species/[Ho] in M	1E-15	1E-14	1E-13	1E-12	1E-11	1E-10	1E-09	1E-08	1E-07	1E-06	1E-05
free Ho^{3+}	19.52	19.52	19.52	19.52	19.52	19.52	19.52	19.52	2.65	0.26	
$Ho(OH)^{2+}$	60.36	60.36	60.36	60.36	60.36	60.36	60.36	60.36	8.19	0.82	
$Ho(OH)_2^+$	14.72	14.72	14.72	14.72	14.72	14.72	14.72	14.72	2	0.2	
$Ho(OH)_3$ (aq)	4.65	4.65	4.65	4.65	4.65	4.65	4.65	4.65	0.63		
$Ho(OH)_3$ (s)									86.42	98.64	99.86
$Ho(OH)_4^-$	0.75	0.75	0.75	0.75	0.75	0.75	0.75	0.75	0.1		

B.2.1. Holmium speciation under optimal dysprosium loading conditions

Table B.14: chemical speciation [%] of holmium under pH = 7.5 and varying concentrations [M].

Holmium	Parameters:		Conc(H) 3.16E-08 M; Conc(Cl) 1E-04 M;				Conc(Dy) 7E-04 M Allow solids to precipitate				
Species/[Ho] in M	1E-15	1E-14	1E-13	1E-12	1E-11	1E-10	1E-09	1E-08	1E-07	1E-06	1E-05
free Ho^{3+}	48.53	48.53	48.53	48.53	48.53	48.53	48.53	48.53	48.53	8.4	0.84
$Ho(OH)^{2+}$	47.4	47.4	47.4	47.4	47.4	47.4	47.4	47.4	47.4	8.2	0.82
$Ho(OH)_2^+$	3.65	3.65	3.65	3.65	3.65	3.65	3.65	3.65	3.65	0.63	
$Ho(OH)_3$ (aq)	0.36	0.36	0.36	0.36	0.36	0.36	0.36	0.36	0.36		
$Ho(OH)_3$ (s)										82.69	98.27
$Ho(OH)_4^-$											

B.3. Dysprosium speciation with phosphate (PO4)3-

As we can see, phosphate creates solid with Dy even under pH 6. For higher pH, there is a competition between the phosphate and hydroxides to form a solid with dysprosium. This occurs when the concentration phosphates/hydroxides is similar. But, what does adding phosphates do to the pH of the solution?

B.3.1. Dysprosium and phosphate under pH 6

Table B.15: chemical speciation [%] of dysprosium ([Dy] = 2E-04 M) under pH = 6 and varying concentrations of phosphate [M].

Dy + [PO_4]$^{3-}$	Parameters:		Conc(H) 1E-06 M; Allow solids to precipitate			Conc(Dy) 2E-04 M				
Species/[PO_4]$^{3-}$ in M	1E-10	1E-09	1E-08	1E-07	1E-06	1E-05	1E-04	1E-03	1E-02	1E-01
free Dy^{3+}	97.88	97.88	97.87	97.83	97.39	92.97	48.89			
$Dy(OH)^{2+}$	2.12	2.12	2.12	2.12	2.11	2.02	1.11			
$Dy(OH)_2^+$										
$Dy(OH)_3$ (aq)										
$Dy(OH)_3$ (s)										
$DyPO_4$ (s)					0.5	5	50	100	100	100

Table B.16: chemical speciation [%] of dysprosium ([Dy] = 7E-04 M) under pH = pip and varying concentrations of phosphate [M].

Dy + [PO_4]$^{3-}$	Parameters:		Conc(H) 1E-06 M; Allow solids to precipitate			Conc(Dy) 7E-04 M				
Species/[PO_4]$^{3-}$ in M	1E-10	1E-09	1E-08	1E-07	1E-06	1E-05	1E-04	1E-03	1E-02	1E-01
free Dy^{3+}	98.14	98.14	98.14	98.13	98	96.74	84.09			
$Dy(OH)^{2+}$	1.85	1.85	1.85	1.85	1.85	1.83	1.62			
$Dy(OH)_2^+$										
$Dy(OH)_3$ (aq)										
$Dy(OH)_3$ (s)										
$DyPO_4$ (s)					0.14	1.43	14.29	100	100	100

Table B.17: chemical speciation [%] of dysprosium ([Dy] = 2E-03 M) under pH = 6 and varying concentrations of phosphate [M].

Dy + [PO_4]$^{3-}$	Parameters:	Conc(H) 1E-06 M; Allow solids to precipitate				Conc(Dy) 2E-03 M				
Species/[PO_4]$^{3-}$ in M	1E-10	1E-09	1E-08	1E-07	1E-06	1E-05	1E-04	1E-03	1E-02	1E-01
free Dy^{3+}	98.45	98.45	98.45	98.45	98.4	97.96	93.51	49.12		
$Dy(OH)^{2+}$	1.55	1.55	1.55	1.55	1.54	1.54	1.48	0.88		
$Dy(OH)_2^+$										
$Dy(OH)_3$ (aq)										
$Dy(OH)_3$ (s)										
$DyPO_4$ (s)						0.5	5	50	100	100

B.3.2. Dysprosium and phosphate under pH 7

Table B.18: chemical speciation [%] of dysprosium ([Dy] = 2E-04 M) under pH = 7 and varying concentrations of phosphate [M].

Dy + [PO_4]$^{3-}$	Parameters:	Conc(H) 1E-07 M; Allow solids to precipitate				Conc(Dy) 2E-04 M				
Species/[PO_4]$^{3-}$ in M	1E-10	1E-09	1E-08	1E-07	1E-06	1E-05	1E-04	1E-03	1E-02	1E-01
free Dy^{3+}	6.71	6.71	6.71	6.71	6.71	6.71	6.71			
$Dy(OH)^{2+}$	1.64	1.64	1.64	1.64	1.64	1.64	1.64			
$Dy(OH)_2^+$										
$Dy(OH)_3$ (aq)										
$Dy(OH)_3$ (s)	91.6	91.6	91.6	91.55	91.1	86.8	41.6			
$DyPO_4$ (s)					0.5	5	50	100	100	100

Table B.19: chemical speciation [%] of dysprosium ([Dy] = 7E-04 M) under pH = 7 and varying concentrations of phosphate [M].

Dy + [PO_4]$^{3-}$	Parameters:	Conc(H) 1E-07 M; Allow solids to precipitate				Conc(Dy) 7E-04 M				
Species/[PO_4]$^{3-}$ in M	1E-10	1E-09	1E-08	1E-07	1E-06	1E-05	1E-04	1E-03	1E-02	1E-01
free Dy^{3+}	1.92	1.92	1.92	1.92	1.92	1.92	1.92			
$Dy(OH)^{2+}$	0.47	0.47	0.47	0.47	0.47	0.47	0.47			
$Dy(OH)_2^+$										
$Dy(OH)_3$ (aq)										
$Dy(OH)_3$ (s)	97.6	97.6	97.6	97.59	97.46	96.17	83.32			
$DyPO_4$ (s)					0.14	1.43	14.29	100	100	100

Table B.20: chemical speciation [%] of dysprosium ([Dy] = 2E-03 M) under pH = 7 and varying concentrations of phosphate [M].

Dy + [PO_4]$^{3-}$	Parameters:	Conc(H) 1E-07 M; Allow solids to precipitate				Conc(Dy) 2E-03 M				
Species/[PO_4]$^{3-}$ in M	1E-10	1E-09	1E-08	1E-07	1E-06	1E-05	1E-04	1E-03	1E-02	1E-01
free Dy^{3+}	0.67	0.67	0.67	0.67	0.67	0.67	0.67			
$Dy(OH)^{2+}$	0.16	0.16	0.16	0.16	0.16	0.16	0.16			
$Dy(OH)_2^+$										
$Dy(OH)_3$ (aq)										
$Dy(OH)_3$ (s)	99.16	99.16	99.16	99.16	99.11	98.66	94.16	49.16		
$DyPO_4$ (s)						0.5	5	50	100	100

B.3.3. Dysprosium and phosphate under pH 8

Table B.21: chemical speciation [%] of dysprosium ([Dy] = 2E-04 M) under pH = 8 and varying concentrations of phosphate [M].

Dy + [PO_4]$^{3-}$	Parameters:	Conc(H) 1E-08 M; Allow solids to precipitate				Conc(Dy) 2E-04 M				
Species/[PO_4]$^{3-}$ in M	1E-10	1E-09	1E-08	1E-07	1E-06	1E-05	1E-04	1E-03	1E-02	1E-01
free Dy^{3+}										
$Dy(OH)^{2+}$										
$Dy(OH)_2^+$										
$Dy(OH)_3$ (aq)										
$Dy(OH)_3$ (s)	99.97	99.97	99.97	99.92	99.47	94.97	49.97			
$DyPO_4$ (s)					0.5	5	50	100	100	100

Table B.22: chemical speciation [%] of dysprosium ([Dy] = 7E-04 M) under pH = 8 and varying concentrations of phosphate [M].

Dy + [PO_4]$^{3-}$	Parameters:	Conc(H) 1E-08 M; Allow solids to precipitate				Conc(Dy) 7E-04 M				
Species/[PO_4]$^{3-}$ in M	1E-10	1E-09	1E-08	1E-07	1E-06	1E-05	1E-04	1E-03	1E-02	1E-01
free Dy^{3+}										
$Dy(OH)^{2+}$										
$Dy(OH)_2^+$										
$Dy(OH)_3$ (aq)										
$Dy(OH)_3$ (s)	99.99	99.99	99.99	99.99	99.85	98.56	85.71			
$DyPO_4$ (s)					0.14	1.43	14.29	100	100	100

Table B.23: chemical speciation [%] of dysprosium ([Dy] = 2E-03 M) under pH = 8 and varying concentrations of phosphate [M].

Dy + [PO_4]$^{3-}$	Parameters:	Conc(H) 1E-08 M; Allow solids to precipitate				Conc(Dy) 2E-03 M				
Species/[PO_4]$^{3-}$ in M	1E-10	1E-09	1E-08	1E-07	1E-06	1E-05	1E-04	1E-03	1E-02	1E-01
free Dy^{3+}										
$Dy(OH)^{2+}$										
$Dy(OH)_2^+$										
$Dy(OH)_3$ (aq)										
$Dy(OH)_3$ (s)	100	100	100	99.99	99.95	99.5	95	50		
$DyPO_4$ (s)						0.5	5	50	100	100

B.4. Gallium speciation

The gallium chemical speciation is determined for 25 degrees Celsius in CHEAQs.

Table B.24: chemical speciation [%] of gallium under pH = 5 and varying concentrations [M].

Gallium	Parameters:		Conc(H) 1E-05 M; Allow solids to precipitate			Conc(Cl) 1E-04 M	
Species/[Ga] in M	1E-15 to 1E-09	1E-08	1E-07	1E-06	1E-05	1E-04	1E-03 to 1E-01
free Ga^{3+}	0	0	0	0	0	0	0
Ga(OH) $^{2+}$	0.23	0.20	0	0	0	0	0
$Ga(OH)_2^+$	3.65	3.17	0.32	0	0	0	0
$Ga(OH)_3$ (aq)	91.46	79.49	7.95	0.79	0	0	0
$Ga(OH)_4^-$	4.66	4.05	0.40	0	0	0	0
Ga_2O_3	0	13.15	91.32	99.13	99.91	99.99	100

Table B.25: chemical speciation [%] of gallium under pH = 5.5 and varying concentrations [M].

Gallium	Parameters:		Conc(H) 3.16E-06 M; Allow solids to precipitate			Conc(Cl) 1E-04 M	
Species/[Ga] in M	1E-15 to 1E-09	1E-08	1E-07	1E-06	1E-05	1E-04	1E-03 to 1E-01
free Ga^{3+}	0	0	0	0	0	0	0
Ga(OH) $^{2+}$	0	0	0	0	0	0	0
$Ga(OH)_2^+$	1.07	1.00	0.10	0	0	0	0
$Ga(OH)_3$ (aq)	85.19	79.53	7.94	0.79	0	0	0
$Ga(OH)_4^-$	13.72	12.81	1.28	0.13	0	0	0
Ga_2O_3	0	6.75	90.68	99.07	99.91	99.99	100

Table B.26: chemical speciation [%] of gallium under pH = 6 and varying concentrations [M].

Gallium	Parameters:		Conc(H) 1E-06 M; Allow solids to precipitate			Conc(Cl) 1E-04 M	
Species/[Ga] in M	1E-15 to 1E-09	1E-08	1E-07	1E-06	1E-05	1E-04	1E-03 to 1E-01
free Ga^{3+}	0	0	0	0	0	0	0
Ga(OH) $^{2+}$	0	0	0	0	0	0	0
$Ga(OH)_2^+$	0.26	0.26	0	0	0	0	0
$Ga(OH)_3$ (aq)	66.10	66.10	7.94	0.79	0	0	0
$Ga(OH)_4^-$	33.63	33.63	4.04	0.40	0	0	0
Ga_2O_3	0	0	87.94	98.80	99.88	99.99	100

Table B.27: chemical speciation [%] of gallium under pH = 6.5 and varying concentrations [M].

Gallium	Parameters:		Conc(H) 3.16E-07 M; Allow solids to precipitate			Conc(Cl) 1E-04 M	
Species/[Ga] in M	1E-15 to 1E-09	1E-08	1E-07	1E-06	1E-05	1E-04	1E-03 to 1E-01
free Ga^{3+}	0	0	0	0	0	0	0
$Ga(OH)^{2+}$	0	0	0	0	0	0	0
$Ga(OH)_2^+$	0	0	0	0	0	0	0
$Ga(OH)_3$ (aq)	38.29	38.29	7.94	0.79	0	0	0
$Ga(OH)_4^-$	61.66	61.66	12.79	1.28	0.13	0	0
Ga_2O_3	0	0	79.26	97.93	99.79	99.98	100

Table B.28: chemical speciation [%] of gallium under pH = 7 and varying concentrations [M].

Gallium	Parameters:		Conc(H) 1E-07 M; Allow solids to precipitate			Conc(Cl) 1E-04 M	
Species/[Ga] in M	1E-15 to 1E-09	1E-08	1E-07	1E-06	1E-05	1E-04	1E-03 to 1E-01
free Ga^{3+}	0	0	0	0	0	0	0
$Ga(OH)^{2+}$	0	0	0	0	0	0	0
$Ga(OH)_2^+$	0	0	0	0	0	0	0
$Ga(OH)_3$ (aq)	16.42	16.42	7.94	0.79	0	0	0
$Ga(OH)_4^-$	83.57	83.57	40.42	4.04	0.40	0	0
Ga_2O_3	0	0	51.64	95.16	99.52	99.95	100

Table B.29: chemical speciation [%] of gallium under pH = 7.5 and varying concentrations [M].

Gallium	Parameters:		Conc(H) 3.16E-08 M; Allow solids to precipitate			Conc(Cl) 1E-04 M	
Species/[Ga] in M	1E-15 to 1E-09	1E-08	1E-07	1E-06	1E-05	1E-04	1E-03 to 1E-01
free Ga^{3+}	0	0	0	0	0	0	0
$Ga(OH)^{2+}$	0	0	0	0	0	0	0
$Ga(OH)_2^+$	0	0	0	0	0	0	0
$Ga(OH)_3$ (aq)	5.85	5.85	5.85	0.79	0	0	0
$Ga(OH)_4^-$	94.15	94.15	94.15	12.79	1.28	0.13	0
Ga_2O_3	0	0	0	86.42	98.64	99.86	100

Table B.30: chemical speciation [%] of gallium under pH = 8 and varying concentrations [M].

Gallium	Parameters:		Conc(H) 1E-08 M; Allow solids to precipitate			Conc(Cl) 1E-04 M	
Species/[Ga] in M	1E-15 to 1E-09	1E-08	1E-07	1E-06	1E-05	1E-04	1E-03 to 1E-01
free Ga^{3+}	0	0	0	0	0	0	0
$Ga(OH)^{2+}$	0	0	0	0	0	0	0
$Ga(OH)_2^+$	0	0	0	0	0	0	0
$Ga(OH)_3$ (aq)	0.20	0.20	1.93	0.79	0	0	0
$Ga(OH)_4^-$	99.80	98.07	98.07	40.42	4.04	0.13	0
Ga_2O_3	0	0	0	58.79	95.88	95.59	100

Table B.31: chemical speciation [%] of gallium under pH = 9 and varying concentrations [M].

Gallium	Parameters:		Conc(H) 1E-09 M; Allow solids to precipitate			Conc(Cl) 1E-04 M	
Species/[Ga] in M	1E-15 to 1E-09	1E-08	1E-07	1E-06	1E-05	1E-04	1E-03 to 1E-01
free Ga^{3+}	0	0	0	0	0	0	0
$Ga(OH)^{2+}$	0	0	0	0	0	0	0
$Ga(OH)_2^+$	0	0	0	0	0	0	0
$Ga(OH)_3$ (aq)	1.93	1.93	1.93	0.79	0	0	0
$Ga(OH)_4^-$	98.07	98.07	98.07	40.42	4.04	0.13	0
Ga_2O_3	0	0	0	58.79	95.88	95.59	100

B.4.1. Gallium speciation in experimental loading conditions

Table B.32: chemical speciation [%] of [Ga-68] with a concentration of 3.8E-13M mM under varying pH.

Gallium	Parameters:		Conc(Ga) 3.8E-13 M; Allow solids to precipitate			Conc(Cl) 1E-04 M					
Species	pH 2	pH 3	pH 4	pH 5	pH 6	pH 7	pH 8	pH 9	pH 10	pH 11	pH 12
free Ga^{3+}	92.00	43.26	1.29	0	0	0	0	0	0	0	0
$Ga(OH)^{2+}$	7.87	47.93	15.39	0.23	0	0	0	0	0	0	0
$Ga(OH)_2^+$	0.10	7.06	23.72	3.65	0.26	0	0	0	0	0	
$Ga(OH)_3$ (aq)	0	1.74	59.30	91.46	66.10	16.42	1.93	0.20	0	0	0
$Ga(OH)_4^-$	0	0	0.30	4.66	33.63	83.57	98.07	99.80	99.97	100	100
Ga_2O_3	0	0	0	0	0	0	0	0	0	0	0

Table B.33: chemical speciation [%] of [Ga] = 0.2136 mM under varying pH.

Gallium	Parameters:	Conc(Ga) 0.2136 mM; Conc(Cl) 1E-04 M Allow solids to precipitate									
Species	pH 2	pH 3	pH 4	pH 5	pH 6	pH 7	pH 8	pH 9	pH 10	pH 11	pH 12
free Ga^{3+}	86.71	0	0	0	0	0	0	0	0	0	0
$Ga(OH)^{2+}$	7.21	0.10	0	0	0	0	0	0	0	0	0
$Ga(OH)_2^+$	0	0	0	0	0	0	0	0	0	0	
$Ga(OH)_3$ (aq)	0	0	0	0	0	0	0	0	0	0	0
$Ga(OH)_4^-$	0	0	0	0	0	0	0.19	1.89	19.01	100	99.99
Ga_2O_3	0	99.79	99.99	100	99.99	99.98	99.81	98.10	80.99	0	0
$Ga_2(OH)_2^{4+}$	5.97	0	0	0	0	0	0	0	0	0	0